STRANGE PARTICLE PRODUCTION IN SULPHUR-SULPHUR INTERACTIONS AT 200 GeV/c PER NUCLEON

Andrew Charles Bayes

Thesis submitted for the degree of
Doctor of Philosophy

School of Physics and Space Research
Faculty of Science
The University of Birmingham

March 1995

Synopsis

The aim of the WA94 experiment is to study the production of strange and multistrange particles and antiparticles, in the central rapidity and medium p_T region, in ultra relativistic heavy ion collisions. Strange particle production is expected to be a useful probe of the dynamics of hadronic matter at extreme conditions of temperature and energy density.

In this thesis, the 100 million triggers obtained by WA94 in 1991 using sulphur-sulphur interactions at 200 GeV/c per nucleon are analysed. The techniques used to reconstruct the strange particles are discussed, giving raw particle yields of 56140 Λs, 18014 $\overline{\Lambda}$s, 547 Ξ^-s, 278 $\overline{\Xi^-}$s, 430 K^+s and 202 K^-s. The data are corrected for reconstruction efficiency and acceptance and the Λ ($\overline{\Lambda}$) sample is corrected for feed-down from Ξ ($\overline{\Xi}$) decays, an effect of about 20% for Λs and 35% for $\overline{\Lambda}$s.

The corrected particle ratios in the central rapidity region are found to be;

$$\Xi^-/\Lambda = 0.08 \pm 0.01,$$

$$\overline{\Xi^-}/\overline{\Lambda} = 0.20 \pm 0.02,$$

$$K^-/\Lambda = 1.3 \pm 0.2,$$

$$K^+/\Lambda = 2.5 \pm 0.3.$$

These ratios are consistent with other heavy ion data, and in particular the $\overline{\Xi^-}/\overline{\Lambda}$ value of 0.20 ± 0.02 is significantly higher than that obtained in non-heavy ion data. The transverse mass distributions are also plotted giving inverse slopes corresponding to temperatures of the order of 200 MeV for a thermal source.

To

Mum and Dad.

Acknowledgements

I should like to thank Professors George Morrison and John Dowell for giving me the opportunity to undertake a Ph.D. in the School of Physics and Space Research. I acknowledge the financial support from the Science and Engineering Research Council for the funding I have received during my studentship.

I would like to thank my tutor Dr. Frank Votruba for his help during my Ph.D. and especially for reading the various drafts of my thesis. Thanks must also be extended to Professor John Kinson and Drs Orlando Villalobos Baille, Dave Evans and Roman Lietava for their help and encouragement throughout my Ph.D. For help with computing problems thanks are also due to Dr. Laurie Lowe for solving many a problem on both the IBM and more recently the HP.

On the social side of things I must thank those people who I have been lucky enough to get to know throughout my years of *education*. Roughly in the order that I met them they are: Paul Davies, for some 10 years a good friend; my house mates and good friends Ashley Hall, Mike Foss, Martin Jones, Steve Clewer and Oliver Ragg, for putting up with me and making life so enjoyable whilst at University; and of course last but not least are my fellow Ph.D.ers/R.A.s which include some of the above and all of the following for making Ph.D. life much more enjoyable than it could have been, these are (again in the rough order that I met them) Jim Clayton, Stuart Robertson, Richard Barnes, Chris Dodenhoff, Mike Haben, Mark Whalley, Dave Rees, Steve Hillier, Tan Ahmed, Rob (my liver hurts) Akers, Paul Newman (not the actor), Mark Pearce, Dave (muscleman) Rigby, Neil Talbot, Vicki Hudgson, Keith (or is it Brucey) Norman, Tim Nicholls, Lee West, Paul Sutton and the present batch of first years Mark Venables, Kirsty Hewitt, James Bloomer,

Andrew Bell and Steve Oglesby.

During the last year of my Ph.D. it seems that I have spent about half of the time up in Manchester, the reason for this is Sharon and my thanks and love go to her for the love and support she has given me over this time[1].

Lastly, but certainly not least, I am deeply grateful to my family and especially my parents for all their love and encouragement they have shown me, and it is to them that I dedicate this thesis.

Andy Bayes, 21st March 1995, Birmingham.

[1] long may it continue

Contents

1 The Quark Gluon Plasma **1**

1.1 Introduction 1

1.2 Quantum Chromodynamics 2

1.3 The Quark Gluon Plasma 5

1.4 Heavy Ion Interactions at Relativistic Energies 6

1.5 Evolution of the plasma 7

1.6 QGP Signals 7

1.6.1 Direct photons 7

1.6.2 Dileptons 9

1.6.3 J/Ψ and Ψ' Suppression 10

1.7 Strangeness Enhancement 11

1.8 WA85 Experiment 14

1.9 Summary 19

2 The Apparatus **21**

2.1 Introduction 21

2.2 The Butterfly Principle 22

2.3 WA94 Experimental Setup 25

2.4 The Omega Spectrometer 25

2.5 Silicon Microstrips 27

2.6 The Multiwire Proportional Chambers 27

2.7 The Trigger 30

2.8 Data Acquisition 32

3 Reconstruction of Λ and Ξ decays **34**

3.1 Reconstructing V^0s 34

3.2 Identifying Λ hyperons 36

3.3 Impact parameter cuts 40

3.4 Summary of cuts used to identify Λs and $\overline{\Lambda}$s 42

3.5 K^0 Contamination 44

3.6 Results on Λ and $\overline{\Lambda}$ production 44

3.7 Identifying Ξs and $\overline{\Xi}$s 46

3.8 Further cuts performed on the Ξ candidates 48

3.8.1 Impact Parameter cuts 50

3.9 Summary of cuts used to identify Ξs and $\overline{\Xi}$s 51

3.10 Summary 54

4 Identifying K^- and K^+ meson decays **56**

4.1 Further cuts performed on the $K^{\pm}$ candidates. 57

4.2 Summary of cuts used to identify K^- and K^+ meson decays 62

5 Calculation of Acceptances **66**

5.1 Λ Acceptance 67

5.2 Ξ Acceptance 68

5.3 K Acceptance 70

6 Reconstruction Efficiencies **74**

6.1 Calculation of the Chamber Efficiencies 76

6.1.1 Chamber Edge Effects 77

6.1.2 Chamber Efficiency Results 77

6.2 Structure of raw data events 77

6.3 Implantation of the Monte Carlo data 80

6.4 Λ Reconstruction Efficiencies 81

6.5 Ξ Reconstruction Efficiencies 84

6.6 K Reconstruction Efficiencies 87

6.7 Further corrections to the data 91
6.8 Summary 92

7 Corrected particle ratios and M_T distributions 93
7.1 Corrected particle yields 93
7.2 M_T distributions 97
7.3 Summary 101

8 Summary and outlook 102
8.1 Results 102
8.2 Future Plans 103
8.3 Conclusions 105

A The Butterfly Geometry 107

B Armenteros Plots 109

C Acceptance Tables 112

D MWPC efficiencies for the 1991 ions run 116

List of Figures

1.1 Screening of a) electric charge and b) colour charge in quantum field theory. 3

1.2 Phase diagram of the QGP. 5

1.3 Before and after the collision of 2 relativistic sulphur nuclei. 6

1.4 An idealized space time diagram of the evolution of the QGP after a relativistic heavy ion collision. 8

1.5 γ/π^0 ratio as a function of p_T for central and peripheral S+Au data at 200 A GeV. The dots represent the inclusive photon data, the histograms all photons from hadronic background sources. 9

1.6 J/Ψ suppression as observed by NA38, where R is defined as the J/Ψ to continuum ratio. 10

1.7 Ψ' suppression relative to J/Ψ as ϵ increases (the box shows the average value for p-A interactions). 11

1.8 Time development of the strangeness content of the Quark Gluon Plasma at different temperatures. The saturation time at 200 MeV is about 10^{-23}s. Dashed lines indicate no $s\overline{s}$ annihilations. 13

1.9 $\frac{1}{m_T^{\frac{3}{2}}}\frac{dN}{dm_T}$ vs m_T for a) Λs and Ξ^-s, and b) $\overline{\Lambda}$s and $\overline{\Xi^-}$s, obtained by WA85. 16

1.10 Ξ^-/Λ and $\overline{\Xi^-}/\overline{\Lambda}$ ratios for different experiments. 18

1.11 Effective mass distributions of $\Omega^- + \overline{\Omega^-}$candidates in SW interactions. . . 18

2.1 A central sulphur-sulphur event as observed in a streamer chamber (NA35 collaboration). 23

2.2 A typical Ξ^- event as seen in the OMEGA wire chambers. 23

2.3 An illustration of how the butterfly principle works. 24

2.4 The WA94 experimental layout used in the 1991 run. 26
2.5 Exploded view of a section through one of the Omega A MWPCs. 29
2.6 Schematic diagram of the trigger elements for the 1991 run. 31
2.7 Timing of input signals to the clean beam coincidence unit, the signals in dashed lines are caused by a second incident beam particle. 32
2.8 The Romulus structure for WA94, 1991 run. 33

3.1 Effective mass ($p\pi^-$) of a sample of V^0 candidates after passing through STRIPV0. 36
3.2 Schematic representation of a possible Λ decay. 37
3.3 Distribution of the V^0's vertex. 37
3.4 Distribution of a) the closest approach between positive and negative tracks and b) the angle, ϑ, between the sum of the three momenta of the V^0 decay tracks and the line of flight from the centre of the target, for Λ candidates that have had all other cuts applied. 38
3.5 Podolanski-Armenteros plot for V^0 candidates. 39
3.6 Crossing paths of two V^0 decay tracks. 41
3.7 Distribution of the impact parameters. 43
3.8 Effective mass plots of Λ candidates after a) having passed through STRIPV0 and then having the cuts b) i and ii, c) i to iv and d) i to vii performed on them. 45
3.9 Effective mass distributions for V^0 candidates as (a) $p\pi^-$ and (b) $\overline{p}\pi^+$. . . 46
3.10 Schematic representation of a possible Ξ^- decay. 47
3.11 M($\Lambda\pi^-$). 48
3.12 Distribution of the vertices of Ξ candidates. 49
3.13 Distribution of closxi. 50
3.14 Effective mass distribution of a) M($\Lambda\pi^-$) and b) M($\overline{\Lambda}\pi^+$). 51
3.15 Distribution of the impact parameter of the pion, *bypi*, and *bypi* plotted against M($\Lambda\pi^-$). 52
3.16 Distribution of the impact parameter of the cascade, *byxi*, and *byxi* plotted against M($\Lambda\pi^-$). 52

3.17 Effective mass distribution of a) M($\Lambda\pi^-$) and b) M($\overline{\Lambda}\pi^+$). 54

4.1 Momentum distribution of V^0s coming from Monte Carlo K decays. . . . 57
4.2 Effective mass distribution, M($\pi\pi\pi$), after initial cuts are applied. 58
4.3 x_Ω coordinate of candidates vertices against M($\pi\pi\pi$). 58
4.4 Impact parameters of the reconstructed $K^\pm$s at the target. 59
4.5 Distribution of the impact parameters of the three decay tracks. 60
4.6 A schematic representation of a possible $K^\pm$ decay. 61
4.7 Distribution of the distance between the V^0 and the third pion. 61
4.8 Effective mass plots of $K^\pm$ candidates after a) having loose WA9XI cuts and cuts i and vi, b) i to v c) i to vii and d) i to viii performed on them. . 63
4.9 Momentum distribution of V^0s superimposed onto V^0s coming from Monte Carlo K decays. 64
4.10 Effective mass distributions of a) $M(\pi^+\pi^-\pi^-)$ and b) $M(\pi^+\pi^-\pi^+)$. . . . 65

5.1 Geometrical acceptance of unambiguous Λs as a function of rapidity and p_T. 69
5.2 Geometrical acceptance of Ξ^-s as a function of rapidity and p_T. 71
5.3 Geometrical acceptance of charged kaons as a function of rapidity and p_T. 73

6.1 Flow of processes used to calculate the reconstruction efficiencies of the different particles reconstructed by WA94 in the sulphur-sulphur interactions. 75
6.2 The four logical quadrants of the MWPCs. 76
6.3 The variation in chamber efficiency close to the edge of the butterfly region of chamber 1, plane Y (a), plane U (b) and plane V (c). The population of reconstructed tracks at the edge of the butterfly region are shown in (d). 78
6.4 Chamber efficiencies of the 7 A chambers used by WA94 in the 1991 S-S run. 79
6.5 Structure of a raw data event. 80
6.6 Structure of TRIDENT header block. 81
6.7 Vertex distribution of a) Monte Carlo Λs and b) Monte Carlo Λs after passing through the analysis chain, the dots represent real data. 83
6.8 Mass distribution of a) Real Λs and b) Monte Carlo Λs. 84

6.9 Reconstruction efficiencies as a function of MWPC cluster multiplicity for a) Λs field down (B=1.8T $\downarrow$), b) $\overline{\Lambda}$s (B=1.8T $\downarrow$), c) Λs (B=1.8T $\uparrow$) and d) $\overline{\Lambda}$s (B=1.8T $\uparrow$). 85

6.10 Vertex distribution of a) Monte Carlo Ξs and b) Monte Carlo Ξs after passing through the analysis chain, the dots represent real data. 86

6.11 Reconstruction efficiencies as a function of MWPC cluster multiplicity for a) Ξ^-s field down, b) $\overline{\Xi^-}$s (B=1.8T $\downarrow$), c) Ξ^-s (B=1.8T $\uparrow$) and d) $\overline{\Xi^-}$s (B=1.8T $\uparrow$). 88

6.12 Vertex distribution of a) Monte Carlo Ks and b) Monte Carlo Ks after passing through the analysis chain, the dots represent real data. 89

6.13 Reconstruction efficiencies as a function of MWPC cluster multiplicity for a) K^+s field down, b) K^-s (B=1.8T $\downarrow$), c) K^+s (B=1.8T $\uparrow$) and d) K^-s (B=1.8T $\uparrow$). 90

7.1 Ξ^-/Λ and $\overline{\Xi^-}/\overline{\Lambda}$ ratios for different experiments, including the WA94 points. 96

7.2 Transverse mass distributions for a) Λs and Ξ^-s, and b) $\overline{\Lambda}$s and $\overline{\Xi^-}$s, obtained by WA94. 99

7.3 Transverse mass distributions for charged kaons, obtained by WA94. . . . 100

8.1 The WA97 experimental layout used in the 1994 run and inset a Λ mass distribution. 104

B.1 Schematic representation of a V^0 decay in a) the lab frame and b) the centre of mass frame of the V^0 decay. 109

B.2 Podolanski-Armenteros regions for different V^0 candidates. 111

List of Tables

1.1 Quark Flavours. 2

1.2 V^0 and cascade yields from the WA85 1990 SW, 1987 SW, and 1988 pW runs. 15

1.3 Strange particle enhancement w.r.t. h^- multiplicity from pW to central SW interactions as observed by WA85. 15

1.4 Inverse slopes for hyperons in SW interactions (MeV) obtained by WA85. 15

1.5 Summary of the different particle ratios, and their respective acceptance intervals, obtained by WA85. 17

1.6 Main collaborations active in the heavy ion physics field 20

3.1 Raw yields obtained from the WA94 1991 sulphur sulphur data. 54

7.1 Raw yields of strange and multistrange particles and antiparticles obtained by WA94 in the 1991 sulphur-sulphur run. 94

7.2 Strangeness Production Ratios for WA94 (S S), WA85 (S W) and NA36 (S Pb). 95

7.3 Relative strange particle yields obtained by WA94 (S S) and WA85 (S W) in the given interval. 96

7.4 Charged kaon production ratios obtained by WA94. 97

7.5 Inverse slopes in MeV for Λs and Ξs. 98

7.6 Inverse slopes in MeV for charged kaons. 98

B.1 Armenteros quantities. 111

C.1 Acceptances for Λs produced in S S interactions (in percent). 113
C.2 Acceptances for Ξ^-s produced in S S interactions (in percent). 114
C.3 Acceptances for K^+s produced in S S interactions (in percent). 115

D.1 Mean efficiencies for chamber A1. 116
D.2 Mean efficiencies for chamber A2. 117
D.3 Mean efficiencies for chamber A3. 117
D.4 Mean efficiencies for chamber A4. 118
D.5 Mean efficiencies for chamber A5. 118
D.6 Mean efficiencies for chamber A6. 119
D.7 Mean efficiencies for chamber A7. 119

Chapter 1

The Quark Gluon Plasma

1.1 Introduction

In the early eighties the possibility of creating a new phase of matter, the Quark Gluon Plasma, in the collisions of ultra-relativistic heavy ions was foreseen. This led to a series of heavy ion experiments starting in 1986 at the Brookhaven AGS and the CERN SPS. One of these experiments was WA85; this thesis concerns the production of strange particles in sulphur-sulphur interactions at 200 GeV/c per nucleon by the WA94 collaboration, a successor of WA85.

The Quark Gluon Plasma has been predicted by QCD, so a brief overview of QCD is presented before the plasma phase and the relation between the existence of the QGP and the production of strange particles is discussed.

Table 1.1: Quark Flavours.

Quarks		Antiquarks	
$Q/\mid e \mid = +\frac{2}{3}$	u, c, t	$Q/\mid e \mid = -\frac{2}{3}$	$\overline{u}, \overline{c}, \overline{t}$
$Q/\mid e \mid = -\frac{1}{3}$	d, s, b	$Q/\mid e \mid = +\frac{1}{3}$	$\overline{d}, \overline{s}, \overline{b}$
u = 'up' quark		$m_u \sim m_d \sim 350 MeV/c^2$	
d = 'down' quark			
s = 'strange'		$m_s \sim 550$ MeV/c^2	
c = 'charmed'		$m_c \sim 1800$ MeV/c^2	
b = 'bottom'		$m_b \sim 4500$ MeV/c^2	
t = 'top'		$m_t \sim 174$ GeV/c^2	

1.2 Quantum Chromodynamics

Quantum Chromodynamics (QCD) describes the strong interaction between quarks by the exchange of massless gluons [1]. Quarks occur in several different varieties, as shown in table 1.1 [1]. As well as their flavour properties quarks are postulated to have an additional degree of freedom. This was needed to explain the discovery by Fermi in 1951 of the Δ^{++} baryon, in which the three up quarks exist with parallel spins, i.e. in a completely symmetric bound state which is forbidden by Fermi statistics. This further degree of freedom has become known as colour.

This strong force must overrule the electromagnetic repulsion of the three quarks in the Δ^{++} particle. In fact the strong force relates to the colour charge in close analogy with the familiar electrical charge in Quantum Electrodynamics (QED), the theory behind electroweak forces. A quark can carry one of three colours, labelled red, green and blue and an antiquark the corresponding anticolours.

Unlike QED, where the photons are electrically neutral, the gluons themselves also carry the colour charge. This effect leads to such things as the confinement of quarks and gluons, where although at short distances there will only be single gluon

[1] The observation of the top quark corresponds to a 2.8σ effect which is not sufficient to firmly establish the existence of top but which, if interpreted as top, yields the mass shown [2].

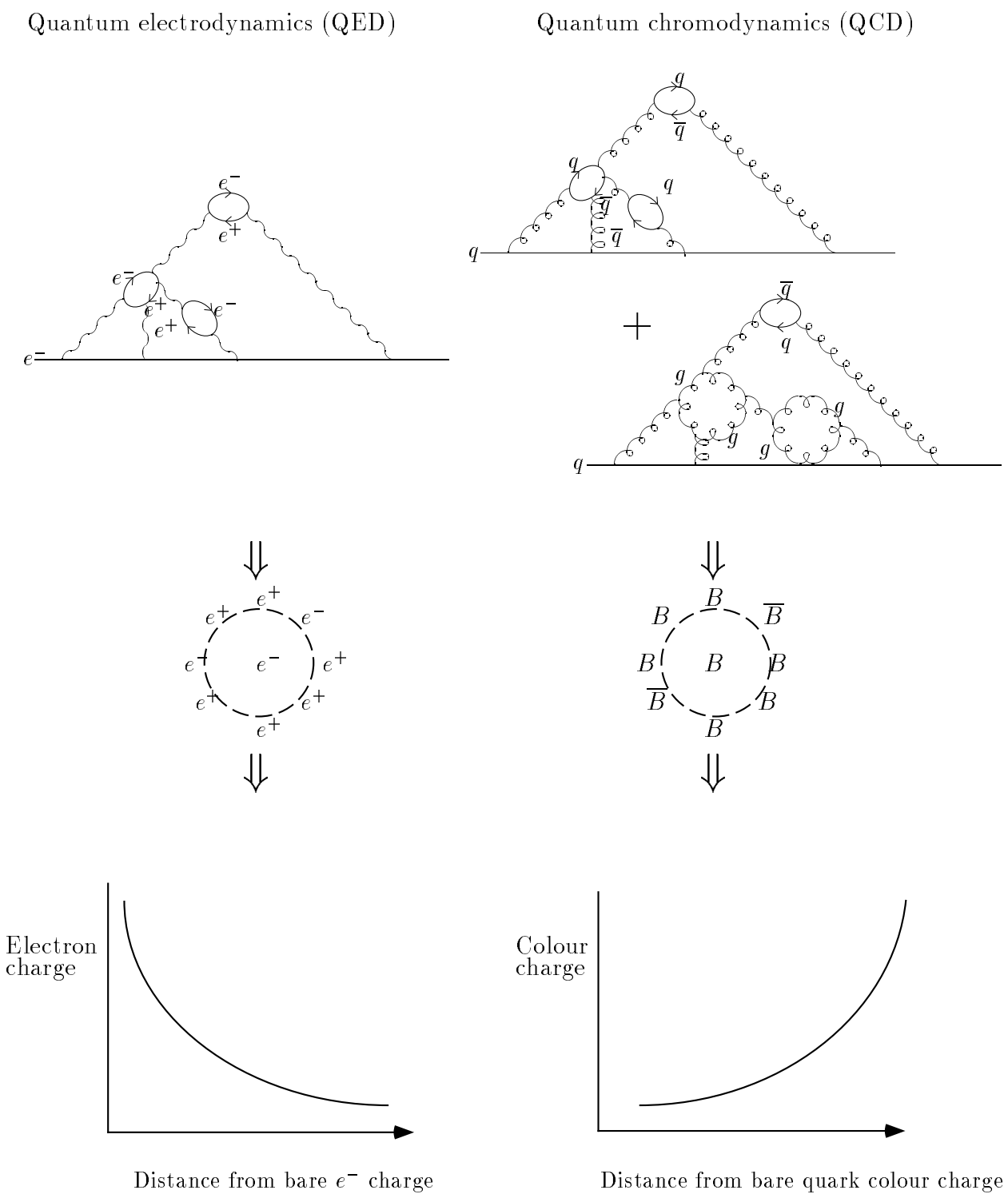

Figure 1.1: Screening of a) electric charge and b) colour charge in quantum field theory.

exchange between quarks and the potential will be of rather similar form to the electric potential (i.e. 1/r), at larger distances there will be multi gluon exchange and the colour field lines tend to group together to form a flux tube connecting the coloured charges [3]. This causes the energy of a field to grow linearly with the distance, r, between the quarks, and the potential is of the form

$$V_S(r) \sim -\frac{\alpha_S}{r} + \gamma r$$

where α_S is the strong coupling constant.

Another result of the self interaction of gluons is the Quantum Chromodynamical equivalent to charge screening in QED. In quantum field theory an electron can continually emit and absorb photons which may annihilate to produce e^+e^- pairs. Therefore the original electron will be surrounded by a number of e^+e^- pairs, as shown in figure 1.1a, and because opposite charges attract the positrons will be preferentially closer to the electron. The charge of the electron will be screened by this charged cloud surrounding it, and it is only at very short distances that this cloud of positrons that screen the electron will be penetrated to reveal the bare charge of the electron.

In QCD a similar process will occur with the quark continually emitting gluons which may then produce quark-antiquark pairs, figure 1.1b. Due to the self interaction of gluons however they will also produce gluon loops, this turns out to have an antiscreening effect as say a blue quark will be preferentially surrounded by other blue charges meaning that a low energy probe measuring the colour charge will find a colour charge that is higher than the 'bare' quark colour charge. This bare charge will only be found by moving the probe closer to the original blue quark, i.e. using a higher energy probe, this probe will penetrate the sphere of mostly blue charge and the amount of blue charged measured decreases. This resulting antiscreening of the blue colour is referred to as 'asymptotic freedom' as at such small distances two blue quarks would interact through colour fields of reduced strength and approach a state where they behave as essentially free, noninteracting particles.

1.3 The Quark Gluon Plasma

One of the predictions of QCD is that hadronic matter at high enough temperature and/or energy density could undergo a phase transition during which hadrons would 'melt' into an asymptotically free gas of quarks and gluons, the QGP, see figure 1.2 [4]. The study of the plasma should therefore shed further light on such features of

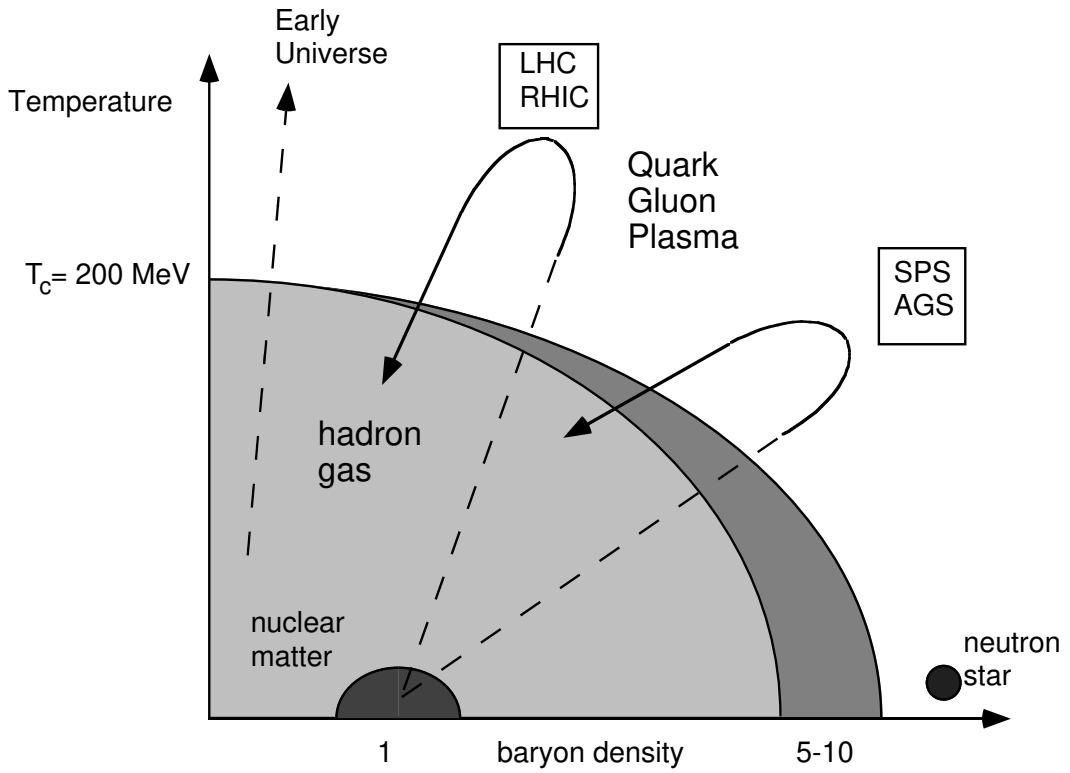

Figure 1.2: Phase diagram of the QGP.

QCD as the confinement and deconfinement of quarks and gluons under these extreme conditions. Also the existence of the plasma is a useful test of non-pertubative QCD, in that the theory will have to be looked at again if the QGP is proved not to exist in the predicted energy density and temperature domain.

In astrophysics it has been postulated that the centre of a neutron star may be dense enough for there to exist a QGP [5]. Also up to 10^{-5} seconds after the Big Bang , when the temperature was above 200 MeV, the Universe may have existed as a QGP. If indeed the Universe was a QGP in its very early stages the behaviour of the plasma as the universe cooled down and began to hadronise could have played a

part in the current inhomogeneities of the universe, with matter clumped together in galaxies etc [6].

Physicists worldwide are looking for evidence of the QGP using heavy ion interactions to create the conditions required for the plasma formation. The WA94 collaboration is looking at strangeness enhancement in sulphur-sulphur collisions as a signal of the formation of a QGP.

1.4 Heavy Ion Interactions at Relativistic Energies

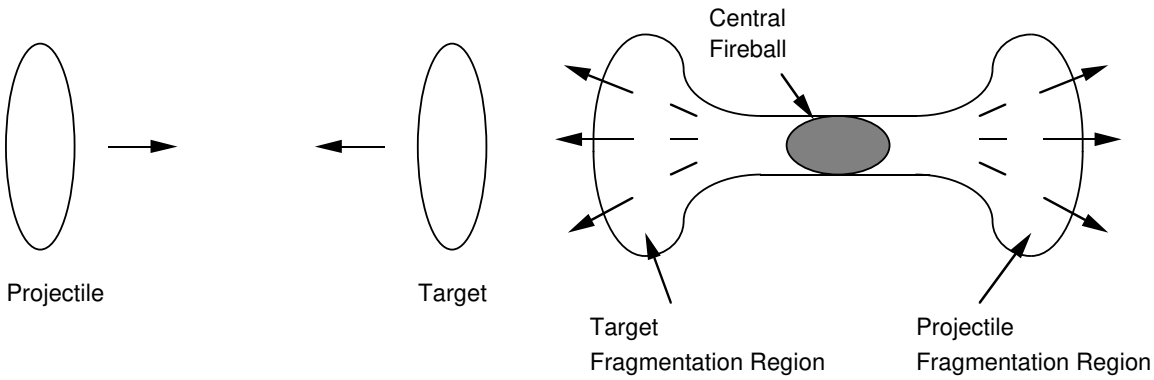

Figure 1.3: Before and after the collision of 2 relativistic sulphur nuclei.

In figure 1.3 one can see a schematic representation of a collision of heavy ions in the centre of mass frame; at the ultra relativistic energies involved they resemble two colliding discs. Between the forward and backward fragmentation region a flat region of rapidity density opens up. The rapidity variable, Y^* is defined as,

$$Y^* = \frac{1}{2} ln \frac{E^* + p_L^*}{E^* - p_L^*}$$

where E^* is the centre of mass energy and p_L^* the centre of mass momentum along the beam direction. Within this 'central' region it is hoped a QGP will be formed out of the hot fireball created by the collision.

1.5 Evolution of the plasma

If a QGP does indeed form in the collision it is expected to evolve as shown in figure 1.4 [7]. The cone is dependent on the trajectories of the projectile and target nuclei. The fireball from which the QGP may originate is expected to last for around 10^{-23} seconds ($\sim$ 10 fm/c). After this time the temperature has dropped below the critical temperature due to expansion and radiation of particles from the surface. The fireball matter then begins to hadronise into several hundred mesons and baryons, which will eventually stop colliding and will fly apart to be recorded in detectors placed at reasonable distances from the target.

1.6 QGP Signals

Initially, the density of the hadronic phase will be very high and only drop during further expansion. Until the density has become so low that the average inter-particle spacing is larger than the range of the strong interactions the hadrons in the fireball will interact violently. The experimentalist, therefore, needs to look for a signature that does not change during this cooling down stage, that is one which is unchanged by the strong interaction. Several of these signatures are outlined in this section, whilst strangeness enhancement is explained in more detail in the next section as this is the signal WA94 is using to probe for the QGP.

1.6.1 Direct photons

Photons which are produced in processes such as,

$$q\overline{q} \rightarrow \gamma\gamma$$

$$gq \rightarrow \gamma q$$

rather than in resonance decays are known as direct photons. These photons interact electromagnetically, and because the electromagnetic force is much weaker than the strong nuclear force observed by particles carrying colour charge, the mean free path

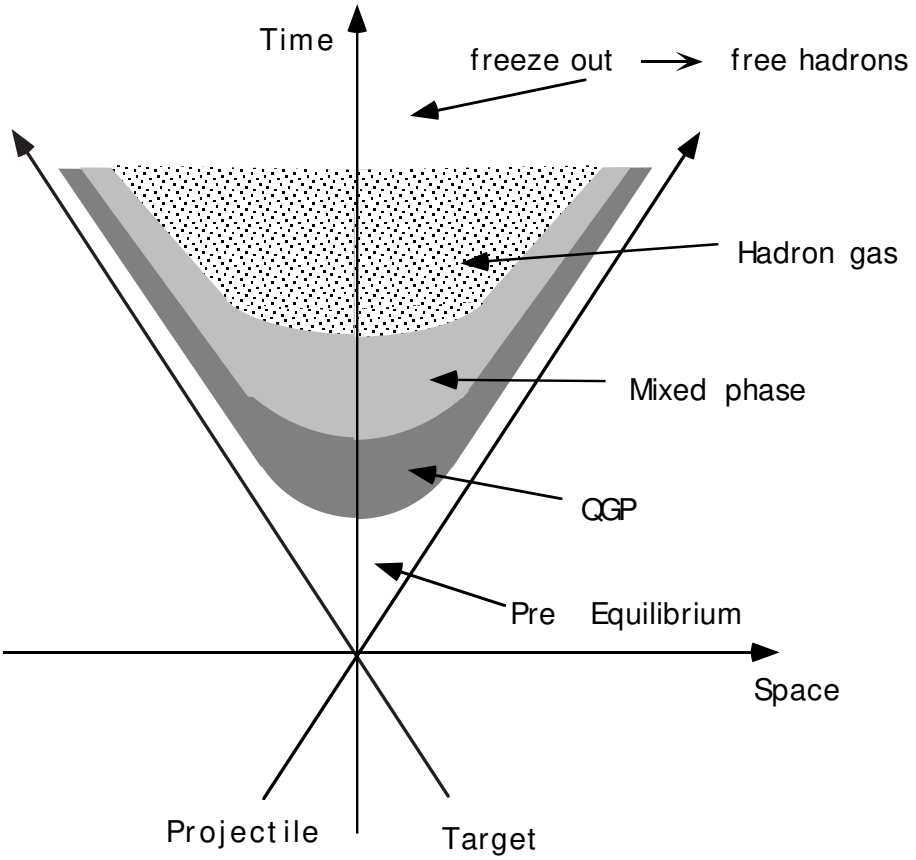

Figure 1.4: An idealized space time diagram of the evolution of the QGP after a relativistic heavy ion collision.

of a particle interacting only electromagnetically is much longer than the mean free path of a strongly interacting one. Therefore photons which are produced in a QGP would have a good chance of reaching a detector without undergoing secondary interactions. However very large backgrounds from hadronic decays into photons, particularly $\pi^0 \rightarrow \gamma\gamma$ and $\eta \rightarrow \gamma\gamma, 3\pi^0$, mean that results from direct photon

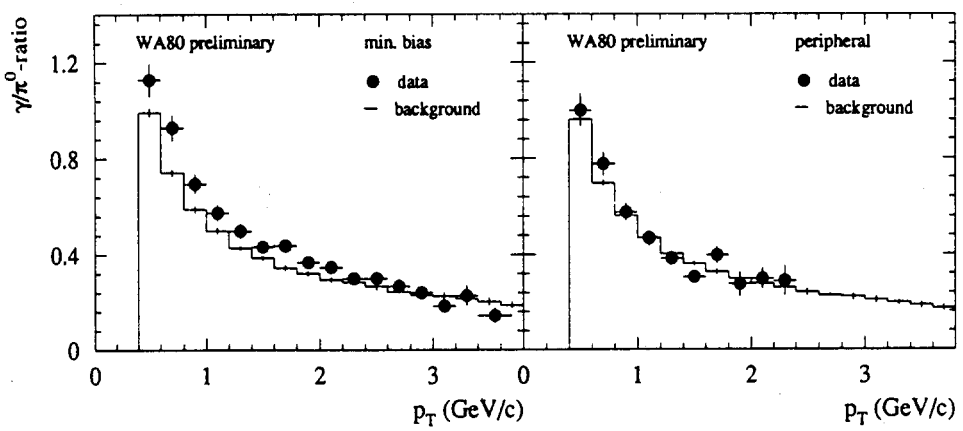

Figure 1.5: γ/π^0 ratio as a function of p_T for central and peripheral S+Au data at 200 A GeV. The dots represent the inclusive photon data, the histograms all photons from hadronic background sources.

analysis had been rather inconclusive [8]. However recently, with an increase in statistics, WA80 have observed an excess of photons in central (minimum bias) S+Au collisions over hadronic sources, with up to a two standard deviation effect for $p_T < 2$ GeV/c. Whilst for peripheral S+Au data the photon yield is completely described by hadronic sources [9], as seen in figure 1.5.

1.6.2 Dileptons

Whilst leptons do not interact strongly the study of single leptons suffers due to the high background from hadronic decays; however the observation of high energy lepton pairs, particularly e^+e^- and $\mu^+\mu^-$, seems to be more promising [10] . Dileptons are produced in the plasma via quark-antiquark electromagnetic annihilations, the background is much reduced compared to single lepton production, but is still

a problem, the main process being $\pi^+\pi^- \rightarrow l^+l^-$.

1.6.3 J/Ψ and Ψ′ Suppression

Heavy vector meson spectroscopy has been suggested as a tool for looking for a QGP [11], in particular $J/\Psi \rightarrow \mu^+\mu^-$. The J/Ψ meson is a bound state of a charmed and an anticharmed quark ($c\overline{c}$), and it is thought that the observed yields of the J/Ψ should be lower if a QGP is formed than the yields found in hadronic interactions. In a QGP quark deconfinement occurs, i.e there are no bound states and the formation of a $c\overline{c}$ pair into a J/Ψ should be suppressed in a mechanism analogous to Debye screening. A 'fast' J/Ψ is more likely to escape before dissolving and thus there is a dependence on p_T. NA38 have observed a suppression in J/Ψ production (see figure 1.6) in oxygen-uranium and sulphur-uranium heavy ion collisions using lepton

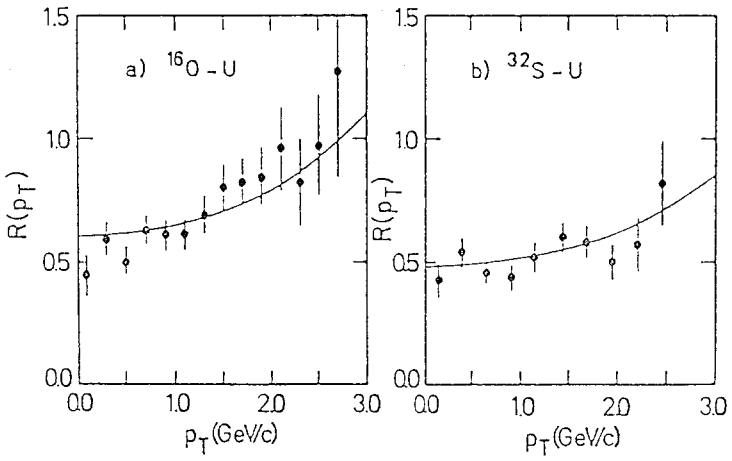

Figure 1.6: J/Ψ suppression as observed by NA38, where R is defined as the J/Ψ to continuum ratio.

spectroscopy to identify the J/Ψ. The predicted p_T dependence of the suppression is also seen. Although these results are consistent with the formation of a QGP they are unfortunately also consistent with various rescattering and absorption models which do not need to introduce a new phase of matter [12].

If a QGP is formed the survival probability of a Ψ′ compared to a J/Ψ has been calculated to be less [13], with the Ψ′ more likely to be suppressed than the J/Ψ

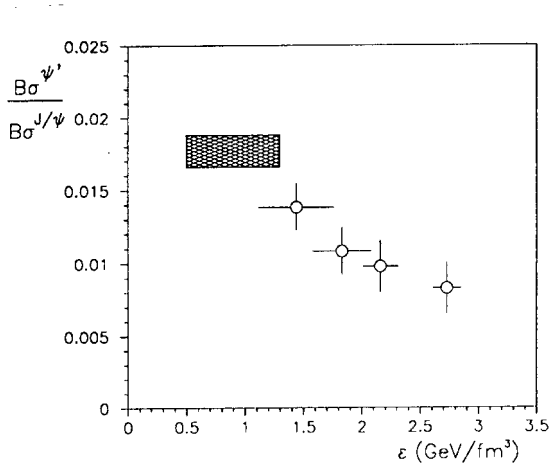

Figure 1.7: Ψ' suppression relative to J/Ψ as ϵ increases (the box shows the average value for p-A interactions).

when the energy density reached in the collisions increases. Figure 1.7 shows the ratio between Ψ' and J/Ψ yields as a function of the energy density of the collision, a clear decrease of this ratio is seen as the energy density increases [14, 15].

1.7 Strangeness Enhancement

The QGP is far too short lived for the weak interaction to be of importance, therefore strangeness, once produced, can only be destroyed if a strange quark and a strange antiquark meet and annihilate. This is unlikely unless there is an abundance of strange quarks; thus the amount of strangeness observed long after the reaction is over is expected to be a good signal of the early stages of the evolution of the QGP [16]. It has been put forward that there will be a general enhancement of strange particle production (in particular an enhancement of multistrange antibaryons) in nuclear collisions involving the formation of a QGP [17]. The reasons for this are outlined below.

The energy threshold required to produce a $s\overline{s}$ pair is just twice the effective strange quark mass, $2m_s \simeq 300$ MeV. Since the temperature of a QGP is expected to be around 200 MeV it is easy to produce $s\overline{s}$ pairs from gg and $q\overline{q}$ annihilation in the plasma. However in hadronic matter the lowest energy process which produces

strangeness is the associated production mechanism

$$\pi^- p \rightarrow \Lambda K^0$$

with a total centre-of-mass energy of about 1.6 GeV, requiring a minimum centre-of-mass momentum of about 520 MeV. The process

$$pp \rightarrow p\Lambda K^+$$

also gives rise to strangeness, with a centre-of-mass energy of around 2.55 GeV, and a threshold centre-of-mass momentum of about 860 MeV. To produce baryons which contain strange antiquarks the minimal energy reactions to produce a $\Lambda\overline{\Lambda}$ pair is via

$$pp \rightarrow pp\Lambda\overline{\Lambda}$$

with a centre-of-mass energy of about 4.1 GeV. Therefore the background production rate of strangeness is extremely low.

Also in heavy ion interactions the initial abundances of u and d quarks from the ions nuclei are high therefore the Pauli Exclusion Principle limits further production of these quarks. The production of $s\overline{s}$ pairs, mostly by gluon gluon fusion, is thus favoured.

The amount of strangeness in the QGP will continue to rise until either the plasma starts to hadronise or strange quarks become so abundant that the rate of production of $s\overline{s}$ pairs equals the rate of $s\overline{s}$ annihilations i.e.

$$\sigma(gg \rightarrow s\overline{s}) + \sigma(q\overline{q} \rightarrow s\overline{s}) = \sigma(s\overline{s} \rightarrow gg) + \sigma(s\overline{s} \rightarrow q\overline{q}).$$

At this stage the strange phase space is said to be saturated, the amount of strangeness remains constant.

The obvious question arises - does the fireball from which the QGP may arise exist long enough for this saturation to occur? The time needed for saturation of the strange phase space in a QGP via gluon fusion has been calculated [18] and figure 1.8 shows the number density of strange quarks in the plasma as a function of time for different plasma temperatures. As can be seen in figure 1.8 the time taken for

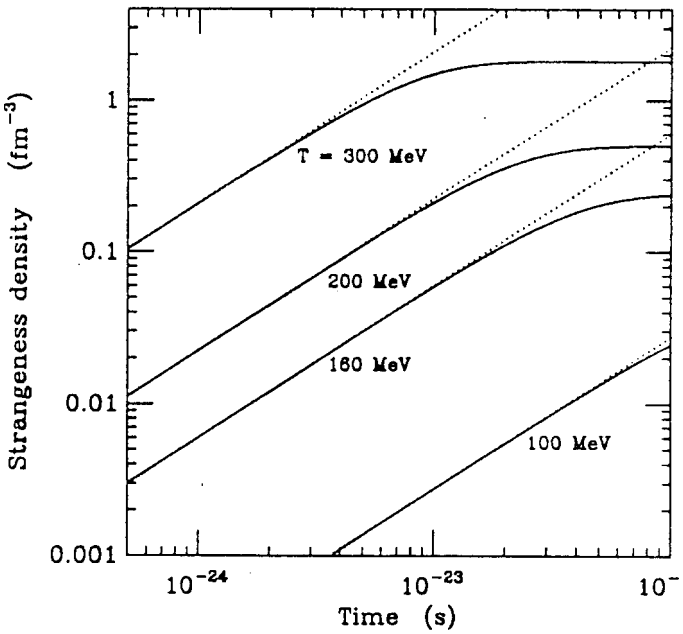

Figure 1.8: Time development of the strangeness content of the Quark Gluon Plasma at different temperatures. The saturation time at 200 MeV is about 10^{-23}s. Dashed lines indicate no $s\overline{s}$ annihilations.

the available phase space to become saturated is only a few fm/c, for comparison the rate for strange pair production in conventional hadronic processes, occurring within a hadron gas [2], $(h_1 + h_2 \rightarrow h_3^s + h_4^{\overline{s}})$ is much slower (of order of a few 10 to 100 fm/c) [19]. As stated earlier the lifetime of the fireball is estimated to be of the order of 10 fm/c. Thus, while the typical lifetime of the hot and dense interaction region created by the collision may be long enough for strangeness saturation to occur if a QGP is formed, the absence of saturation would result in a similar suppression of strange particles compared with nonstrange particles as seen in usual hadron-hadron collisions.

In summary, due to the high threshold energies required to produce strangeness in hadronic reaction coupled with the longer time needed to reach saturation of

[2] A hadron gas is a volume of highly excited nuclear matter made up of quarks and gluons confined within hadrons.

conventional strangeness production, strange baryons would provide a good signal of the existence of the plasma. Multistrange baryons and antibaryons would therefore be an even better signature as they are more difficult to form in hadronic interactions than singly strange baryons.

1.8 WA85 Experiment

The WA85 experiment [20], the predecessor of WA94, was performed using the CERN Omega Spectrometer with a 200 A GeV/c beam of S^{32} ions incident on a tungsten target. The experiment has taken data from 1987 and the raw yields of strange particles observed by WA85 are summarised in table 1.2 [21].

The p + W data was taken by WA85 for comparison with their S + W data, and in fact a strangeness enhancement is seen with respect to negatively charged particles (mostly pions) when going from p + W to central S + W interactions [22], see table 1.3.

Transverse mass distributions provide an insight into the temperature of the central fireball. Particles with fixed rapidity coming from a thermal source are expected to have a transverse mass distribution given by

$$\frac{1}{m_T}\frac{dN}{dm_T} \sim \exp^{-\beta m_T},$$

where β is the inverse temperature of the source and m_T is the transverse mass defined by $m_T = \sqrt{p_T^2 + m^2}$. For particles with varying rapidity coming from a thermal source the above expression becomes

$$\frac{1}{m_T^{\frac{3}{2}}}\frac{dN}{dm_T} \sim \exp^{-\beta m_T}.$$

Figure 1.9 shows the m_T distributions for a) Λ and Ξ, and b) $\overline{\Lambda}$ and $\overline{\Xi^-}$ hyperons, obtained by WA85 [21], in the rapidity interval $2.3 < Y_{LAB} < 2.8$. The inverse slopes are given in table 1.4. As can be seen from table 1.4 the inverse slopes of the m_T distributions are around 230 MeV for these hyperons.

The strange particle production ratios obtained by WA85 from their 1990 data are shown in table 1.5. Hyperon ratios obtained by NA36 [23] (using S + Pb colli-

Table 1.2: V^0 and cascade yields from the WA85 1990 SW, 1987 SW, and 1988 pW runs.

Candidate	1990 SW data	1987 SW data	1988 pW data
Λ	51600	13300	3200
$\overline{\Lambda}$	13600	3400	1000
Ξ^-	500	108	80
$\overline{\Xi^-}$	200	44	20

Table 1.3: Strange particle enhancement w.r.t. h^- multiplicity from pW to central SW interactions as observed by WA85.

Particle	$\frac{(\text{particle}/h^-)_{SW}}{(\text{particle}/h^-)_{pW}}$
Λ	2.02 ± 0.20
$\overline{\Lambda}$	1.64 ± 0.16
K^0	1.33 ± 0.13

Table 1.4: Inverse slopes for hyperons in SW interactions (MeV) obtained by WA85.

Particle	Inverse slope (MeV)
Λ	232 ± 3
$\overline{\Lambda}$	230 ± 6
Ξ^-	239 ± 11
$\overline{\Xi^-}$	234 ± 15

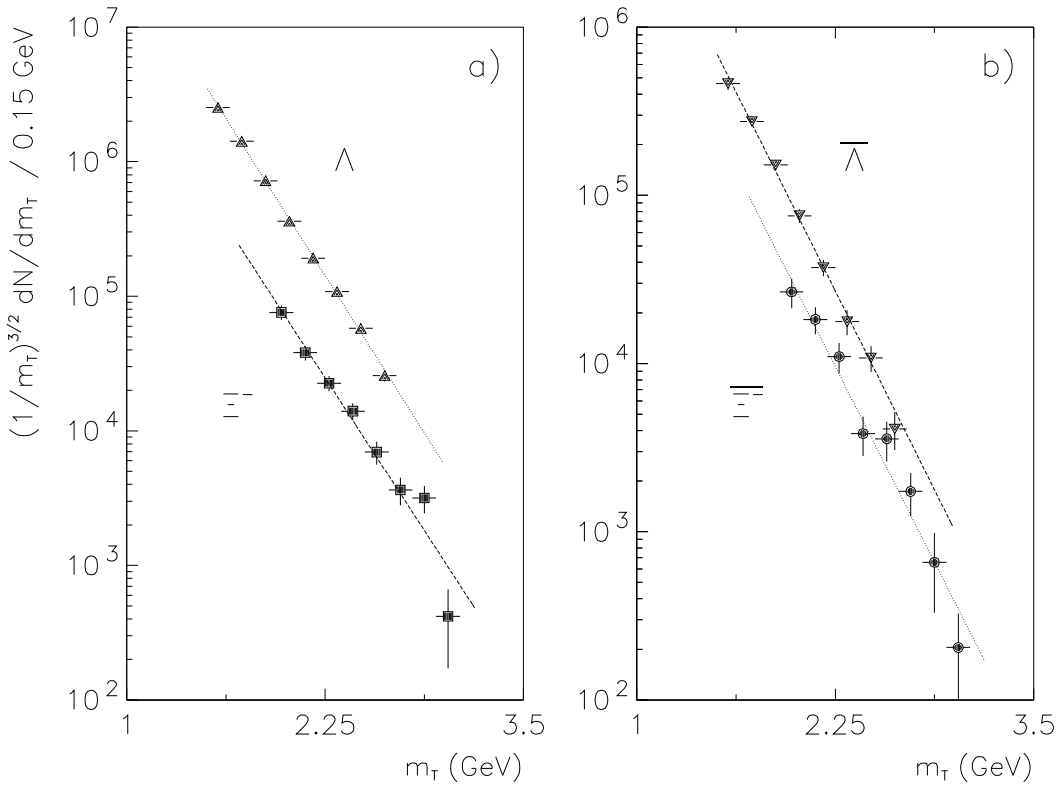

Figure 1.9: $\frac{1}{m_T^{\frac{3}{2}}} \frac{dN}{dm_T}$ vs m_T for a) Λs and Ξ^-s, and b) $\overline{\Lambda}$s and $\overline{\Xi^-}$s, obtained by WA85.

Table 1.5: Summary of the different particle ratios, and their respective acceptance intervals, obtained by WA85.

Ratio	Value	Acceptance region
K^0_S/Λ	1.4 ± 0.1	$2.5 \leq Y_{LAB} \leq 3.0, 1.0 \leq p_T \leq 2.5$
$\overline{K^0_S}/\overline{\Lambda}$	6.4 ± 0.4	same
$\overline{\Lambda}/\Lambda$	0.20 ± 0.01	$2.3 \leq Y_{LAB} \leq 3.0,\ 1.2 \leq p_T \leq 3.0$
$\overline{\Xi^-}/\Xi^-$	0.45 ± 0.05	same
Ξ^-/Λ	0.095 ± 0.006	same
$\overline{\Xi^-}/\overline{\Lambda}$	0.21 ± 0.02	same

sions at 200 GeV/c per nucleon) are compatible, within one or two standard deviations, with these ratios, however a direct comparison between the two is not possible due to the different phase space windows over which they have been measured. To compare with data from other experiments, WA85 have calculated the ratios Ξ^-/Λ and $\overline{\Xi^-}/\overline{\Lambda}$ in the window $2.3 < Y_{LAB} < 2.8$ and $1.0 < p_T < 2.0$ GeV/c. These ratios are shown in figure 1.10 together with those measured by other experiments in e^+e^-, $\overline{p}p$ and pp interactions. While the ratio Ξ^-/Λ from S + W is compatible with those from other interactions, the $\overline{\Xi^-}/\overline{\Lambda}$ ratio is over three times greater than that measured in pp interactions, corresponding to a four standard deviation effect.

Until recently the Ω baryon, which is composed of three strange quarks and therefore of particular interest with regards to the formation of a QGP, had not been observed in heavy ion interactions owing to its low cross section and acceptance. In their 1990 data however WA85 have identified the decays $\Omega^- \rightarrow \Lambda + K^-$ and $\overline{\Omega^-} \rightarrow \overline{\Lambda} + K^+$ [24]. Figure 1.11 shows the effective mass distribution of the Ω^- and the $\overline{\Omega^-}$ candidates. As can be seen there is a clear peak in the Ω mass region with little background (dotted line). This combinatorial background is obtained by the merging of every Λ from the data with the non Λ tracks of the previous Λ event. Subtraction of this background leaves 7.0 ± 3.6 Ω^-s and 4.0 ± 2.0 $\overline{\Omega^-}$s, which gives the ratio $\Omega^-/\overline{\Omega^-} = 0.57 \pm 0.41$. The production ratio $(\Omega^- + \overline{\Omega^-})/(\Xi^- + \overline{\Xi^-})$ has

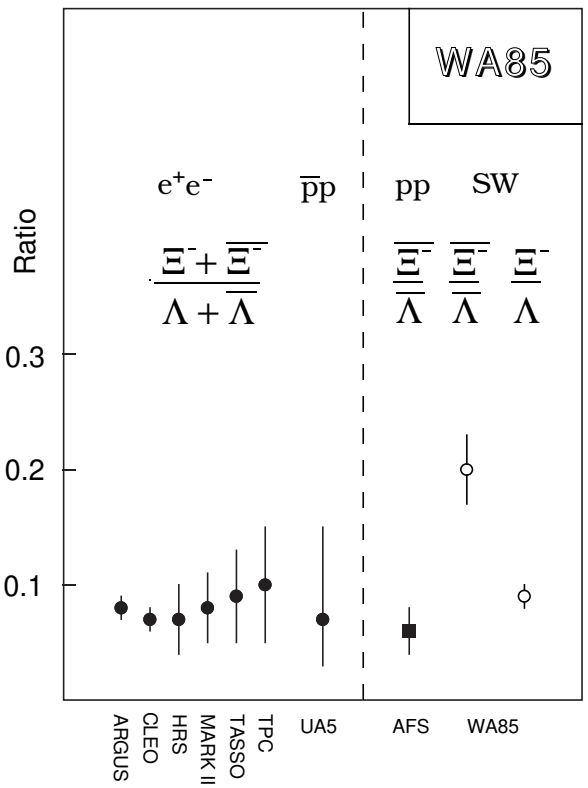

Figure 1.10: Ξ^-/Λ and $\overline{\Xi^-}/\overline{\Lambda}$ ratios for different experiments.

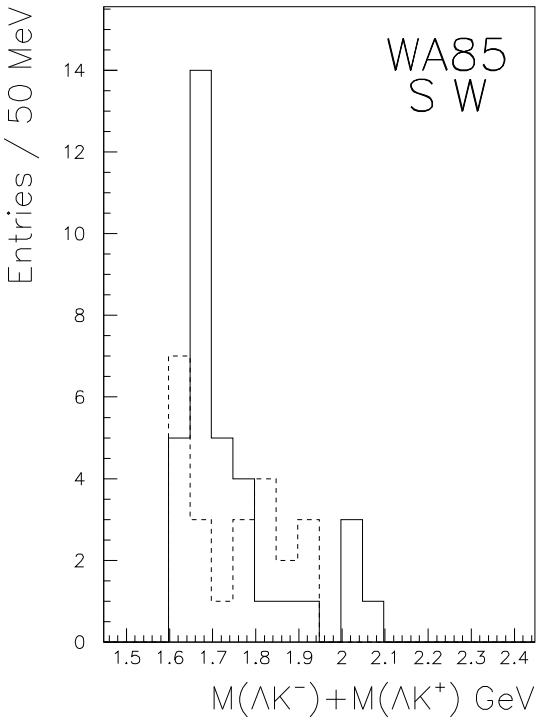

Figure 1.11: Effective mass distributions of $\Omega^- + \overline{\Omega^-}$candidates in SW interactions.

been calculated to be 0.8 ± 0.4 in the overlapping region $2.5 < y < 3.0$ and $p_T > 1.6$ GeV/c [25]. The $\overline{\Omega^-}/\overline{\Xi^-}$ ratio was measured in central rapidity and $p_T > 1.4$ GeV/c in pp interactions at the CERN ISR by the AFS collaboration [26]. They obtained a 90% confidence level upper limit of $\overline{\Omega^-}/\overline{\Xi^-} < 0.15$ which is much lower than the value measured by WA85.

1.9 Summary

The prediction of QCD that at high enough energy density and temperature a phase transition may occur from hadronic matter to a QGP is of particular interest to particle physicists and astrophysicists alike. Several signatures of the QGP have been suggested by theoreticians and from 1987 heavy ions have been accelerated at both BNL and CERN to try and create the conditions required for the formation of a QGP, the experimental collaborations involved in this work are given in table 1.6. The WA94 experiment uses a sulphur beam on a sulphur target and carries on the work of WA85, which saw an enhancement of strange particle production of up to a factor of 2 in central SW interactions with respect to pW interactions, where no QGP formation is expected (table 1.3). Also they see an increase in the ratio of $\overline{\Xi}/\overline{\Lambda}$ in SW interactions compared to pp interactions, i.e. an increased yield of multistrange antibaryons is observed, as shown in figure 1.10.

Table 1.6: Main collaborations active in the heavy ion physics field

Collaboration	Main detectors	Physics topics
BNL	(14.6 GeV/c per nucleon O^{16} and Si^{28} ions)	
E802	Magnetic Spectrometer	$\pi^{\pm}, K^{\pm}, p, \overline{p}$
E810	Time projection chamber (TPC)	V^0 and charged hadron production
E814	Calorimeter	Fragmentation of projectile and E_T distributions.
CERN	(200 GeV/c per nucleon O^{16}, S^{32} and Pb^{207} ions)	
NA34	Muon Spectrometer & calorimeter	$\pi^{\pm}, K^{\pm}, \mu^+\mu^-, E_T$
NA35	Streamer chamber	K^0, Λ and $\overline{\Lambda}$ production
NA36	Time projection chamber	$V0$, charged hadrons and Ξ^- and $\overline{\Xi^-}$ production
NA38	Muon Spectrometer	Dimuons, J/Ψ and ϕ production
NA44	Focussing Spectrometer	Interferometry, charged hadrons
NA45	e^+e^- Spectrometer, RICH	e^+e^-
WA80	Plastic ball, e.m. calorimeter	π^0 and γ production and target fragmentation
WA85	Ω Spectrometer, MWPCs	K^0, Λ, $\overline{\Lambda}$, $K^{\pm}$, Ξ^-, $\overline{\Xi^-}$, Ω^- and $\overline{\Omega^-}$ production.
WA94	Ω Spectrometer, MWPCs, RICH	K^0, $K^{\pm}$, Λ, $\overline{\Lambda}$, Ξ^- and $\overline{\Xi^-}$ production.
WA97	Ω Spectrometer, RICH, silicon telescope	p, $\overline{p}$, K^0, $K^{\pm}$, Λ, $\overline{\Lambda}$, Ξ^-, $\overline{\Xi^-}$, Ω^- and $\overline{\Omega^-}$ production.

Chapter 2

The Apparatus

2.1 Introduction

The WA94 experiment [27, 28], like WA85, was set up to measure strange and multistrange baryons and antibaryons produced in heavy ion interactions in the central rapidity region with medium to high p_T. The first stage of the experiment used a beam of sulphur ions of energy 200 GeV per nucleon incident on a sulphur target (unlike WA85 which used a tungsten target). This stage was undertaken in the latter part of 1991 and in 1993 data were taken using a 200 GeV beam of protons to be used for comparison with the 1991 data. The experiment was performed using the Omega spectrometer in the West Experimental Area at CERN. This spectrometer is a multi-user facility and to some extent it can be changed to suit the experiment using it [29]. This thesis concerns the analysis of the 1991 sulphur-sulphur data and the experimental set up used in this run will be discussed in this chapter.

Before describing the apparatus used in this 1991 run, the philososphy behind it will be discussed. As said in chapter 1, it is believed that heavy ions colliding at ultrarelativistic energies offer the most satisfactory way of achieving the conditions required for the formation of a Quark Gluon Plasma. However this is a hostile environment for measuring e.g.

$$\Xi^- \rightarrow \Lambda + \pi^- \rightarrow p + \pi^- + \pi^-$$

where one is looking for 3 specific tracks out of some 300 tracks produced in central sulphur-sulphur interactions.

Two methods have been developed to study strangeness production in heavy ion interactions. One approach is to attempt to measure everything, the advantage of this being that one can get complete information per event, whilst the disadvantage is the large amount of combinatorial background present, as seen in figure 2.1 which shows the interaction of a sulphur beam particle at 200 GeV/c per nucleon with a sulphur target as seen by the NA35 streamer chamber.

To reconstruct a Ξ^- decay one requires a pair of oppositely charged tracks to intersect to form a Λ which when reconstructed traces back to an intersection with a third charged track. As the number of tracks recorded per event increases this becomes harder and harder, further more the track reconstruction efficiency will decrease as, for example, in multiwire proportional chambers where it obeys an inverse relation to the number of track hits. Also the time taken to analyse each event increases with its complexity.

An alternative approach and one taken by WA94 and WA85 is to use a specialised experimental set up to study hyperons in a narrow phase space window. Whilst this means that less information per event is gathered, the data which is obtained has less combinatorial backgound per event. The reconstruction efficiency is also higher for these events. WA94 achieves this by the use of so called 'Butterfly' geometry which is explained below. Using this geometry a typical reconstructed Ξ^- is shown in figure 2.2.

2.2 The Butterfly Principle

The ability of the so called butterfly geometry to reduce the combinatorial background can be understood by considering two tracks from the target with the same transverse momentum p_T but with different longitudinal momentum p_L, as illustrated in figure 2.3.

The tracks produced at the target are at an angle θ with respect to the beam

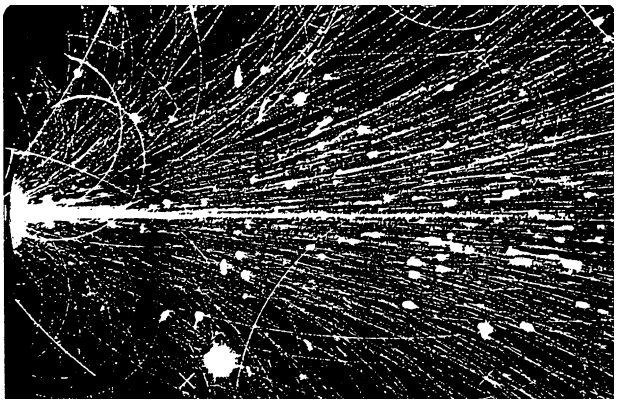

Figure 2.1: A central sulphur-sulphur event as observed in a streamer chamber (NA35 collaboration).

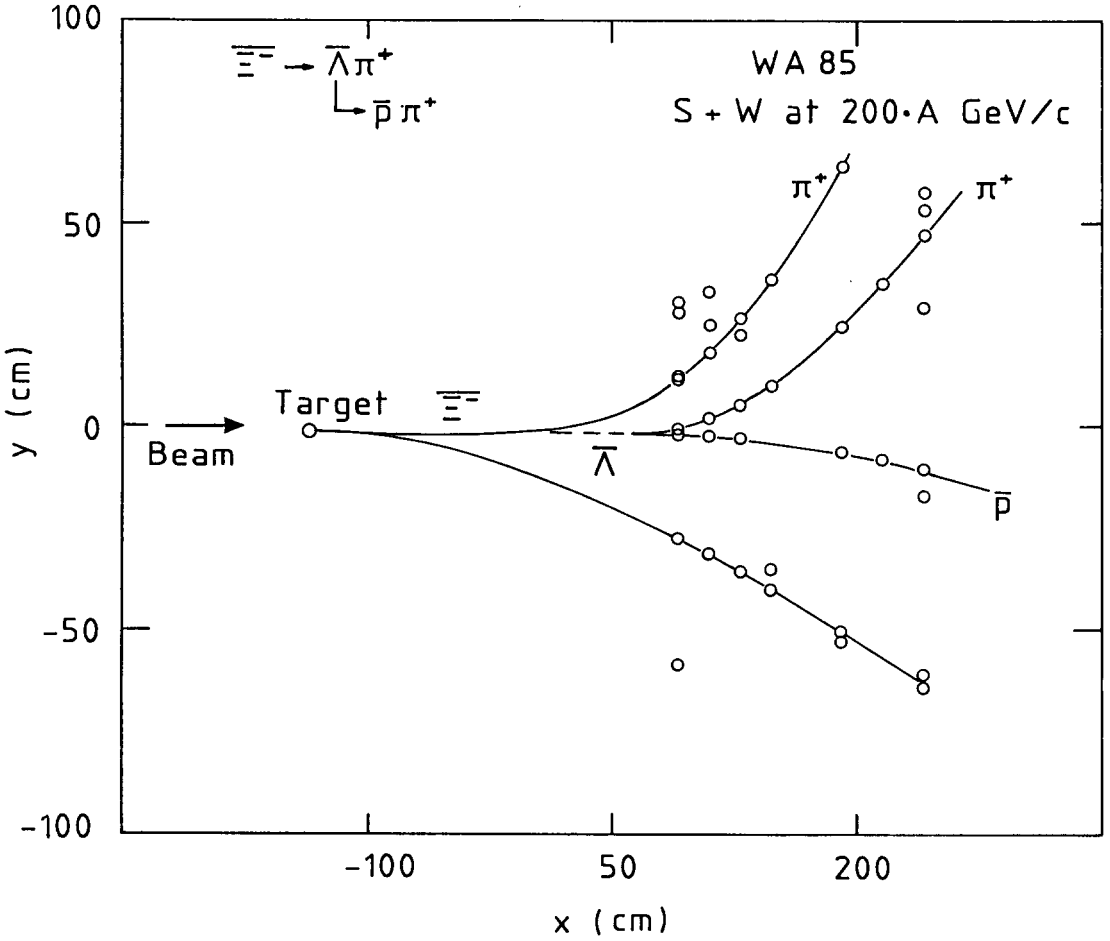

Figure 2.2: A typical Ξ^- event as seen in the OMEGA wire chambers.

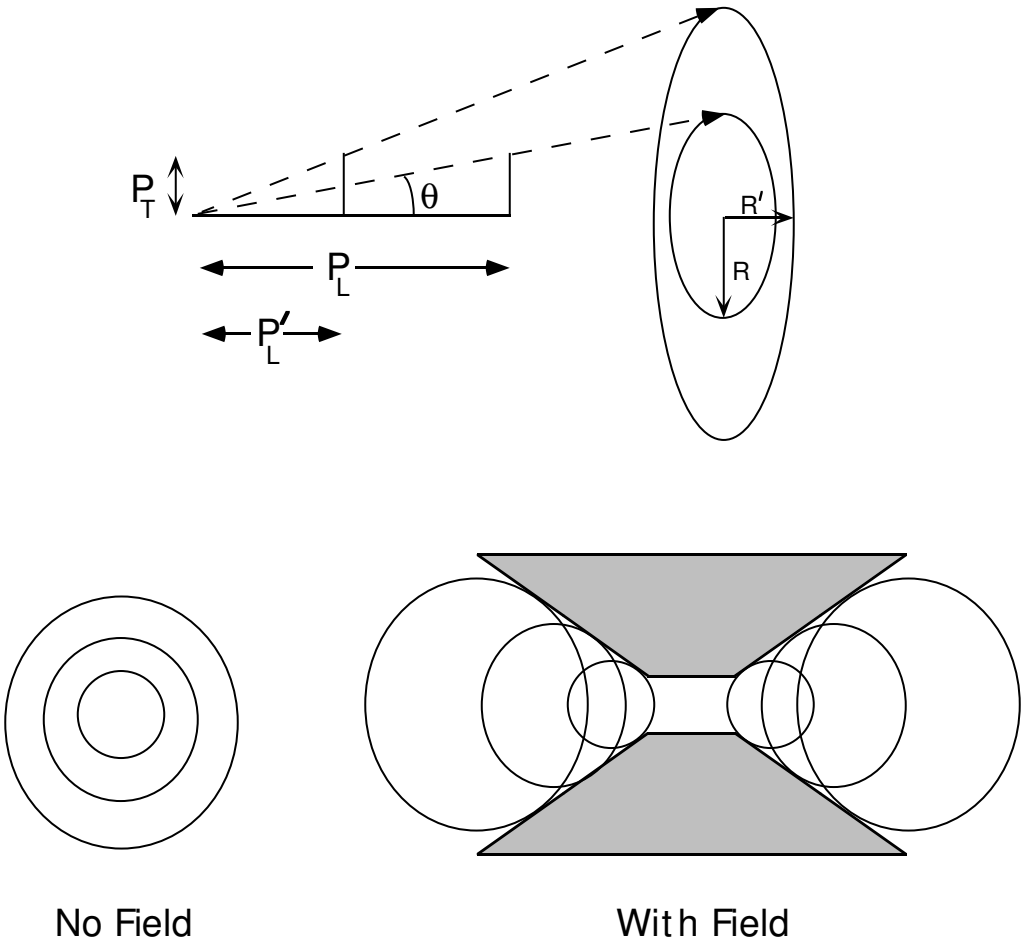

Figure 2.3: An illustration of how the butterfly principle works.

axis which depends on the ratio of p_T to p_L. At a given distance from the target particles with the same p_T but smaller p_L sweep out a larger circle. In the presence of a magnetic field the tracks are swept to one side by the interaction of the field, those tracks with the smaller p_L being swept out further than those with larger p_L. If all values of p_L for a given p_T are considered it turns out that the track loci form two v-shaped regions as shown in the figure . Therefore if one were to make only the shaded regions enveloped by the tracks sensitive there will be a cut off for which tracks below a certain p_T will not be detected[1]. To the imaginative reader the shaded regions could be seen to be similar in shape to butterfly wings hence the principle behind the reduction of tracks from the target being detected is known as the butterfly principle.

The multiwire proportional chambers used by WA94 are modified in this way although only the upper 'wing' is used, these detectors along with the others used by WA94 in 1991 are discussed in the next section.

2.3 WA94 Experimental Setup

The layout of the experimental apparatus is shown in figure 2.4. The beam to the Omega spectrometer is supplied by the CERN Super-Proton-Synchrotron, and the sulphur ions are extracted directly from the accelerator at an energy of 200 GeV/nucleon. This ultrarelativistic sulphur beam is then focussed using dipole and quadrupole magnets onto the target.

2.4 The Omega Spectrometer

The Omega Spectrometer is a multi-user facility designed for detecting and measuring interactions with several final state particles. It consists of a pair of superconducting Helmholtz coils which are capable of producing a central field of 1.8 Tesla. Into this field there may be placed the experimental target as well as an assortment

[1]This is further explained in Appendix A.

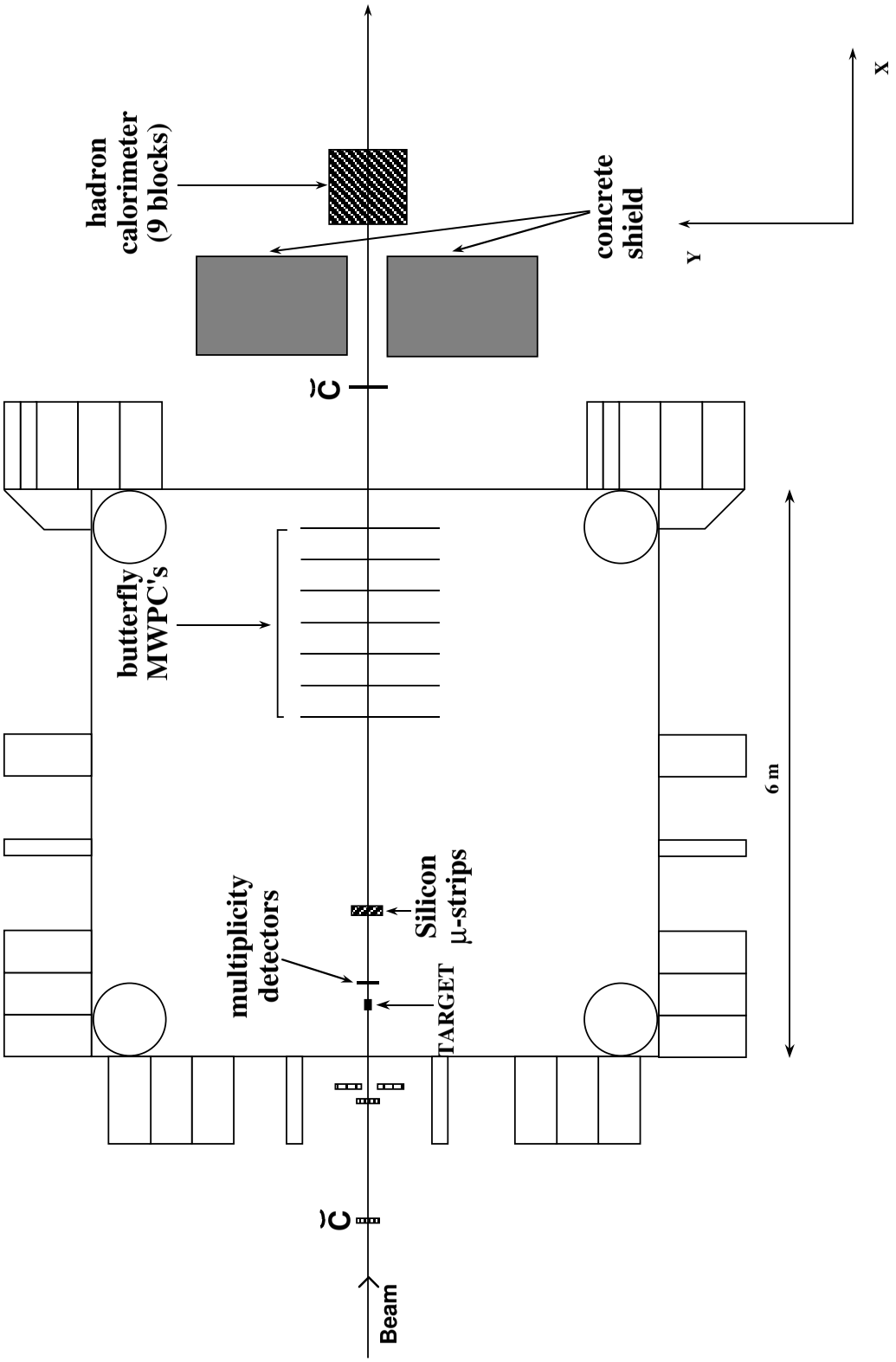

Figure 2.4: The WA94 experimental layout used in the 1991 run.

of detectors for track identification and event triggering.

In the 1991 run a thin sulphur target was used (2% interaction length). This target was placed at x_Ω = -215 cm, where x_Ω = 0 is the centre of the Omega magnet. The overall multiplicity in the central rapidity region was sampled using a system of silicon microstrips placed close to the target. Seven multiwire proportional chambers (MWPCs) were used in the 'butterfly' mode. A similar set up was used successfully by the WA85 experiment; these detectors are used for track recognition and will be explained in detail later. The positions of the target and MWPCs are different from the WA85 values so that the acceptance of the MWPCs is greatest for sulphur-sulphur interactions at central rapidity.

2.5 Silicon Microstrips

The charged particle multiplicity in the central rapidity range is sampled using two arrays of 50μm silicon microstrips, each having 512 channels arranged above and below the beam 15 cm downstream from the target. The region covered by these microstrips is in the pseudorapidity region $2.2 < \eta < 3.5$. Pseudorapidity is defined as $\eta = -\ln(\tan(\theta/2))$ and in the relativistic limit where mass becomes negligible it is equivalent to the laboratory rapidity, Y_{LAB}. Thus a count of the number of tracks originating in this region gives an insight into the centrality of collision and the amount of activity in the central fireball where the Quark Gluon Plasma may have been formed.

2.6 The Multiwire Proportional Chambers

A proportional chamber is essentially a container of gas subjected to an electric field, where a passing particle can leave a trail of electrons and ions in the gas. The charged particle debris is collected at the chamber electrodes and in the process is greatly amplified and provide an electrical signal indicating the passage of the particle. When the field is high such that secondary ionization occurs but small

enough so that the output pulse is still proportional to the number of primary ion pairs the detector operates as a proportional counter. In a MWPC a plane of anode wires is separated from two cathode planes. Each anode wire acts as an individual proportional counter, thereby allowing a big improvement in spatial resolution. The seven MWPCs used by WA94 in the 1991 run are known as the 'A Chambers'. These A chambers consist of three planes of wires (U,V,Y) where Y planes are vertical in the Omega system; the U and V planes are inclined at $+10.14^o$ and -10.14^o to the vertical respectively. Each plane contains 752 anode wires spaced at 2mm intervals. The gas used is an argon, isobutane, freon and ethanol mixture. The nearest chamber to the target, A1, is at 71 cm downstream from the centre of Omega; the 6 other chambers being placed at x_Ω = 90,109,147,190,215 and 250 cm.

The 'butterfly' shape was produced by modifying the cathode planes which consist of a 12 μm mylar foil coated with graphite paint. By removing a narrow band of this paint an electrically insulated region is created whose shape is given by the butterfly principle. The active area within this band is held at the chambers' working potential of around 5 kV whilst the remaining part is held at about 0.5 kV lower than this. This prevents tracks being recorded outside of the butterfly region but is close enough to the potential in the adjacent area so as to avoid break-down of the insulation. Figure 2.5 shows an exploded view of a section through one of the of the omega A MWPCs, the first cathode plane showing a schematic representation of how the A chambers are sensitized, the white region showing where the graphite has been removed, also shown are the three planes of wires (U,Y,V) each lying between the cathode planes.

The area chosen to be regionally sensitized is one in which particles from the target will only be detected if they have a $p_T > 0.6$ GeV/c. Strange hadrons with medium to high p_T are expected to originate in the fireball during the earlier stage of its evolution and thus allow a more direct view of the hottest and most dense stages of the interaction rather than looking at the large number of particles produced at low p_T during hadronisation. Therefore although WA94 does not record many of the tracks produced in the interaction we have a good acceptance over the region

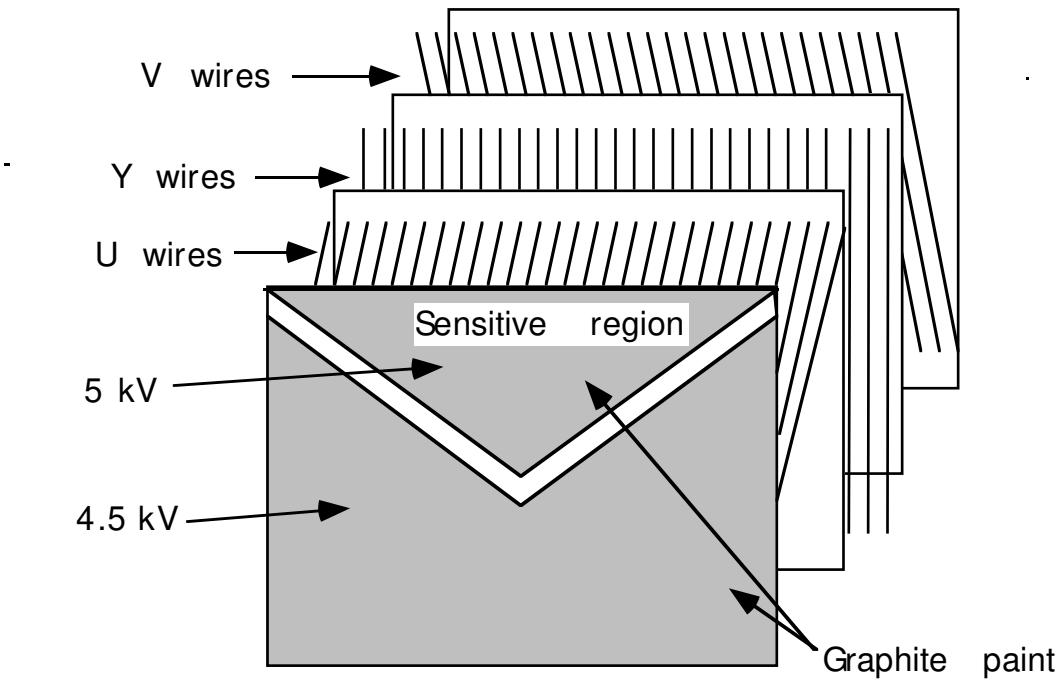

Figure 2.5: Exploded view of a section through one of the Omega A MWPCs.

that is of most interest to those studying the Quark Gluon Plasma. Also, due to the low number of tracks recorded, the data from these MWPCs can be read out quickly, hence WA94 takes many more triggers than those heavy ion experiments which record more tracks per event.

2.7 The Trigger

Figure 2.6 shows the trigger detectors used in the 1991 run. The detectors S2 and V0 are quartz Cerenkovs, whilst S3 is a scintillator. V2 and V3 are veto scintillators (scintillators with a small hole for the beam to pass through). S2, S3 and V0 are used to identify sulphur ions, S2 and S3 ensure that lighter ions are not triggered on, whilst V0 is a veto counter to make sure that a central interaction has occurred before triggering, i.e. there is no trigger when ions are detected by this counter downstream of the target.

The beam logic is also shown in figure 2.6. The definition of BEAM is a signal in S2 and S3 but no signal in the vetoes V2 and V3. The Clean Beam (CB) requirement is that only one beam particle is allowed through at a time. This is achieved by passing part of the S2 signal through an updating discriminator which resets the output on arrival of a second pulse. The effect of a second signal arriving at a time Δt during the output caused by the first signal is to lengthen the output by a time Δt. This signal will then be in anti-coincidence with the other three inputs to the clean beam coincidence unit and the event will be rejected. This is illustrated in figure 2.7 which shows the timing of the signals to the clean beam coincidence unit. The duration of the protection is set to 20 ns.

The interaction trigger (INT) requires a beam signal, no V0 signal and that the microstrip multiplicity (top and bottom) is 6 or greater. This ensures that a high multiplicity central interaction has occurred. This is further qualified by the INT.CB trigger which requires the coincidence of the clean beam and interaction triggers.

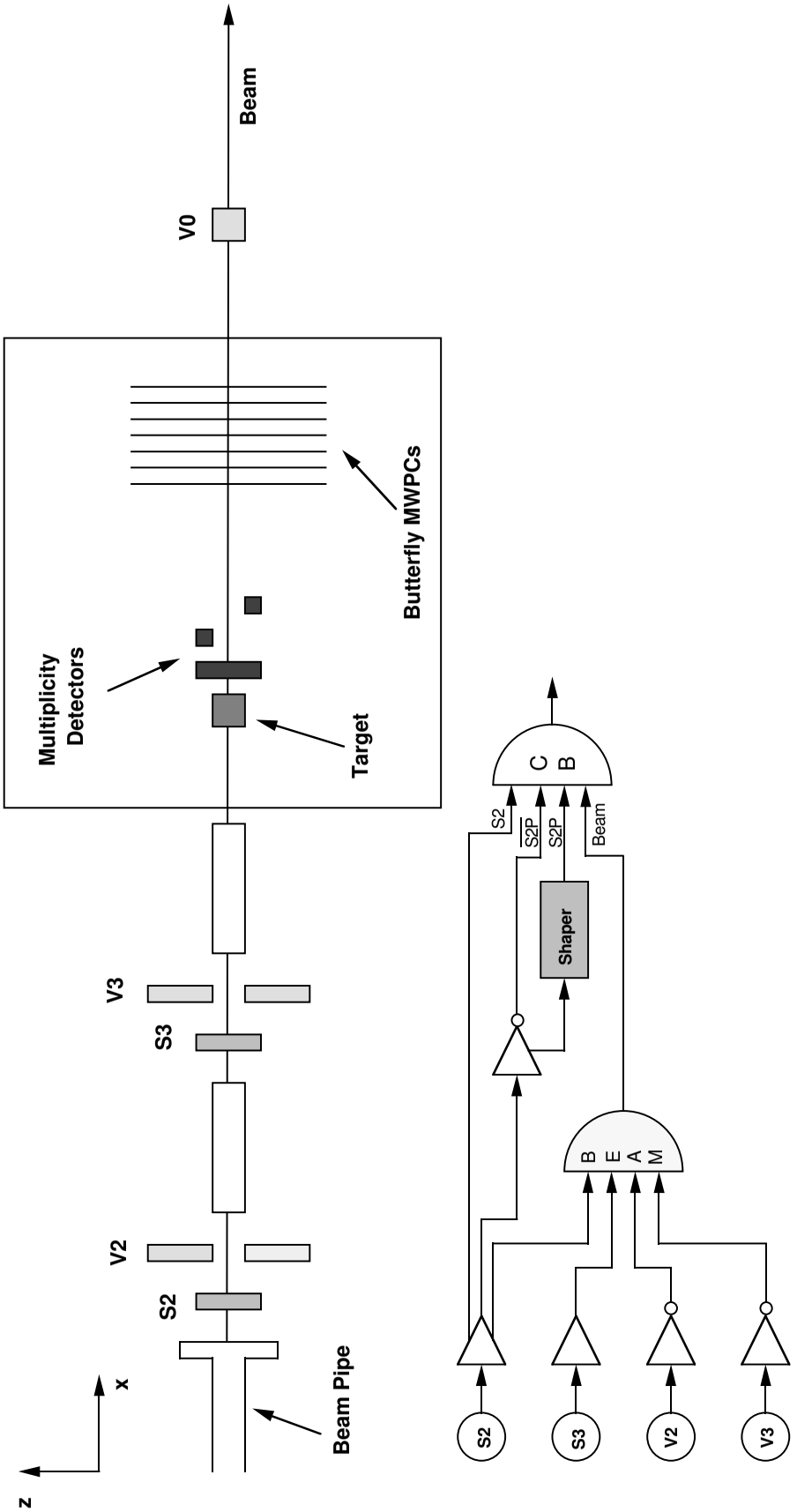

Figure 2.6: Schematic diagram of the trigger elements for the 1991 run.

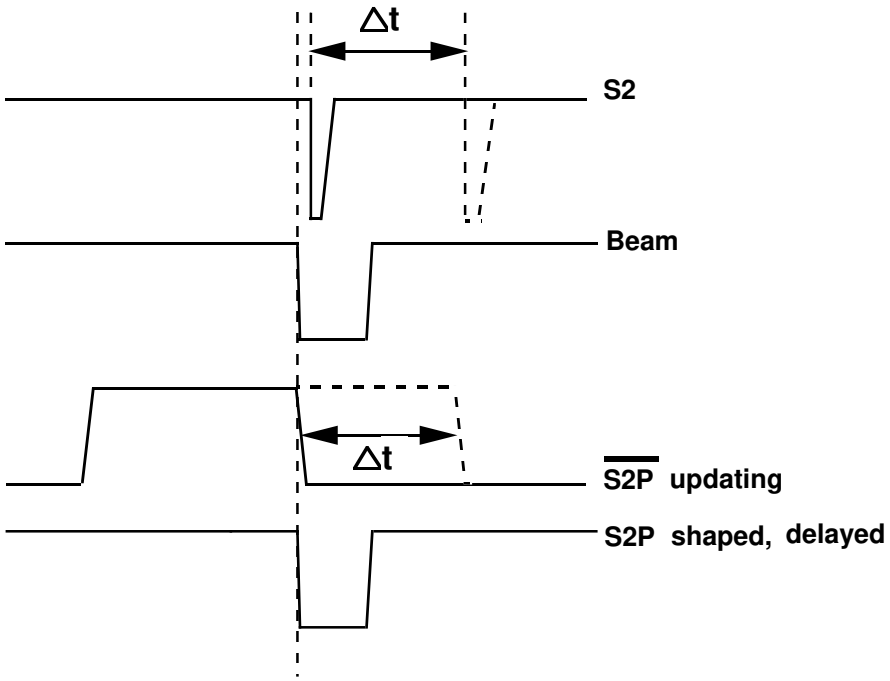

Figure 2.7: Timing of input signals to the clean beam coincidence unit, the signals in dashed lines are caused by a second incident beam particle.

2.8 Data Acquisition

The raw data taken during the run is recorded by the Omega online VAX in EPIO format, a machine independent format, used in experimental physics. It is reconstructed using a version of the program TRIDENT [31], which is modified for the particular experimental layout used by WA94. The events are written to cartridge in the form of 16 bit words, with a header block consisting of about 20 words giving information about the type of event and the length of it. Information on wire hits, cluster sizes etc. are contained in a tree structure called the ROMULUS block, which is subdivided into *branches* and *crates*. In figure 2.8 the ROMULUS structure for the WA94 1991 run is shown, showing how the information from the wire chambers and microstrips is stored. For example information on the U,Y,V planes of chamber 1 are stored at the ROMULUS addresses (1,0,22,253,17),(1,0,22,253,18) and (1,0,22,253,19).

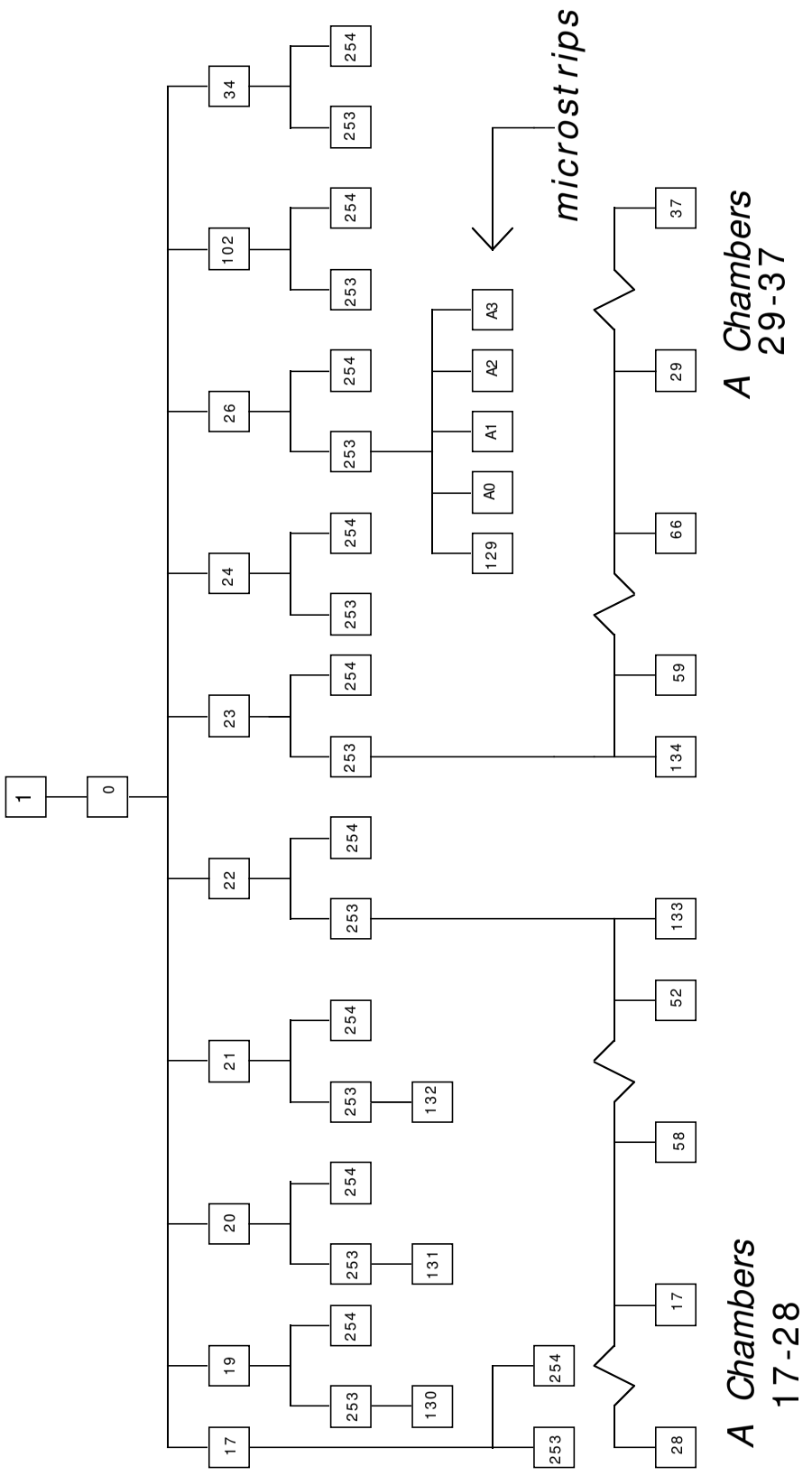

Figure 2.8: The Romulus structure for WA94, 1991 run.

Chapter 3

Reconstruction of Λ and Ξ decays

In the latter part of 1991, as stated earlier, WA94 performed an experiment using ultra-relativistic sulphur-sulphur collisions to try to create a QGP. The signal looked for by WA94 as evidence of the formation of the plasma is strangeness enhancement, i.e an increased production rate of strange (e.g Λs, $\overline{\Lambda}$s) and multistrange (e.g Ξ^-s and $\overline{\Xi^-}$s) particles in this environment compared to normal hadronic interactions.

We identify Λ and Ξ^- hyperons by the weak decays

$$\Lambda \rightarrow p + \pi^-$$

and

$$\Xi^- \rightarrow \Lambda + \pi^-.$$

Thus the signature for a Ξ^- decay is a charged track that intersects the path of a Λ, therefore before describing how a Ξ^- decay is reconstructed the identification of a Λ decay will be discussed.

3.1 Reconstructing V^0s

Once tracks have been reconstructed by TRIDENT from hits recorded in the A chambers they are then passed through a program called STRIPV0. This looks for two oppositely charged tracks intercepting at a point well separated from the target,

a few very loose cuts are also performed in order to produce a data summary tape of V^0 candidates; these are listed below.

- The tracks are traced from the chambers to the $x_\Omega = 0$ plane (where the Omega magnetic field is the most uniform). There the tracks are represented by helices and then the distance of closest approach for all permutations of oppositely charged tracks are calculated. This distance is required to be less than 1.6 cm.

- The vertex of the V^0 is then defined to lie midway between the points where the two tracks have their distance of closest approach. The x-coordinate of this vertex is required to lie in the range $-115 < x_\Omega < 71$ cm. The lower limit is because the acceptance is very low for V^0s decaying a long way from the MWPCs. This effect can be seen in figure 3.3a which shows the distribution of the vertices of possible V^0 candidates falling as the distance from the chambers increases. The upper limit is the position of the first MWPC.

- To ensure that the V^0 comes from the target the angle, ϑ, between the V^0s line of flight from the target and its momentum vector must be less than 3^o.

- It is also required that the transverse momentum of the decay tracks with respect to the momentum of the V^0, q_T, is less than 0.3 GeV/c. Real V^0s have a q_T of less than 0.2 GeV/c.

- The momentum of the V^0 must be greater than 6.5 GeV/c, Λs recorded by the chambers have a typical momentum of about 10 GeV/c.

As can be seen in figure 3.1 the effective mass M($p\pi^-$) of V^0 candidates shows a clear peak at the Λ mass even with these very loose cuts. We also require that each decay track has at least 4 space points, so that the momentum (hence the mass) of the particle can be determined more accurately. To standardise the acceptance of the apparatus it is also required that both decay tracks trace through all seven MWPCs.

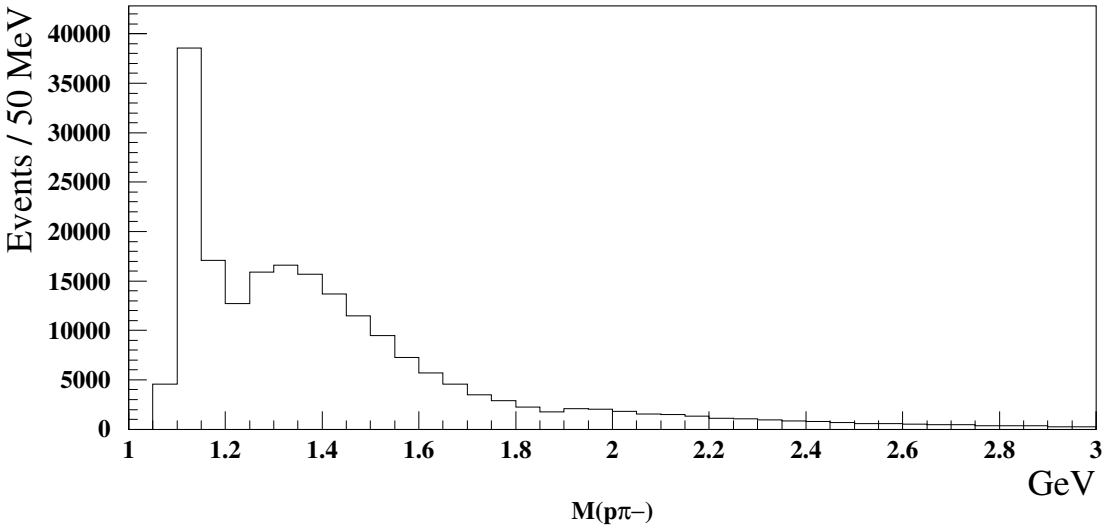

Figure 3.1: Effective mass ($p\pi^-$) of a sample of V^0 candidates after passing through STRIPV0.

3.2 Identifying Λ hyperons

Figure 3.2 is a schematic diagram of a possible Λ decay, it shows the main geometrical parameters of such a decay: the distance of closest approach of the two decay tracks, the x_Ω position of the vertex, and the impact parameters of the decay tracks at the target plane.

Figure 3.3 shows both the distribution of the V^0's vertex positions and the distribution of the V^0's vertex against the effective mass, M($p\pi^-$) of V^0 candidates. As can be seen the cut on the vertex can be tightened to be in the region of $-80 < x_\Omega < 71$ cm without losing many Λs but cutting down the noise, caused by paths of oppositely charged tracks, from the target, crossing and producing fake V^0 candidates.

Figure 3.4a shows the distribution of the closest approach of the two decay tracks to the vertex for Λ candidates after all the other cuts have been applied. One can see that the distance of closest approach between tracks can be tightened, to < 1 cm, reducing the background without losing many Λs. Figure 3.4b shows the distribution of the angle, ϑ, which was defined earlier. We reduce this cut so that V^0 candidates

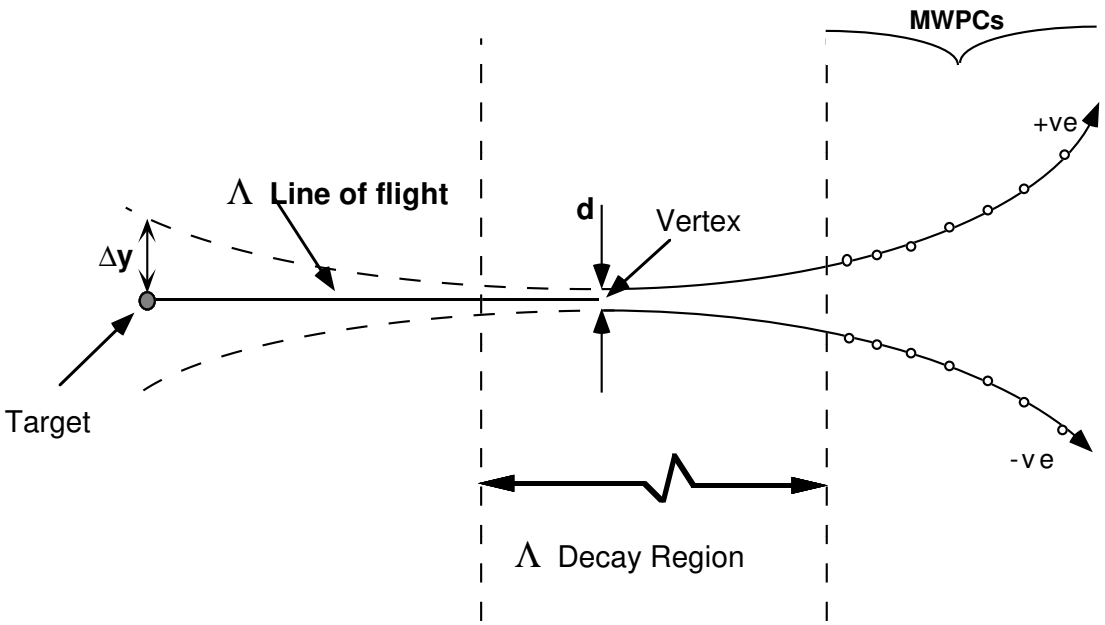

Figure 3.2: Schematic representation of a possible Λ decay.

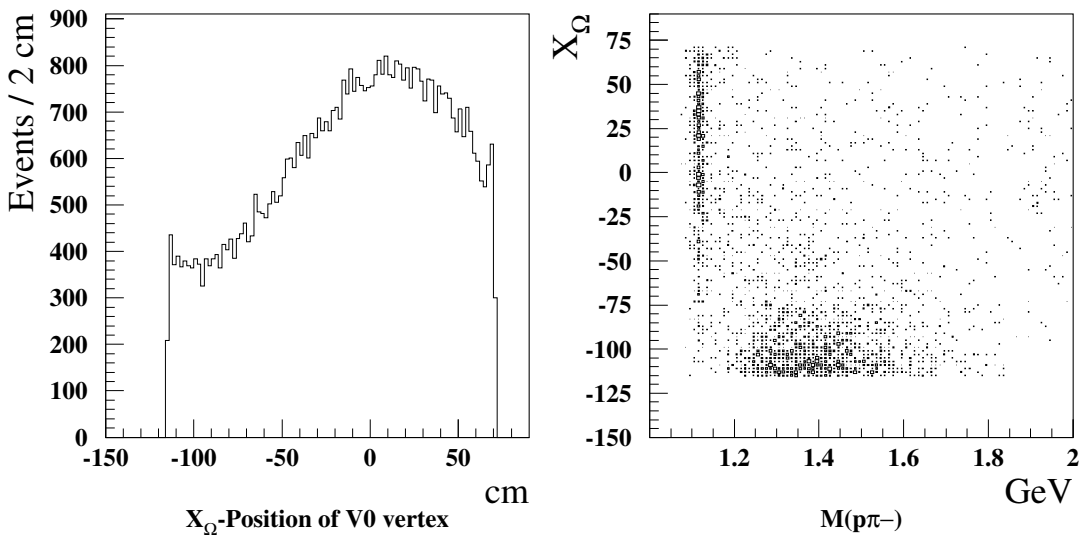

Figure 3.3: Distribution of the V^0's vertex.

will now only be accepted if this angle is less than 0.75^0.

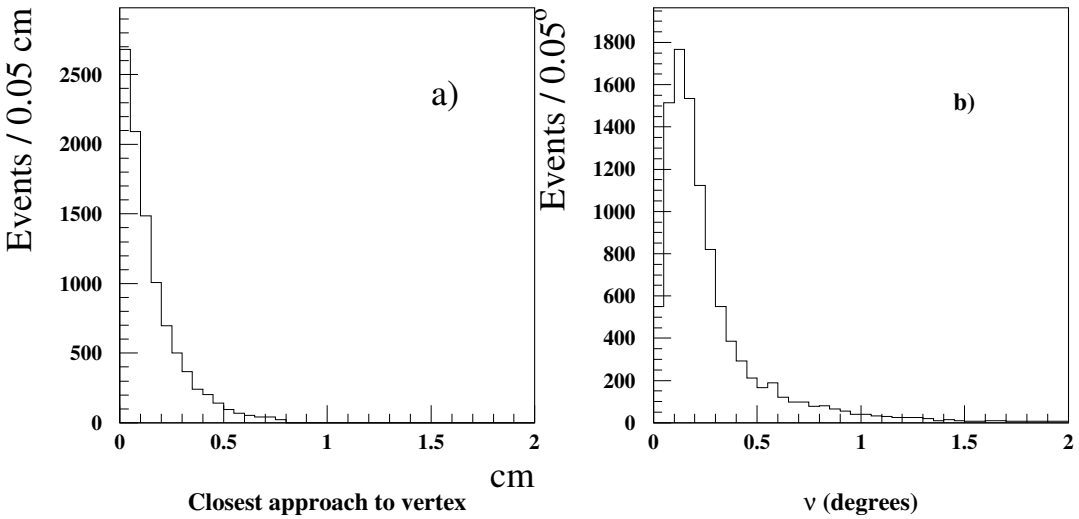

Figure 3.4: Distribution of a) the closest approach between positive and negative tracks and b) the angle, ϑ, between the sum of the three momenta of the V^0 decay tracks and the line of flight from the centre of the target, for Λ candidates that have had all other cuts applied.

The quality of the V^0 candidates that have passed the above cuts can be assessed by studying their distribution on the Podolanski-Armenteros plot [32]. The three-momenta of the V^0 decay particles are resolved into a transverse component, q_T, and the components q_L^+, q_L^- parallel to the direction of motion of the V^0, for positive and negative tracks respectively. The variable α describes the asymmetry of a decay and is defined by,

$$\alpha = \frac{q_L^+ - q_L^-}{q_L^+ + q_L^-}.$$

In the scatter plot of q_T versus α the kinematically allowed regions for V^0s are ellipses as shown in figure 3.5 (dotted line) and explained in appendix B. The ellipse for K^0s overlaps the ellipses for Λs and $\overline{\Lambda}$s. It can be seen however that in certain kinematic regions the V^0s are unambiguous.

In figure 3.5 the data shows a clear correlation between q_T and α for Λs, $\overline{\Lambda}$s and K^0s. The background in the region of the ellipses is low, the noise at the top of the

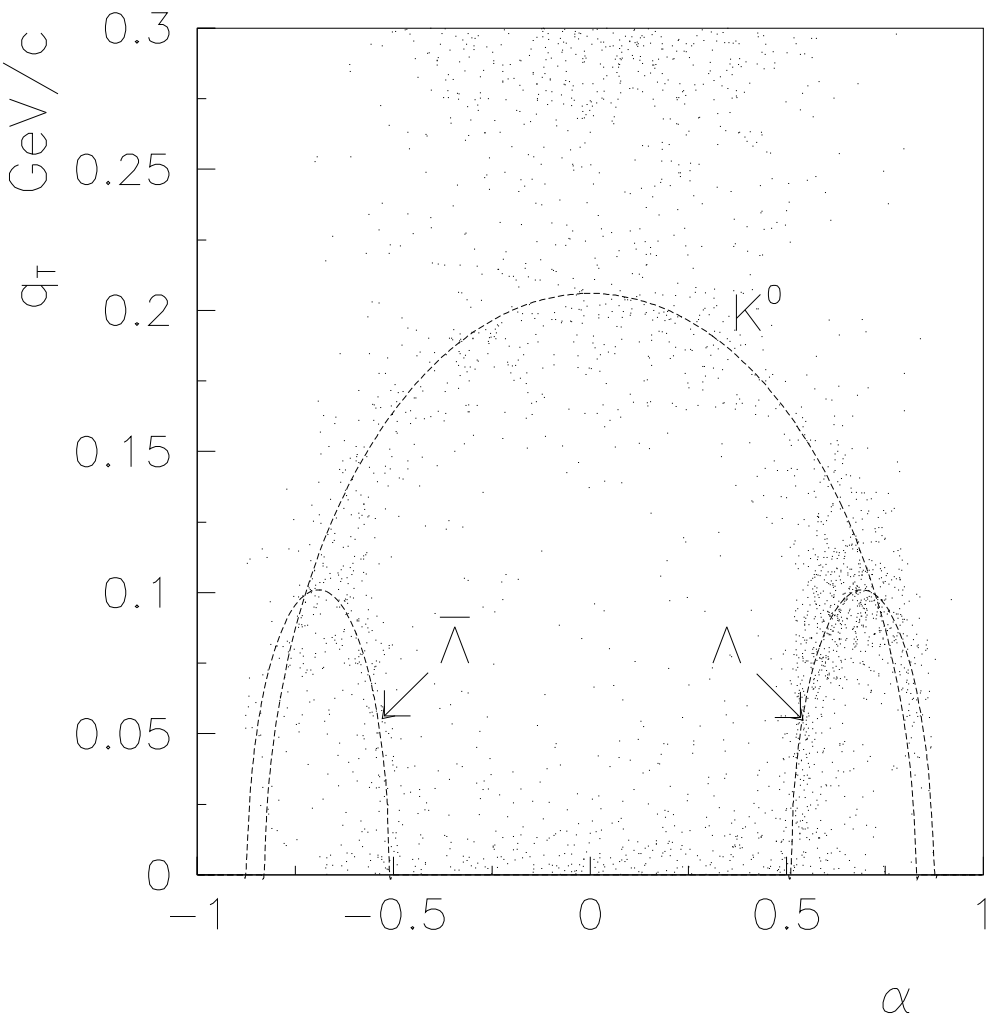

Figure 3.5: Podolanski-Armenteros plot for V^0 candidates.

figure being due to tracks from the target crossing and thus producing fake V^0s.

Λs, $\overline{\Lambda}$s and K^0s are then selected in the following α range,

- $\overline{\Lambda}$s $\cdots \alpha < -0.45$,
- Λs $\cdots \alpha > 0.45$,
- K^0s $\cdots -0.45 < \alpha < 0.45$.

3.3 Impact parameter cuts

As mentioned earlier most of the V^0 background comes from tracks which originate from the target intersecting and thus looking like a V^0 decay. The paths of real V^0 decay tracks will, in general, cross each other twice, once at the vertex and then again some distance from the vertex (either upstream or downstream). It turns out that the maximum distance between these crossing points does not depend on the V^0 momentum but only on the decay particles momentum in the centre of mass frame, p^*, and the magnetic field strength. Therefore, for a given type of V^0 in a given magnetic field the maximum distance between the crossing points of the decay tracks is a constant.

Figure 3.6 shows the paths of the decay tracks crossing at the vertex which may be at A or B. The distance between the crossing points is given by L where L is defined by,

$$\sin\theta = \frac{L}{2R} \tag{3.1}$$

R is the radius of curvature of the particle in a magnetic field, B, and the projection of this in the x_Ω direction is $x = Lsin\phi$.

The interaction between a charged particle and the magnetic field it is traversing is given by

$$e(\underline{v} \times \underline{B}) = \frac{mv^2}{R} \Rightarrow R = \frac{p}{e \mid B \mid \sin\phi} \tag{3.2}$$

where p is the momentum of the track and ϕ is the angle between the magnetic field and the motion of the particle. Now for small θ

$$\sin\theta \simeq tan\theta = \frac{q_T}{q_L} \tag{3.3}$$

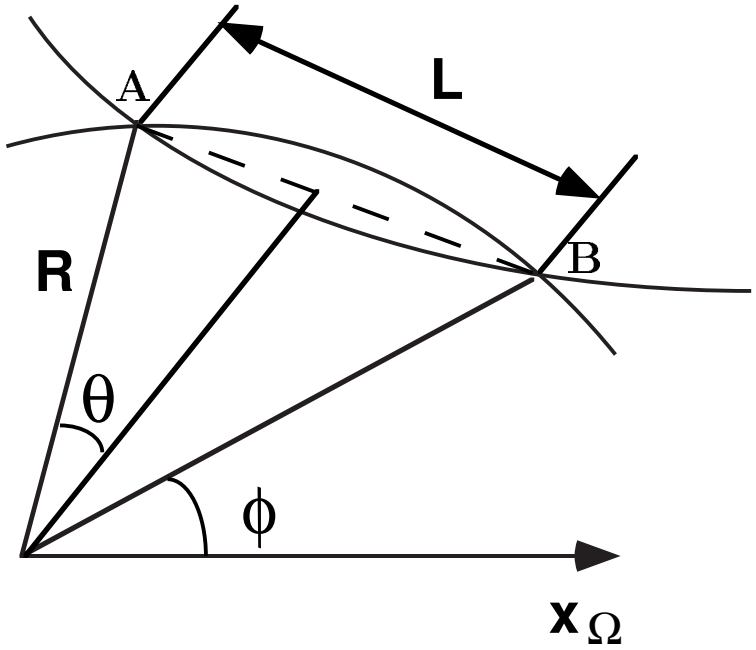

Figure 3.6: Crossing paths of two V^0 decay tracks.

Thus $\sin\theta$, hence L, will be at their maximum when q_T is at its maximum and since $q_T = p^* \cos\theta^*$, $q_{Tmax} = p^*$. For $\Lambda \rightarrow p\pi^-$, $p^* = 0.1$ GeV/c and as the decay tracks have momenta, p, of several GeV/c, $p \gg p^* \Rightarrow q_L \simeq p$. Therefore from equation 3.3 we have

$$\sin\theta_{max} \simeq \frac{p^*}{p} \tag{3.4}$$

Therefore using equations 3.1,3.2 and 3.4 we find that the maximum crossing distance, L_{max}, is given by,

$$L_{max} \simeq 2(\frac{p}{Besin\phi}) \times (\frac{p^*}{p}) = \frac{2p^*}{Besin\phi} \tag{3.5}$$

and in metres

$$L_{max} \simeq \frac{2p^*(GeV/c)}{B(T)esin\phi} \times \frac{10^9 e}{c} = \frac{2p^*(GeV/c)}{0.29979B(T)sin\phi} \tag{3.6}$$

and as $x = Lsin\phi$ and B = 1.8 Tesla for WA94,

- $x_{\Omega max} \simeq 40$ cm for Λs,

- $x_{\Omega max} \simeq 80$ cm for K^0s, as for $K^0 \rightarrow \pi^-\pi^+$, $p^* = 0.2$ GeV/c.

This means that as we only accept Λ ($\overline{\Lambda}$) candidates if they decay at least 135 cm from the target the two decay tracks cannot trace back to the target. The impact parameter Δ_y is defined as the distance of a track from the centre of the target, in the bend direction of the magnetic field, at the target plane, as seen in figure 3.2. Figure 3.7 shows the distribution of the Δ_y for a) protons and b) pions from the decays of Λ candidates. It also shows the Δ_y against the effective mass, M($p\pi^-$), of the V^0 candidates for c) protons and d) pions from the decays of Λ candidates. The background due to tracks from the target is hence removed by demanding that tracks traced to the target plane have a non-zero impact parameter. Hence we require

- $\Delta_y(\pi) > 4$ cm,
- $\Delta_y(p) > 2$ cm.

We then select Λ and $\overline{\Lambda}$ candidates in a 50 MeV mass interval centred on the Λ mass taken from [33], i.e. $1.09 < M_\Lambda < 1.14$ MeV.

3.4 Summary of cuts used to identify Λs and $\overline{\Lambda}$s

(i) Each decay track has at least four space points,

(ii) each track traces through all seven MWPCs,

(iii) the V^0 vertex lies in the range $-80 < x_\Omega < 71$ cm,

(iv) the positive and negative tracks of the V^0 must have a distance of closest approach of less than 1 cm,

(v) the angle between the V^0s line of flight from the target and the sum of the three-momenta for the V^0 decay tracks is $< 0.75^o$, i.e. the candidate comes from the target,

(vi) $\overline{\Lambda}$s $\cdots \alpha < -0.45$; Λs $\cdots \alpha > 0.45$,

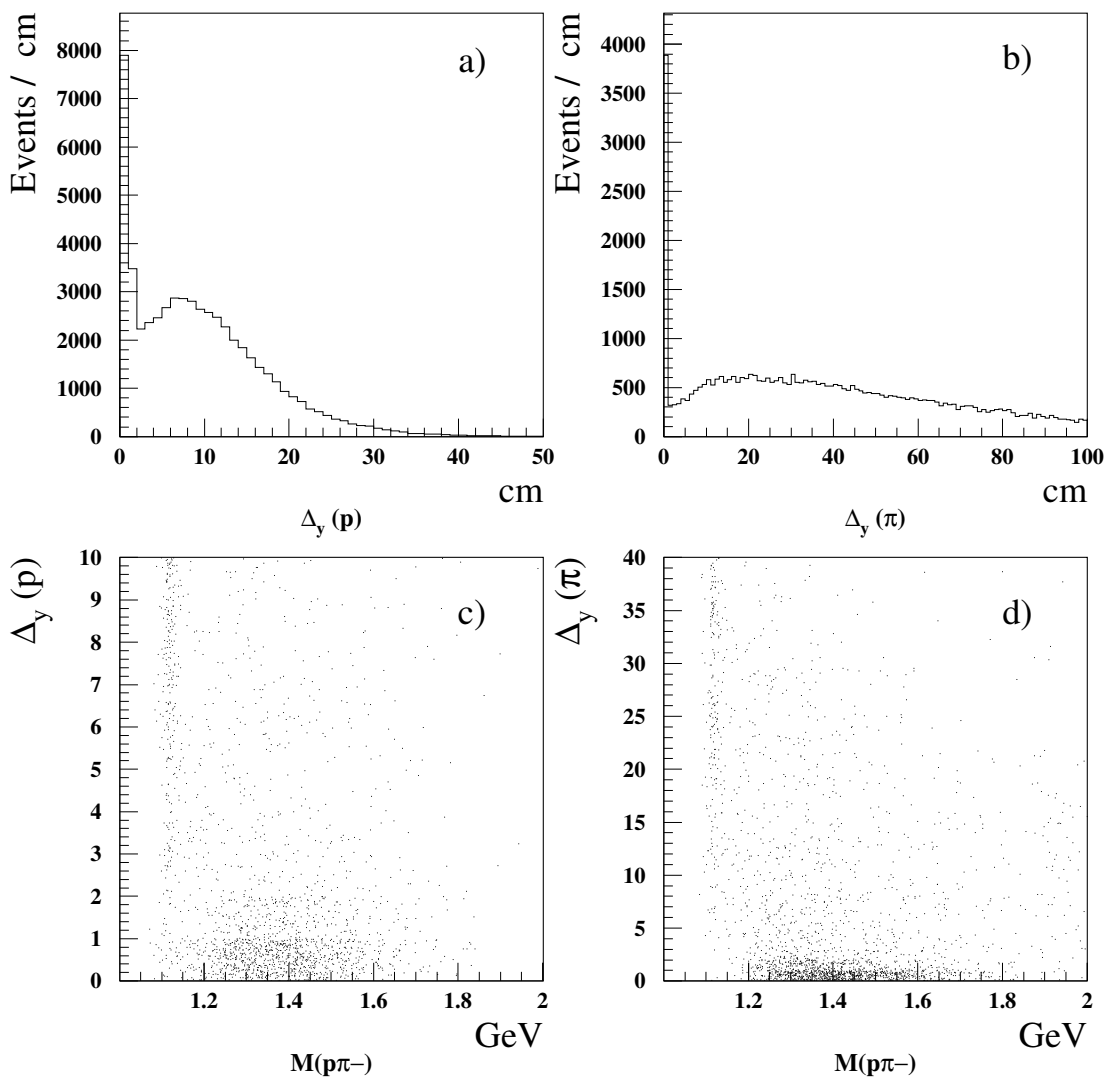

Figure 3.7: Distribution of the impact parameters.

(vii) $\Delta_y > 2$ cm for $p(\overline{p})$ and $\Delta_y > 4$ cm for $\pi^-(\pi^+)$, from the $\Lambda(\overline{\Lambda})$ decay,

(viii) the effective mass is in the range,

$$(M_\Lambda - 25MeV) < M(p\pi^-) < (M_\Lambda + 25MeV).$$

Figure 3.8 shows the effective mass plots of a sample of Λ candidates after a) having passed through STRIPV0 and then having the cuts b) i and ii, c) i to iv and d) i to vii performed on them. As can be seen from figure 3.8d a clear peak at the Λ mass can be seen with little background after cuts i to vii have been applied to the V^0 candidates.

3.5 K^0 Contamination

The V^0s in the kinematic region $\mid \alpha \mid > 0.45$ are ambiguous, i.e. this region contains K^0s as well as Λs. This K^0 contamination can however be estimated as follows,

$$n_{\Lambda\prime} = n_\Lambda + n_K,$$

$$n_{\overline{\Lambda}\prime} = n_{\overline{\Lambda}} + n_K,$$

where $n_{\Lambda\prime}$ ($n_{\overline{\Lambda}\prime}$) equals the number of Λ ($\overline{\Lambda}$) candidates and $n_\Lambda(n_{\overline{\Lambda}})$ equals the actual number of Λs ($\overline{\Lambda}$s); n_K is the number of contaminating K^0s, which due to the symmetry in the Podolanski- Armenteros plot is the same for $\alpha < 0.45$ and $\alpha > 0.45$. Now by selecting Λs and $\overline{\Lambda}$s in the unambiguous regions ($0.45 <\mid \alpha \mid < 0.60$), i.e where $n_{\Lambda\prime} = n_\Lambda$, we can find the ratio $n_{\overline{\Lambda}}/n_\Lambda$. Then we now know $n_{\Lambda\prime}$, $n_{\overline{\Lambda}\prime}$ and $n_{\overline{\Lambda}}/n_\Lambda$ and so we can find n_Λ, $n_{\overline{\Lambda}}$ and n_K. In fact we find that the K^0 contamination to be around 1% for Λs and about 3% for $\overline{\Lambda}$s.

3.6 Results on Λ and $\overline{\Lambda}$ production

Figure 3.9 shows the mass plots for a) Λs (M($p\pi^-$)) and b) $\overline{\Lambda}$ (M($\overline{p}\pi^+$)) after all the cuts have been applied, apart from the Λ mass cut. We then select candidates in the 50 MeV interval centred on the Λ mass, giving 56140 Λ and 18014 $\overline{\Lambda}$ candidates. These candidates contain some K^0 contamination; in the unambiguous region

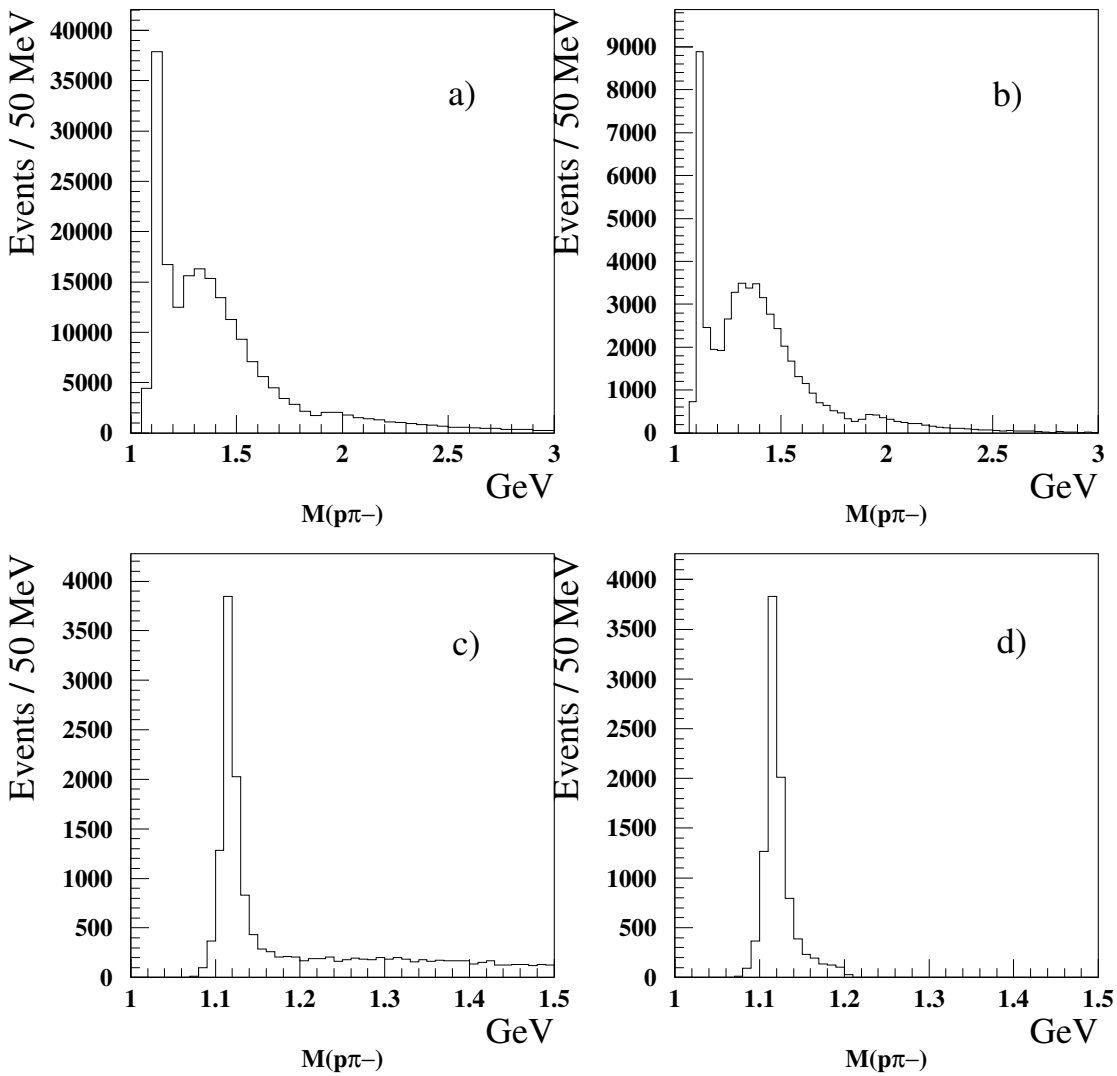

Figure 3.8: Effective mass plots of Λ candidates after a) having passed through STRIPV0 and then having the cuts b) i and ii, c) i to iv and d) i to vii performed on them.

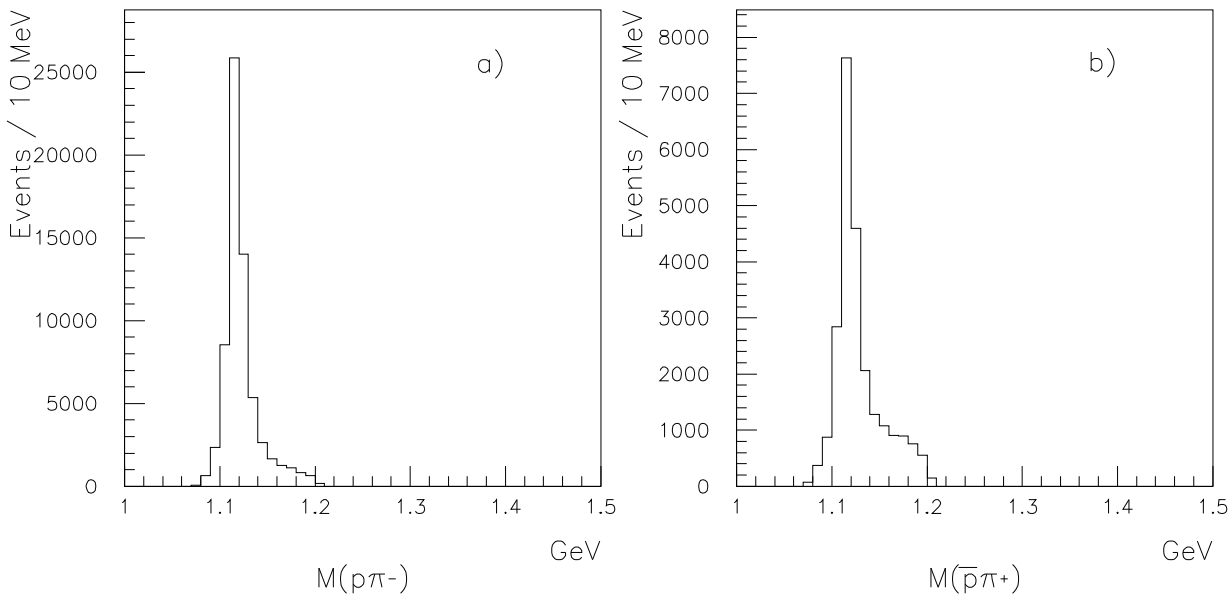

Figure 3.9: Effective mass distributions for V^0 candidates as (a) $p\pi^-$ and (b) $\overline{p}\pi^+$.

($0.45 < |\alpha| < 0.60$) we find 28787 Λ and 8783 $\overline{\Lambda}$ candidates, giving an uncorrected ratio of $\overline{\Lambda}$ to Λ of 0.305 ± 0.004.

3.7 Identifying Ξs and $\overline{\Xi}$s

We identify Ξs by the weak decays

$$\Xi^- \rightarrow \Lambda + \pi^-$$

$$\overline{\Xi^-} \rightarrow \overline{\Lambda} + \pi^+$$

with the Λ ($\overline{\Lambda}$) decaying to $p\pi^-$ ($\overline{p}\pi^+$). The signature for a cascade is therefore a charged track that intercepts the path of a lambda. A schematic diagram of a Ξ^- decay is shown in figure 3.10. This signature is found by a program called WA94XI which goes through the data on the STRIPV0 DST looking for the intersection of the line of flight of a Λ ($\overline{\Lambda}$) candidate with a negatively (positively) charged track at a point well separated from the target region.

WA94XI requires that the Armenteros α lies in the range $\mid \alpha \mid > 0.40$, this rejects many V^0s without rejecting any Λs or $\overline{\Lambda}$s. It also tightens the cut on the x-coordinate

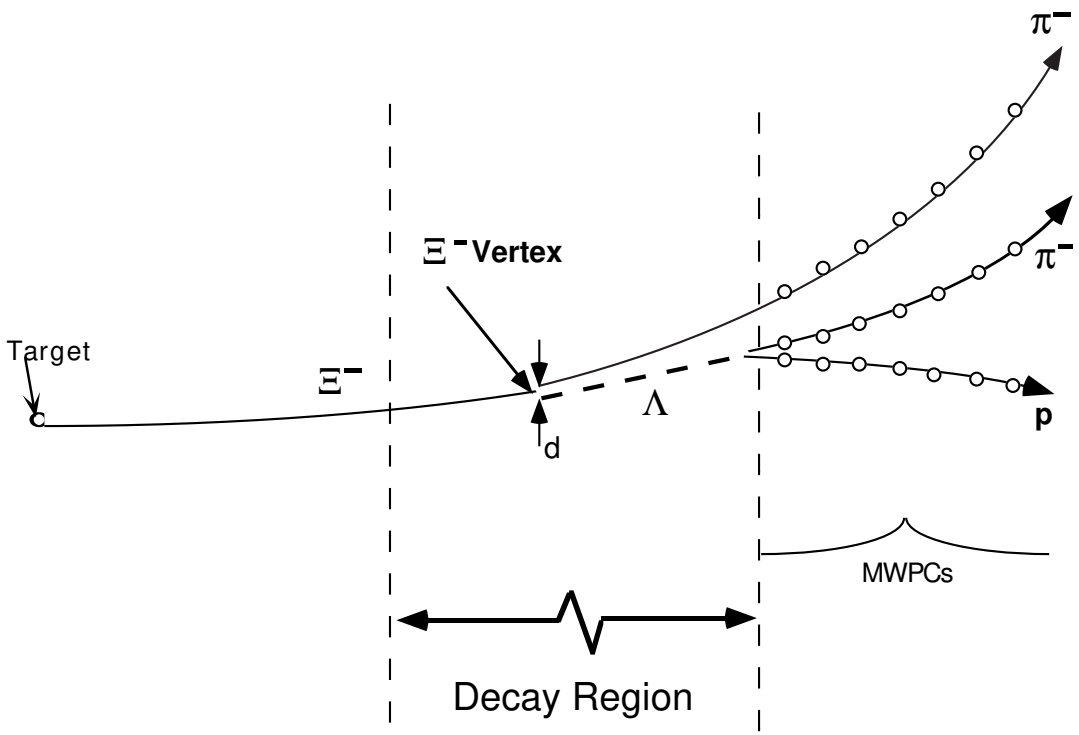

Figure 3.10: Schematic representation of a possible Ξ^- decay.

of the V^0 vertex to be in the range $-105 < x_\Omega < 71$ cm. A mass cut is then performed on the V^0s of $(M_\Lambda - 40MeV) < M(p\pi) < (M_\Lambda + 40)$ MeV. The distance of closest approach between the line of flight of the Λ ($\overline{\Lambda}$) and a negative (positive) track must be less than 3 cm or the cascade candidate is rejected. The vertex of the remaining cascade candidates are chosen to be the midpoint of the line joining the V^0 candidate and the charged track at their points of closest approach. The x-coordinate of the cascade vertex is then required to lie in the range $-150 < x_\Omega < 71$ cm. WA94XI then writes out a cascade DST.

The effective mass, M($\Lambda\pi^-$), after the above cuts have been made on the STRIPV0 DST by WA94XI is shown in figure 3.11. Even with the loose cuts applied by WA94XI a peak at the Ξ mass can be seen.

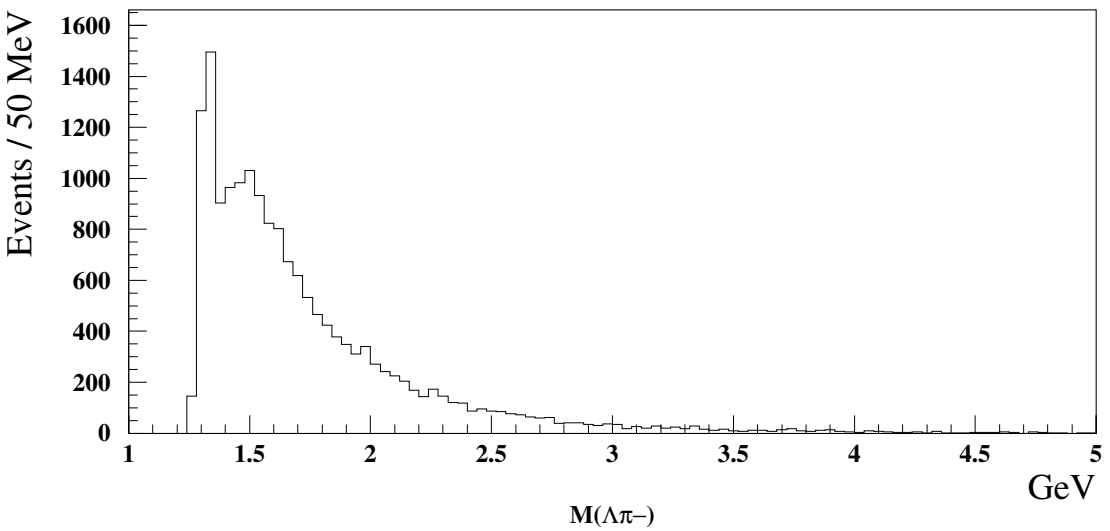

Figure 3.11: M($\Lambda\pi^-$).

3.8 Further cuts performed on the Ξ candidates

To identify the tracks better and to standardise the acceptance of the apparatus we require that the decay tracks from the V^0 candidate and the charged decay track intercepting with the V^0 line of flight have at least four space points and trace

through the first four MWPCs.

The cuts applied to the V^0 candidates by STRIPV0 and then by WA94XI are quite loose cuts. Further cuts are made on the V^0s coming from the cascade candidates, i.e. that the x-coordinate of the V^0 vertex is greater than -80 cm, the distance of closest approach of the two V^0 decay tracks is less than 1.6 cm, and the q_T of the V^0 decay tracks are less than 0.12 GeV/c (the maximum value of q_T is p^* which for the decay $\Lambda \rightarrow p\pi^-$ is 0.10 GeV/c).

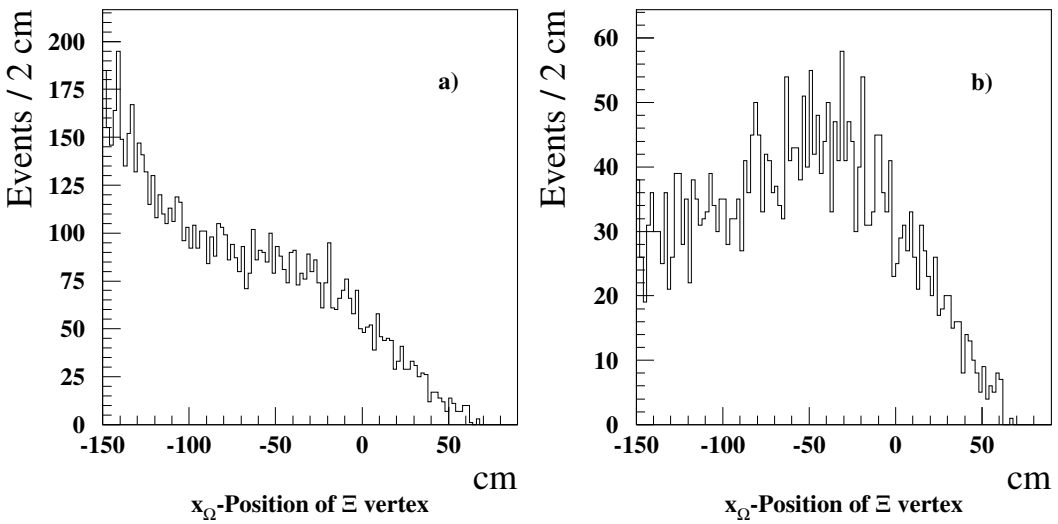

Figure 3.12: Distribution of the vertices of Ξ candidates.

Figure 3.12 shows the distribution of the x-coordinate of a) raw Xi candidates from WA94XI and b) the same parameter after all other cuts have been applied. The acceptance of the apparatus is low for cascades which decay a long way from the MWPCs. We therefore require that the x-position of the Ξ vertex is in the range $-125 < x_\Omega < 71$ cm which reduces the background without losing many Ξs.

Figure 3.13 shows a) the distribution of the variable closxi, which is half the distance of closest approach between the V^0 candidate and the charged track from the cascade candidate and b) closxi against M($\Lambda\pi$). The cut on this distance is tightened so that cascade candidates with closxi greater than 0.8 cm are rejected.

The V^0 vertex must, of course, be after the cascade vertex i.e. the intersection

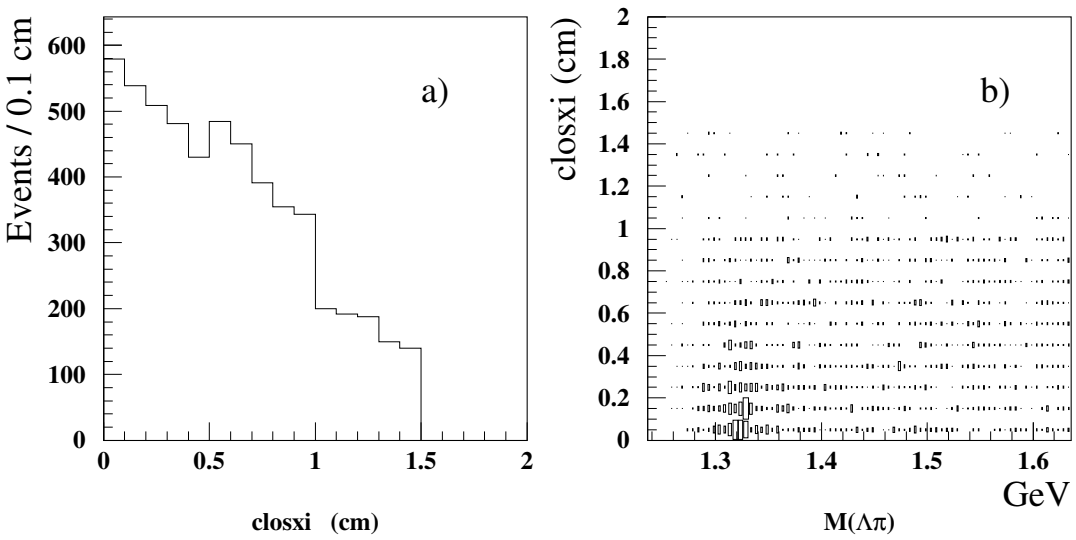

Figure 3.13: Distribution of closxi.

of the charged track with the path of the V^0 candidate must be before the V^0 vertex. Therefore cascade candidates with $x_{V^0} - x_\Xi < 0$ cm are rejected. Because of the errors in finding the vertex positions this cut might lose a few real cascades, however this can be corrected for in efficiency calculations. The effective mass of Ξ candidates, M($\Lambda\pi^-$), after all the above tighter cuts have been applied is shown in figure 3.14. Although the background has been reduced by applying the above cuts it is still appreciable; however some further cuts can still be made.

3.8.1 Impact Parameter cuts

Figure 3.15 shows a) the distribution of the impact parameter of the π^- from the decay of a cascade candidate, *bypi* (see figure 3.10), and b) *bypi* plotted against the effective mass M($\Lambda\pi^-$) of the cascade candidate. A cut of $|$ *bypi* $|> 6$ cm is made on the cascade sample which removes some of the background (seen in figure 3.5), caused by charged tracks from the target crossing the paths of V^0 candidates.

If the cascade candidate is a real cascade coming from the target it should trace back to the target. Hence the cascade candidates are traced back to the target plane and the distance from this point to the target, *byxi* (see figure 3.10), is plotted in

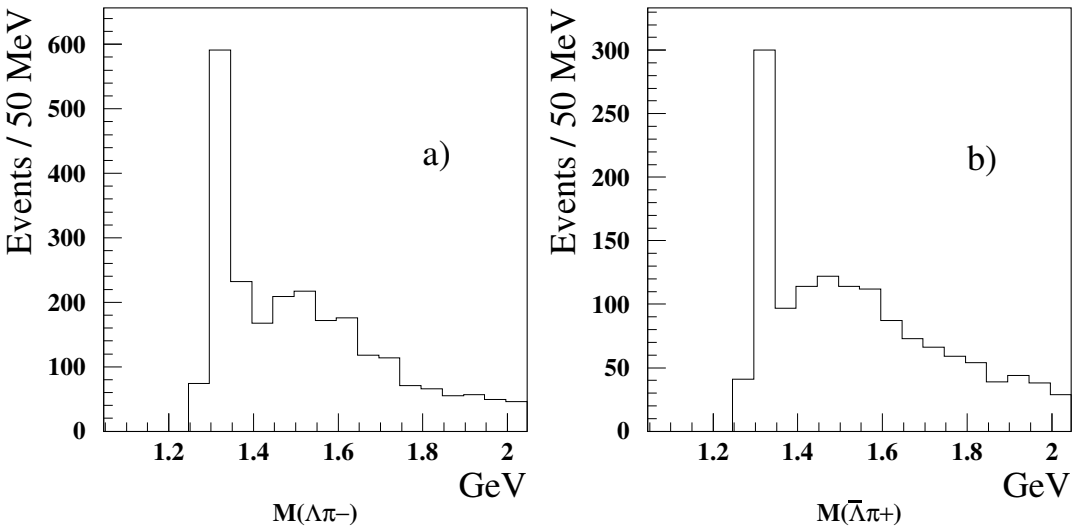

Figure 3.14: Effective mass distribution of a) M($\Lambda\pi^-$) and b) M($\overline{\Lambda}\pi^+$).

figure 3.16a, figure 3.16b shows the impact parameter, $byxi$, plotted against M($\Lambda\pi^-$). As can be seen Ξ candidates have an impact parameter centred on y = 0 cm and a cut of $\mid byxi \mid < 2.0$ cm is applied.

We then select Ξ and $\overline{\Xi}$ candidates in a 100 MeV mass interval centred on the Ξ mass taken from [33], i.e. $1.271 < M_{\Xi} < 1.371$ MeV.

3.9 Summary of cuts used to identify Ξs and $\overline{\Xi}$s

Cuts used on the V^0 candidates are,

(i) each decay track has at least four space points,

(ii) each track traces through the first four MWPCs,

(iii) the V^0 vertex lies in the range $-80 < x < 71$ cm,

(iv) the positive and negative tracks of the V^0 must have a distance of closest approach of less than 1.6 cm,

(v) $\mid \alpha \mid > 0.40$,

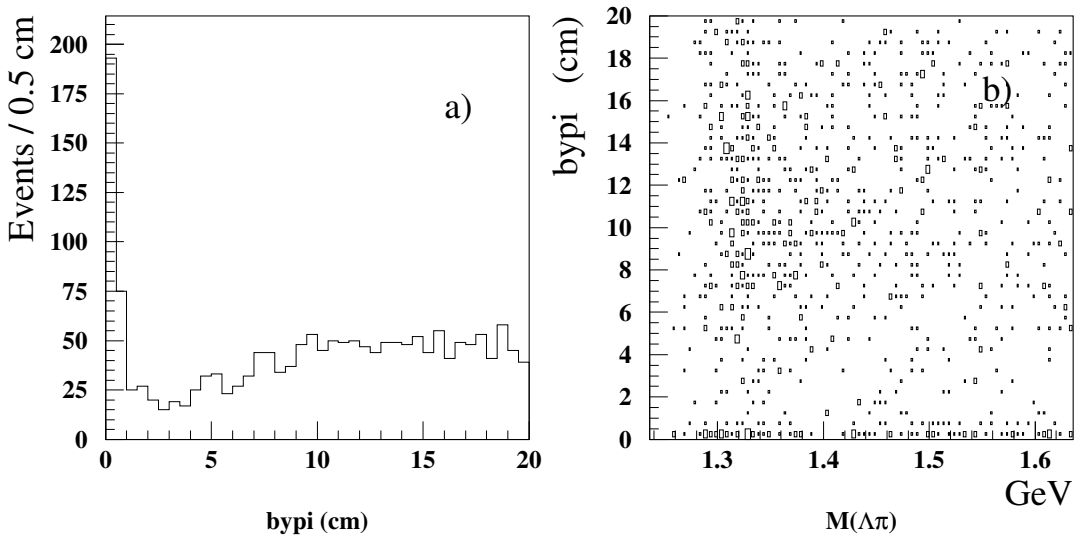

Figure 3.15: Distribution of the impact parameter of the pion, *bypi*, and *bypi* plotted against M($\Lambda\pi^-$).

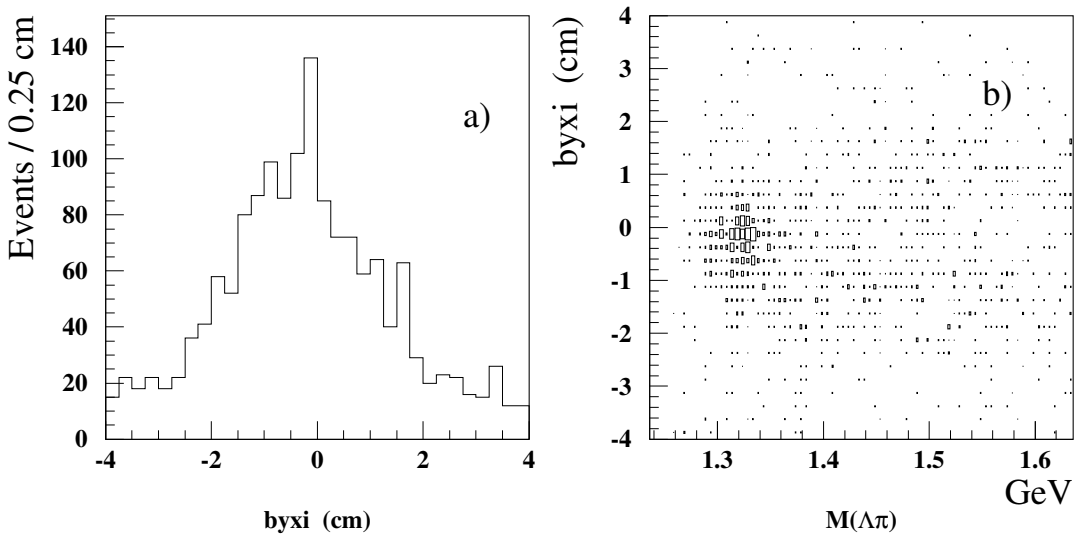

Figure 3.16: Distribution of the impact parameter of the cascade, *byxi*, and *byxi* plotted against M($\Lambda\pi^-$).

(vi) $q_T < 0.12$,

(vii) the effective mass is in the range,
$(M_\Lambda - 40MeV) < M(p\pi^-) < (M_\Lambda + 40MeV)$.

The cuts performed on the cascade candidates are,

(i) the charged decay track has at least four space points,

(ii) the charged decay track traces through the first four MWPCs,

(iii) the Ξ vertex lies in the range $-80 < x < 71$ cm,

(iv) the distance of closest approach between the V^0 and the charged track is less than 1.6 cm,

(v) the Ξ vertex is before the V^0 vertex,

(vi) $\mid bypi \mid > 6.0$ cm,

(vii) $\mid byxi \mid < 2.0$ cm,

(viii) the effective mass is in the range,
$(M_\Xi - 50MeV) < M(\Lambda\pi^-) < (M_\Xi + 50MeV)$.

Figure 3.17 shows the effective mass plots of a) M($\Lambda\pi^-$) and b) M($\overline{\Lambda}\pi^+$) after all the cuts have been applied apart from the Ξ mass cut. With this mass cut we find 547 Ξ^-s and 278 $\overline{\Xi^-}$s giving an uncorrected ratio of $\overline{\Xi^-}$ to Ξ^- of 0.51 ± 0.04.

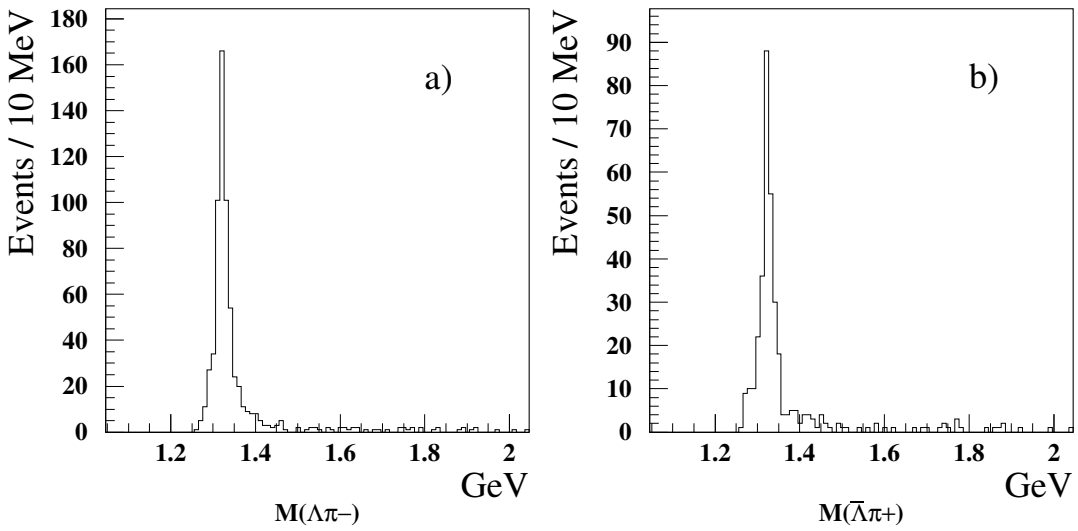

Figure 3.17: Effective mass distribution of a) M($\Lambda\pi^-$) and b) M($\overline{\Lambda}\pi^+$).

3.10 Summary

Both Λs and Ξ^-s have been reconstructed to give clean mass peaks with little background in the difficult environment of heavy ion interactions. The raw yields for these particles are shown in the table below, where the numbers in brackets are the yields of unambiguous Λs.

Table 3.1: Raw yields obtained from the WA94 1991 sulphur sulphur data.

Particle	Raw particle yields
Λ	56140 (28783)
$\overline{\Lambda}$	18014 (8783)
Ξ^-	547
$\overline{\Xi^-}$	278

These yields give the following ratios

$$\frac{\overline{\Lambda}}{\Lambda} = 0.305 \pm 0.004,$$

$$\frac{\overline{\Xi^-}}{\Xi^-} = 0.51 \pm 0.04.$$

These ratios need to be corrected to take account of the geometrical acceptance and reconstruction efficiency of the apparatus for the different particle species. Furthermore the $\overline{\Lambda}$ to Λ ratio has to be corrected for cascade "feed-down" where the Λs and $\overline{\Lambda}$s come from Ξ decays. These corrections are discussed later and enable the calculation of the relative production rates of the different particle species detected by WA94 in the 1991 sulphur-sulphur run.

Chapter 4

Identifying K^- and K^+ meson decays

The study of strange mesons, as well as hyperons, is of interest to those using strange particle production to probe into the physics of heavy ion interactions. Charged kaons decay via the weak decays

$$K^- \rightarrow \pi^- + \pi^+ + \pi^-$$

$$K^+ \rightarrow \pi^- + \pi^+ + \pi^+.$$

The topology of $K \rightarrow \pi\pi\pi$ is similar to the topology of a Xi decay ($\Xi \rightarrow \Lambda\pi \rightarrow p\pi\pi$). Therefore the cascade finding program WA94XI has been adapted to look for K decays instead of Ξ decays. The signature for a $K^{\pm}$ is a $\pi^{\pm}$ coming from the vertex of an apparent $V^0 \rightarrow \pi^-\pi^+$. Two cuts are applied to suppress other particles which are of the V^0 type, these are:

- we require the mass of the 2π object, $M_{\pi\pi}$, to be less than 0.42 GeV,
- we also require $|\alpha_{V0}| < 0.45$.

As mentioned in chapter 3, in creating the STRIPV0 data summary tapes a few cuts are made to reduce the background with respect to the reconstruction of Λ hyperons. One of these cuts is a momentum cut of 6.5 GeV/c, as can be seen from

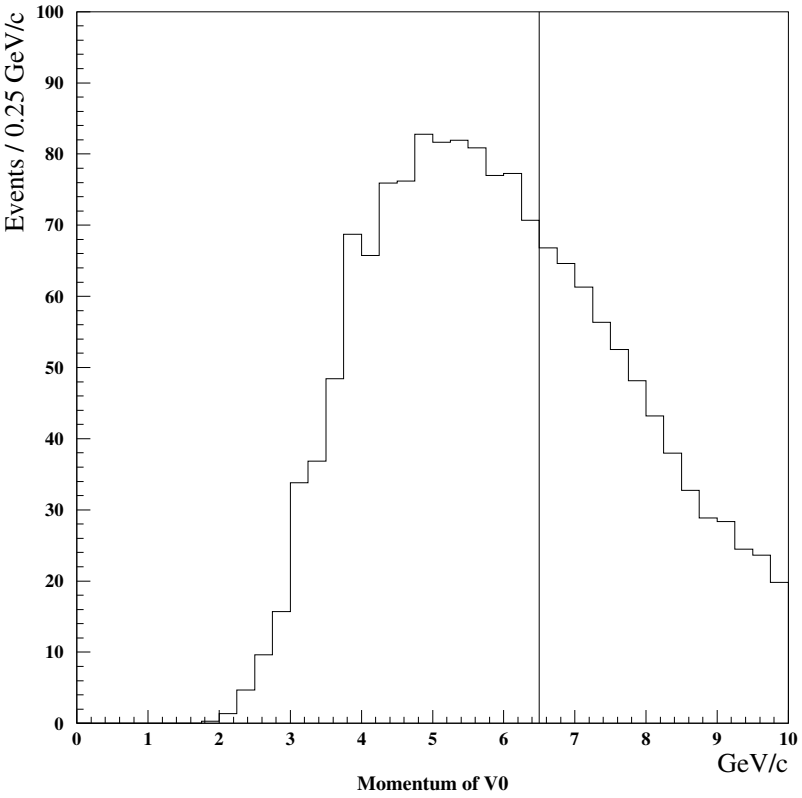

Figure 4.1: Momentum distribution of V^0s coming from Monte Carlo K decays.

figure 4.1 which shows the distribution of the momenta of V^0s coming from the decays of Ks generated using a Monte Carlo program, at least half of the Ks will decay to V^0s having a momentum of less than 6.5 GeV/c. Therefore in the long term the tapes will have to be re-done without this cut on the V^0 momentum; in this thesis results will be presented using only the sample having this cut applied.

As for the Ξ case the three decay particles are required to trace through the first four MWPCs and to have at least 4 space points each. The effective mass, M($\pi\pi\pi$), after these conditions is shown in figure 4.2. Even with these initial cuts applied by STRIPTAU, the modified version of WA94XI, a peak at the $K^{\pm}$ mass can be seen.

4.1 Further cuts performed on the $K^{\pm}$ candidates.

Although a peak at the K mass can clearly be seen in figure 4.2 there is still a large amount of background present, so a study of further cuts to apply to these candidates has been undertaken. Figure 4.3 shows the distribution of the x_{Ω} position of the K

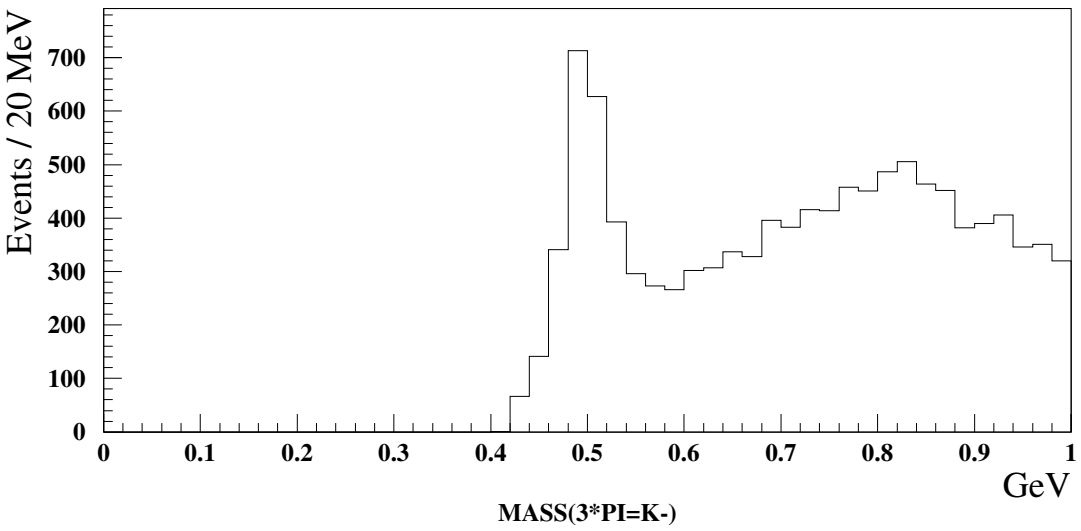

Figure 4.2: Effective mass distribution, M($\pi\pi\pi$), after initial cuts are applied.

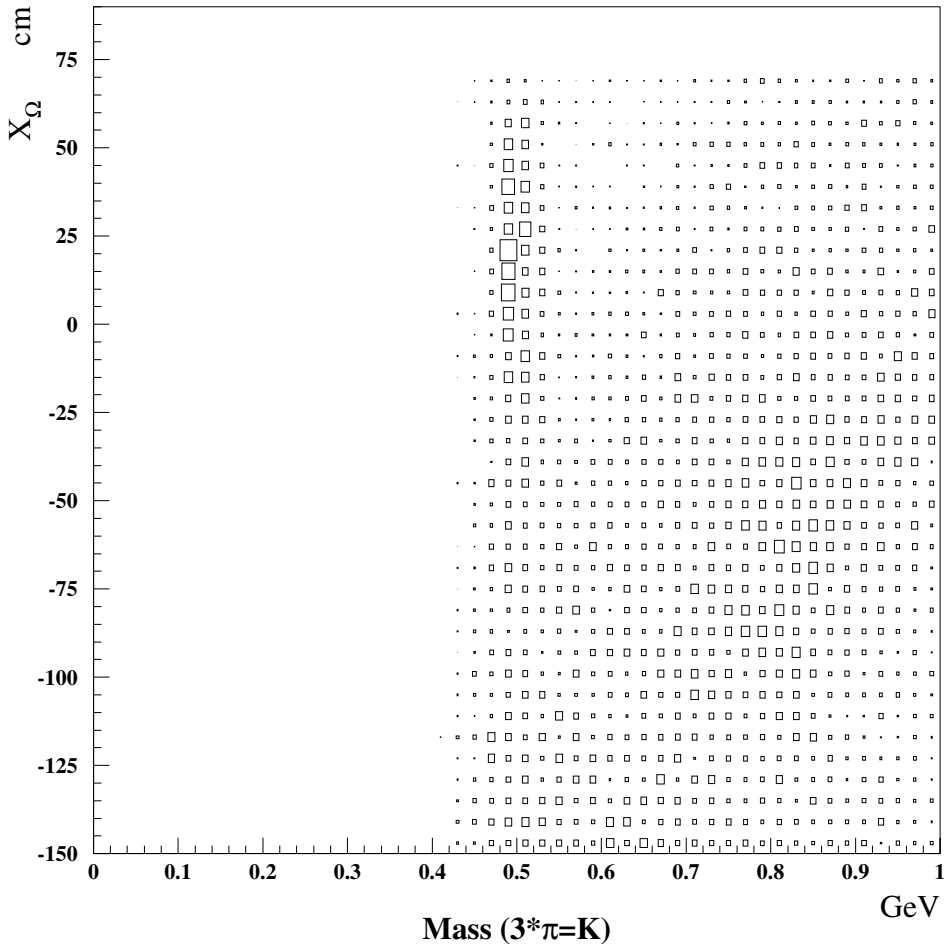

Figure 4.3: x_Ω coordinate of candidates vertices against M($\pi\pi\pi$).

vertex against the against the effective mass, M($\pi\pi\pi$), of these candidates. A signal in the K mass region is most clearly seen when the position of the vertex is larger than -55 cm. Therefore the vertex is required to lie in the region $-55 < x_\Omega < 71$ cm.

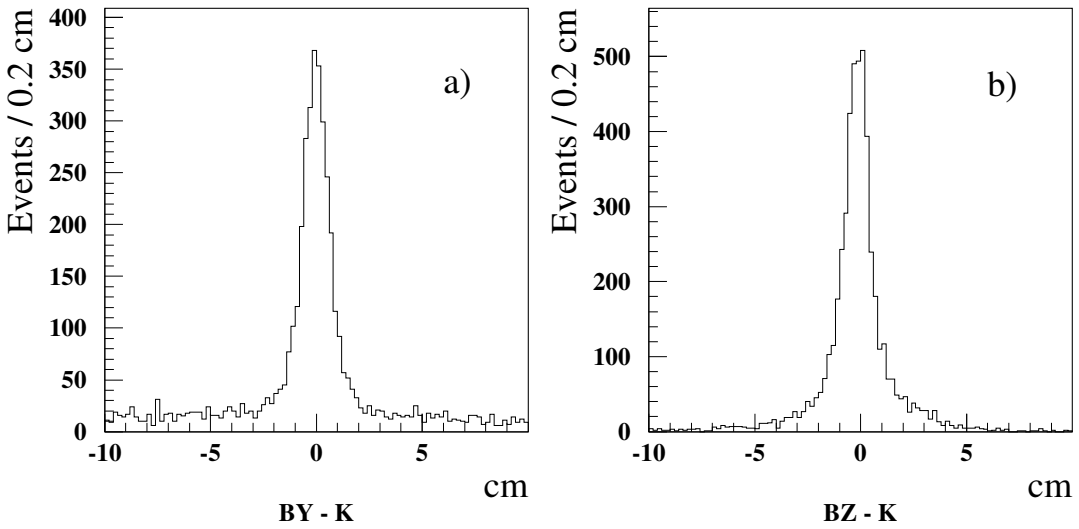

Figure 4.4: Impact parameters of the reconstructed $K^{\pm}$s at the target.

The reconstructed $K^{\pm}$ should trace back to the target, figure 4.4 shows the distribution of the impact parameter of the reconstructed $K^{\pm}$ at the target plane a) in the y direction, byk, and b) the z direction, bzk. The $K^{\pm}$ is then required to satisfy the conditions:

- $\mid byk \mid < 2.0$ cm,
- $\mid bzk \mid < 2.0$ cm.

Whilst the $K^{\pm}$ should come from the target the decay tracks should not, figure 4.5 shows the distribution of the impact parameters of the three decay tracks at the target against the effective mass distribution M($\pi\pi\pi$). The noise caused by tracks coming from the target can clearly be seen in these plots. We require that the decay tracks miss the target by at least 5 cm, i.e. $\mid by(\pi) \mid \geq 5$ cm for each pion.

Unlike the Ξ case the third pion should trace back to the Ks vertex. Figure 4.6 is an example of how tracks recorded in the A chambers and traced back towards the target could be due to a $K^{\pm}$ decay. The bend plane projections of the V^0 (decaying

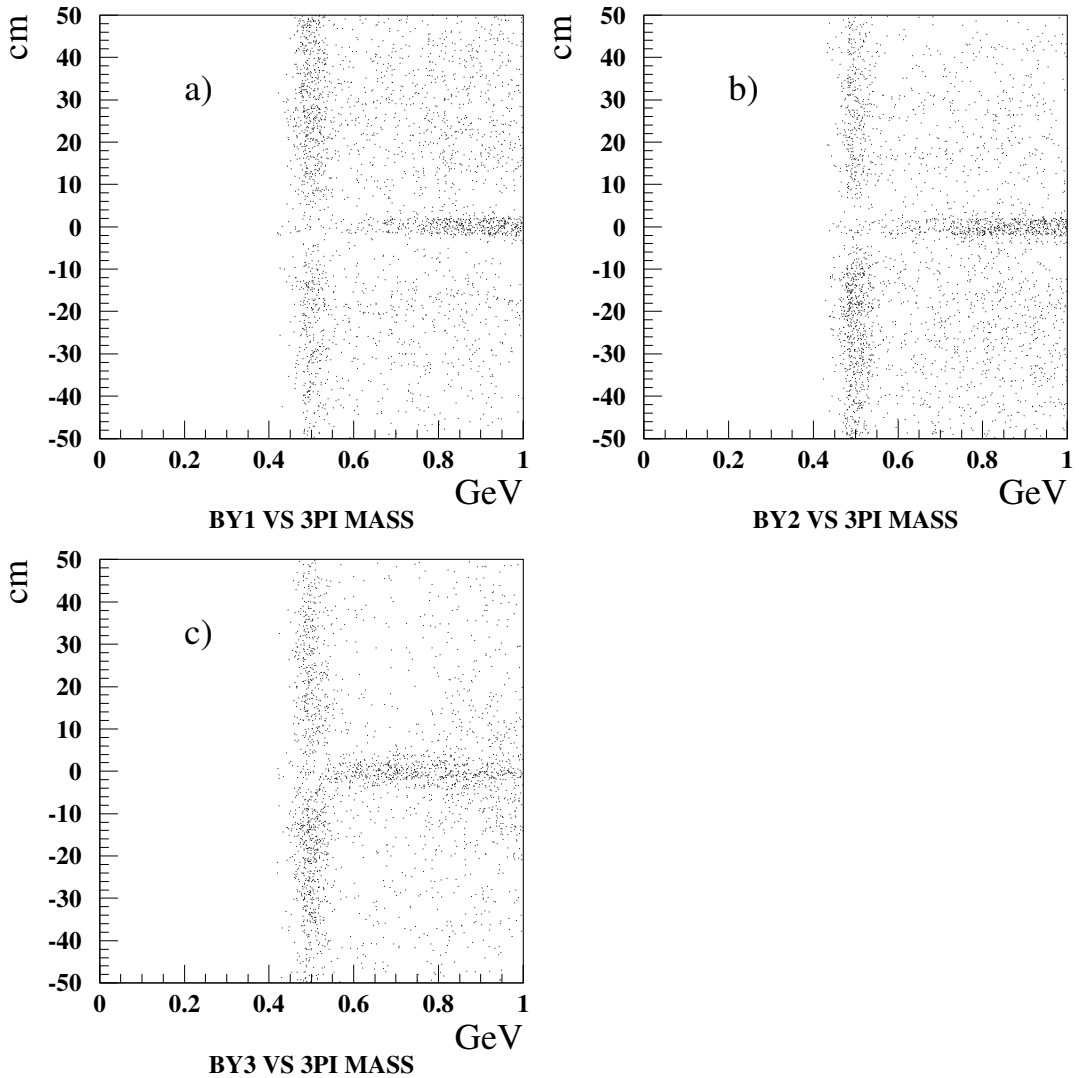

Figure 4.5: Distribution of the impact parameters of the three decay tracks.

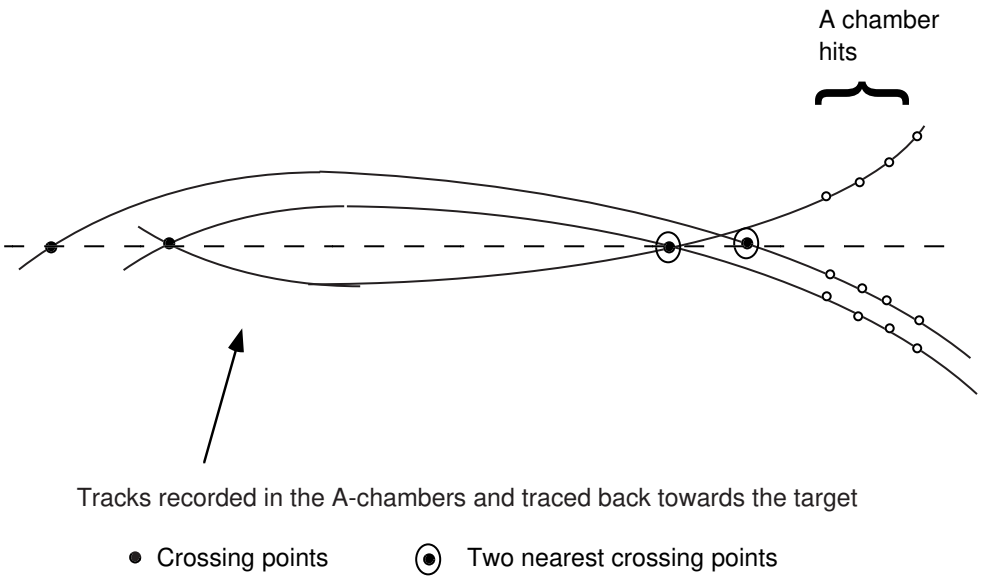

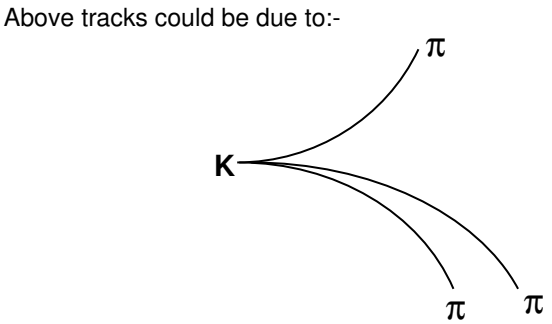

Figure 4.6: A schematic representation of a possible $K^{\pm}$ decay.

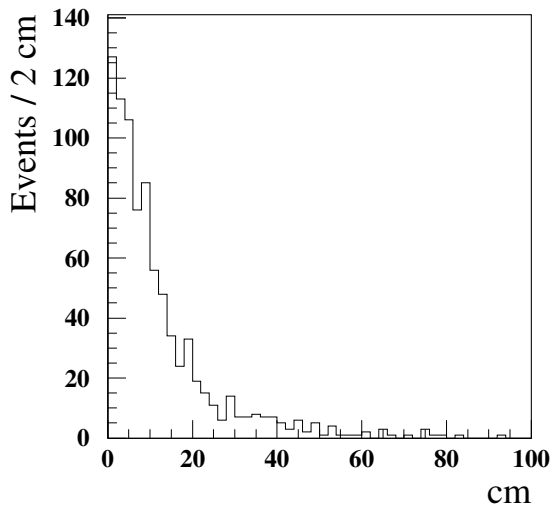

Figure 4.7: Distribution of the distance between the V^0 and the third pion.

to $\pi^+\pi^-$) extrapolated backwards towards the target and the third pions trajectory cross twice, there may be some ambiguity as to which of the two crossings is the real decay point of the $K^{\pm}$ [24]. These crossing points are calculated in STRIPTAU and the 4 distances between the third pion's crossing points and the V^0's crossing points are calculated, figure 4.7 shows the distribution of the minimum of these 4 distances. This distance is then required to be less than 20 cm.

Finally we require that the effective mass lies in the range $(M_K - 50MeV) < M(\pi\pi\pi) < (M_K + 50MeV)$, with M_K taken from [33].

4.2 Summary of cuts used to identify K^- and K^+ meson decays

(i) Each decay track has at least four space points,

(ii) each track traces through the first four MWPCs,

(iii) $M_{\pi\pi} < 0.42$ GeV,

(iv) $|\alpha_{V0}| < 0.45$,

(v) momentum of V^0 >6.5 GeV/c.

(vi) the $K^{\pm}$ vertex lies in the range $-55 < x_\Omega < 71$ cm,

(vii) the $K^{\pm}$ traces back to the target $|\ byk\ | < 2.0$ cm and $|\ bzk\ | < 2.0$ cm,

(viii) the decay tracks miss the target by at least 5 cm, i.e. $|\ by(\pi)\ | \geq 5$ cm for each pion,

(ix) the distance between the V^0 vertex and the third pion's crossing points is less than 20 cm,

(x) the effective mass is in the range,
$(M_K - 50MeV) < M(\pi\pi\pi) < (M_K + 50MeV)$.

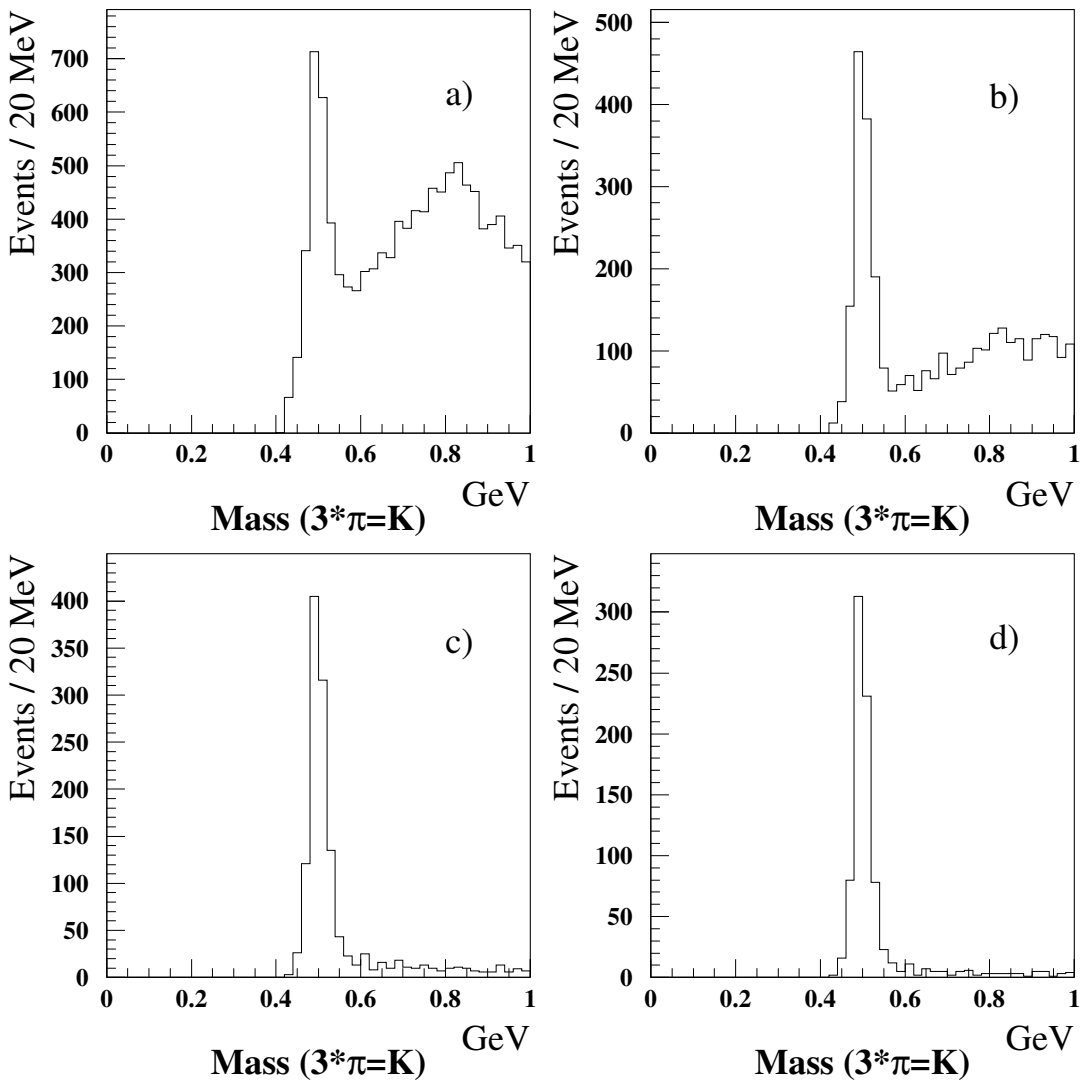

Figure 4.8: Effective mass plots of $K^{\pm}$ candidates after a) having loose WA9XI cuts and cuts i and vi, b) i to v c) i to vii and d) i to viii performed on them.

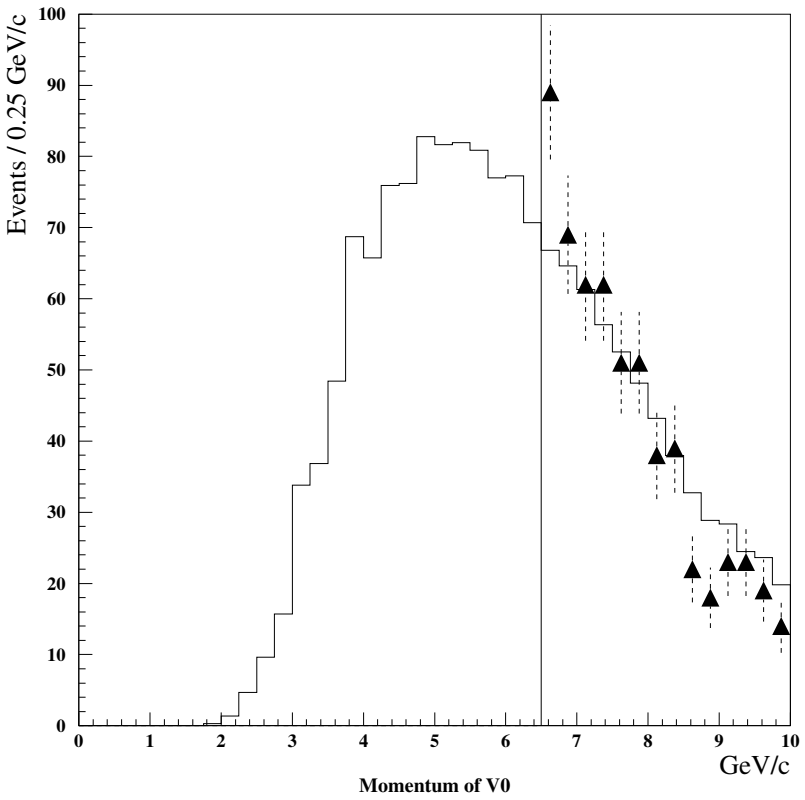

Figure 4.9: Momentum distribution of V^0s superimposed onto V^0s coming from Monte Carlo K decays.

Figure 4.8 shows the effective mass plots of a sample of $K^{\pm}$ candidates after a) having loose WA9XI cuts and cuts i and vi, b) i to v c) i to vii and d) i to viii performed on them. As can be seen from figure 4.8d a clear peak at the $K^{\pm}$ mass can be seen with little background after cuts i to viii have been applied to the candidates.

Figure 4.9 shows the distribution of momentum of V^0s coming from K decays, after all the cuts have been applied to the data, superimposed onto the Monte Carlo distribution, it can clearly be seen that when the tapes are redone a doubling of the statistics should be found. Figure 4.10 shows the effective mass distributions of a) $M(\pi^-\pi^+\pi^-)$ and b) $M(\pi^-\pi^+\pi^+)$ after all the cuts apart from the mass cut has been applied to the candidates. With this mass cut applied we find 202 K^-s and 430 K^+s giving an uncorrected ratio of K^+ to K^- of 2.1 ± 0.2. This ratio needs to

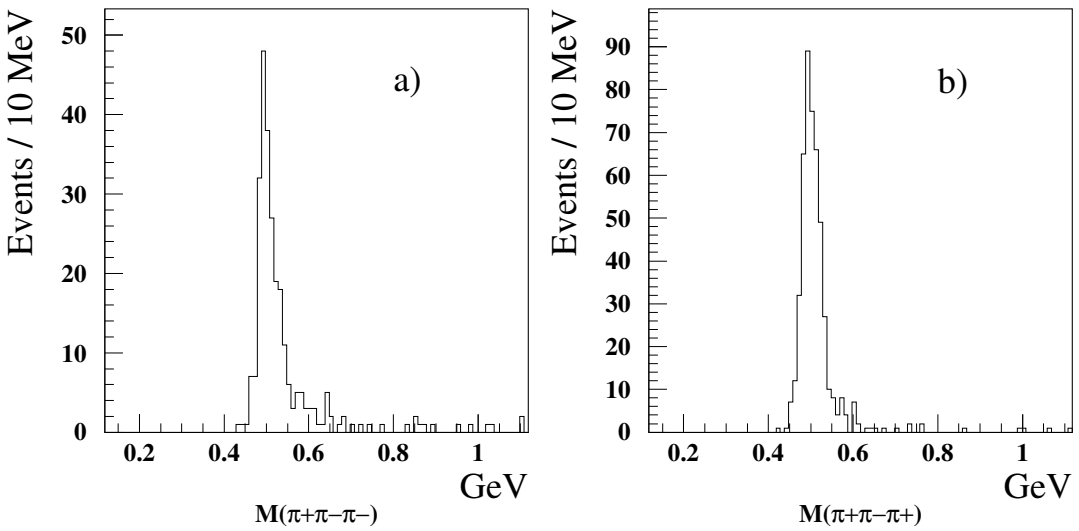

Figure 4.10: Effective mass distributions of a) $M(\pi^+\pi^-\pi^-)$ and b) $M(\pi^+\pi^-\pi^+)$.

be corrected for the acceptance and reconstruction efficiencies of the apparatus to these charged mesons to enable comparison of charged kaon to lambda production. These corrections are discussed next.

Chapter 5

Calculation of Acceptances

It has been shown in the preceding chapters how the various strange particles under study are reconstructed. The raw reconstructed particle numbers in themselves tell us very little about the fireball created by the collision of the ions; what is required is the average numbers of each particle species produced in the interaction and not the reconstructed number. This will enable comparison between the production rates of the different particle species. For example, the comparison of the yields of multistrange baryons with singly strange baryons will provide information on the strangeness content of the created fireball, which the theorists can then use to deduce the most likely model, hadron gas or QGP, which best describes the results.

In order to calculate the true particle yields and hence compare relative production rates it is required that the reconstructed numbers are corrected for:-

- Geometrical acceptance of the apparatus.
- Reconstruction efficiency of the detectors and analysis packages.

In this chapter the acceptance calculations are discussed whilst the reconstruction efficiencies will be discussed in the next chapter. The data needs to be corrected to take account of how the geometry of the detectors constrains the number of particles observed. For a detector to have an acceptance of 100% all the particles produced in the interaction should pass through it. As stated in chapter 2 the WA94 detectors, specifically the Omega A MWPCs, only cover a narrow phase space window and

therefore it is important to know how this limits the detection of the particles produced in the interaction. The data also needs to be corrected to take account of unseen decay modes, such as $K^+ \rightarrow \mu^+ + \nu_\mu$, and also decays outside of the fiducial volume.

The acceptances are evaluated using Monte Carlo programs which generate a large known number of particles in a wider phase space window than is covered by the MWPCs. The region of acceptance studied is divided into a grid, with each element of size 0.05 units of rapidity by 0.1 GeV/c in transverse momentum. The acceptance is then calculated individually for each grid square.

5.1 Λ Acceptance

To calculate the acceptances of the chambers with regard to Λ decays Monte Carlo Λs are generated with a lab rapidity, Y_{LAB}, and transverse momentum, p_T, corresponding to the centroid of the grid element under study. The Λ is assigned the following momentum vectors,

$$p_L = m_T + sinh(Y_{LAB}) \qquad\qquad m_T = \sqrt{M_\Lambda^2 + p_T^2}$$

where p_L is the longitudinal momentum and m_T is the transverse mass;

$$p_x = p_L / \mid p \mid \qquad\qquad \mid p \mid = \sqrt{p_T^2 + p_L^2}$$

and,

$$p_y = p_T cos(phi) \qquad\qquad p_z = p_T sin(phi),$$

where phi is a random number generated between 0 and π, i.e. to save computer time only decays in the upper hemisphere are considered.

The Λ is then made to decay, with a decay length given by a random distribution determined by the mean lifetime, τ, of a Λ decay. The probability, $P(x_o)$, that a particle of mass M travels a distance x_o or greater is given by,

$$P(x_o) = e^{-Mc^2 x_o \Gamma / \mid p \mid},$$

where $\Gamma = 1/c\tau$ and $|p|$ is the momentum of the particle. Rearranging this equation gives,

$$x_o = -\frac{-c\tau\ |p|}{Mc^2} \ln(P(x_o)).$$

The decay distance, d, of the Λ is made to be,

$$d = -\frac{c\tau\ |p|}{M_\Lambda c^2} \ln(R),$$

where R is a random number generated between 0 and 1; $c\tau$ of the Λ is 7.89 cm. Once the decay length is calculated the position of the vertex of the Λ is found and required to be in the fiducial region $-80 < x_\Omega < 71$ cm as this is the region in that the reconstructed Λ vertices lie, see chapter 3.

The decay tracks are assigned in x, y and z an equal but opposite random 3-dimensional momentum vector of length p^*, where p^* is the momentum of each decay product in the rest frame of the decaying particle, $p^* = 0.101$ GeV/c for Λs. The decay tracks momenta are then transformed from the centre of mass rest frame to the lab frame. The decay tracks are then traced through the MWPCs, if they pass through A1 and A7, and the Λ decay is unambiguous, i.e. $0.45 < \alpha < 0.6$, the decay is then counted as an accepted decay. The total acceptance is then given by

$$\text{Acceptance} = \frac{\text{no.accepted}}{\text{no.generated}} \times \frac{1}{2} \times 0.641$$

where the factor of 1/2 takes account of the fact that the Λs were only generated in the upper hemisphere, and the factor of 0.641 takes account of the unseen decay modes. The acceptance of Λs over the Y_{LAB} and p_T ranges considered are shown in figure 5.1.

5.2 Ξ Acceptance

The calculation of Ξ acceptances is more complicated than the Λ case as two decays need to be considered,

$$\Xi^- \rightarrow \Lambda + \pi^- \quad \text{with} \quad \Lambda \rightarrow p + \pi^-.$$

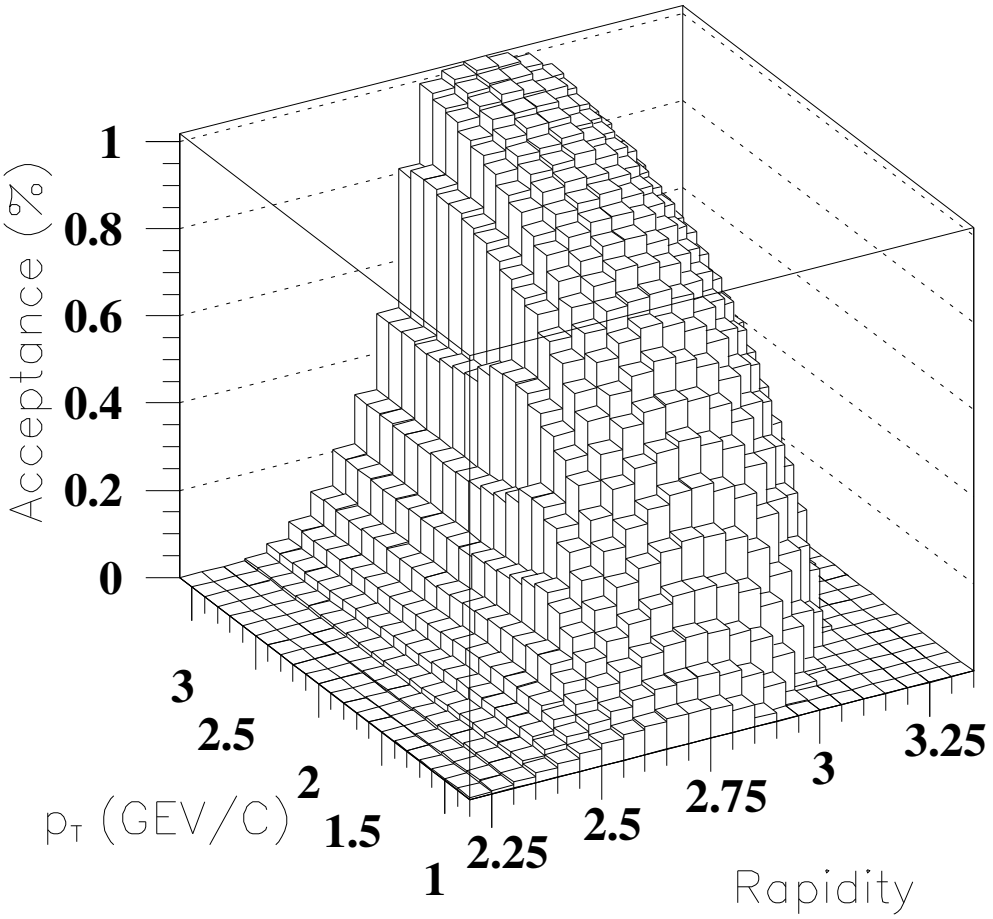

Figure 5.1: Geometrical acceptance of unambiguous Λs as a function of rapidity and p_T.

The Monte Carlo Ξs are generated with a rapidity Y_{LAB} and p_T and the momentum vectors are calculated as for Λs. The Ξ decay length is then calculated from

$$d = -\frac{c\tau \mid p \mid}{M_{\Xi}c^2} \ln(R),$$

with $c\tau$ of the Ξ being 4.91 cm. The position of the Ξ vertex is then determined and required to lie in the fiducial region $-125 < x_{\Omega} < 71$cm. In a similar way to the Λ decay the Ξ decay particles (the Λ and π) are assigned equal but opposite 3 momenta vectors in the centre of mass rest frame which are then transformed to the lab frame. The π is required to trace through the first four MWPCs, and to miss the target by at least 6 cm as this is a geometrical cut that is applied to the Ξ candidates and would otherwise bias the p_T spectra. The Λ from the Ξ decay is then decayed with its decay tracks traced through the chambers as when calculating the Λ acceptance except these Λs are traced from the vertex of the Ξ and not the target and its decay products have to trace through A1-A4 and not A1-A7. Figure 5.2 shows the acceptance of Ξs as a function of Y_{LAB} and p_T.

5.3 K Acceptance

The calculation of the charged kaons acceptance is different from the other two in that the $K^{\pm}$ decays to three particles i.e. $K^+ \rightarrow \pi^+\pi^-\pi^+$. The Ks are generated in the same way as the Λs and Ξs and made to decay with a decay length given by

$$d = -\frac{c\tau \mid p \mid}{M_K c^2} \ln(R),$$

where $c\tau$ of the K is 370.9 cm. If the K vertex lies in the region $-55 < x_{\Omega} < 71$ cm then it is made to decay into three particles, each with the mass of a pion and having centre of mass momenta (and energies) distributed randomly between the three particles but giving a total of centre of mass energy equal to the mass of a charged kaon. The momentum vectors are then Lorentz boosted to the lab frame.

The decay particles are then required to trace through the first four MWPCs, it is also required that the decay tracks must miss the target by at least 5 cm as this is a geometrical cut that is applied to the charged kaon candidates and would

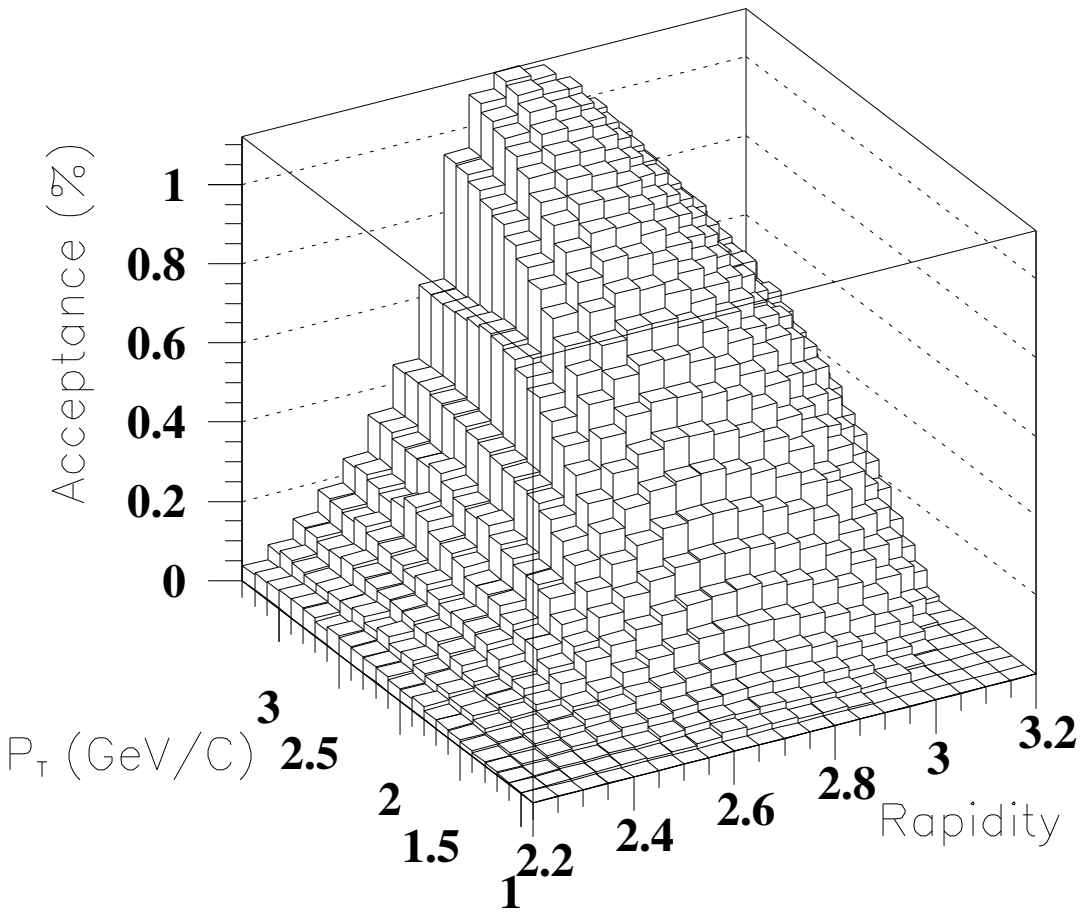

Figure 5.2: Geometrical acceptance of Ξ^-s as a function of rapidity and p_T.

bias the p_T spectra as in the Ξ case. Furthermore the oppositely charged tracks are required to have combined momenta greater than 6.5 GeV/c as this is a cut that has been applied to the data and biases against the reconstruction of charged kaons with lower p_T and rapidity.

The acceptance of the kaons are then given by

$$\text{Acceptance} = \frac{\text{no.accepted}}{\text{no.generated}} \times \frac{1}{2} \times 0.0559,$$

the factor 0.0559 is the branching ratio of the decay $K^+ \to \pi^+\pi^-\pi^+$. The acceptance of the Ks are shown in figure 5.3. The acceptance tables for Λs, Ξ^-s and K^+s are given in appendix C.

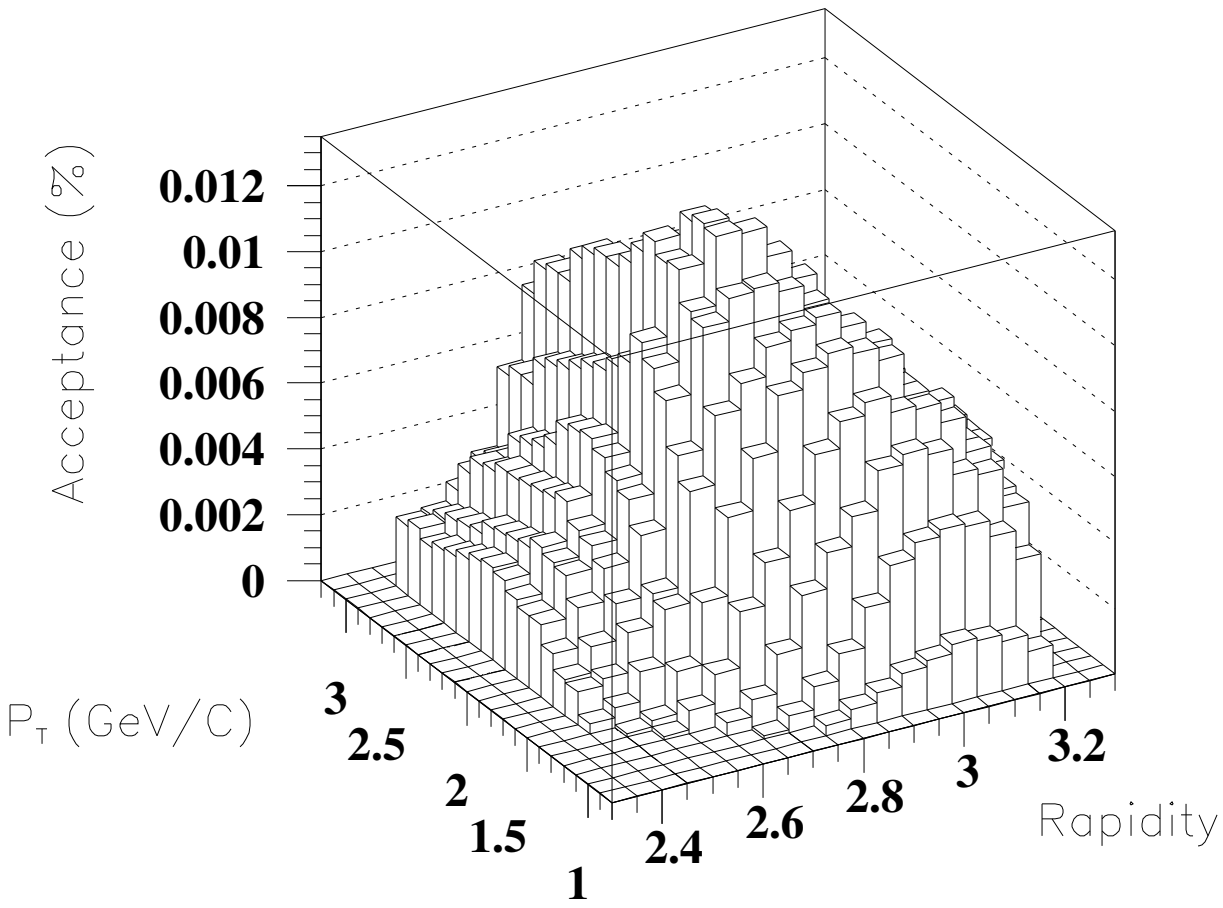

Figure 5.3: Geometrical acceptance of charged kaons as a function of rapidity and p_T.

Chapter 6

Reconstruction Efficiencies

As mentioned in the preceding chapters WA94's aim is to study the relative production rates of strange and multistrange particles and antiparticles. Therefore as well as calculating the acceptance of the detectors to the particles produced in the interactions, the efficiency of the detectors and the analysis programs which reconstruct the particles needs to be calculated.

To this end a number of Monte Carlo particles are generated according to given distribution functions, rather like in the acceptance case. The Monte Carlo particles are then traced through the Omega magnetic field and their intersection points with the chambers wires calculated. At each intersection point a cluster of wire hits is generated, taking into account the efficiencies of the various planes of the chambers. Real events are then read from a TRIDENT output tape, which contains information on the wire hits in the MWPCs chambers and the Monte Carlo hits are then merged with real hits, forming a realistic background to the decay in the resulting composite event and a new file is written in the format of raw data and then fed through the normal analysis chain. By identifying the Monte Carlo particles which are successfully reconstructed the reconstruction efficiency can be found as a function of the charged track multiplicity in the wire chambers. The flow chart shown in figure 6.1 summarises the procedure used to evaluate the reconstruction efficiencies.

As mentioned, the reconstruction efficiency is dependent on two factors; the

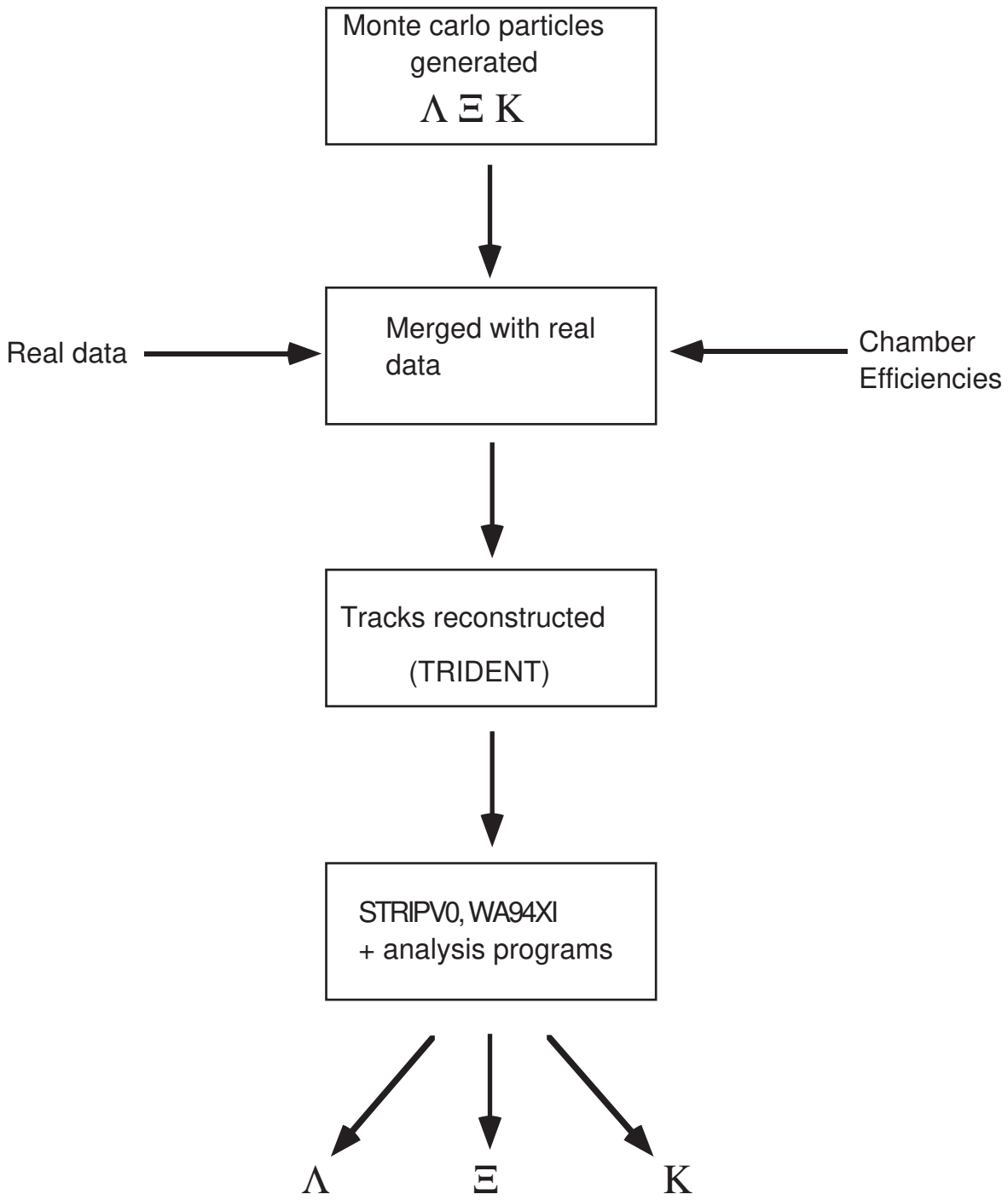

Figure 6.1: Flow of processes used to calculate the reconstruction efficiencies of the different particles reconstructed by WA94 in the sulphur-sulphur interactions.

efficiency of the wire chambers in recording a track caused by a particle passing through it, and the efficiency of the software in correctly fitting the tracks. The efficiency of the chambers will be discussed first.

6.1 Calculation of the Chamber Efficiencies

To calculate the chamber efficiency TRIDENT is run on a sample of raw data with the chamber under study removed out of the track fitting routine, making the reconstructed tracks completely independent of this chamber. The efficiency is then calculated by tracing 'good' tracks through each plane of the chamber and checking whether any wire within 2 mm (the wire pitch) of the impact fire. 'Good' tracks trace through A1-A7, have six space points and trace back to the target. The efficiency is then determined by the number of such successful detections divided by the total number of 'good' tracks traced through the chamber.

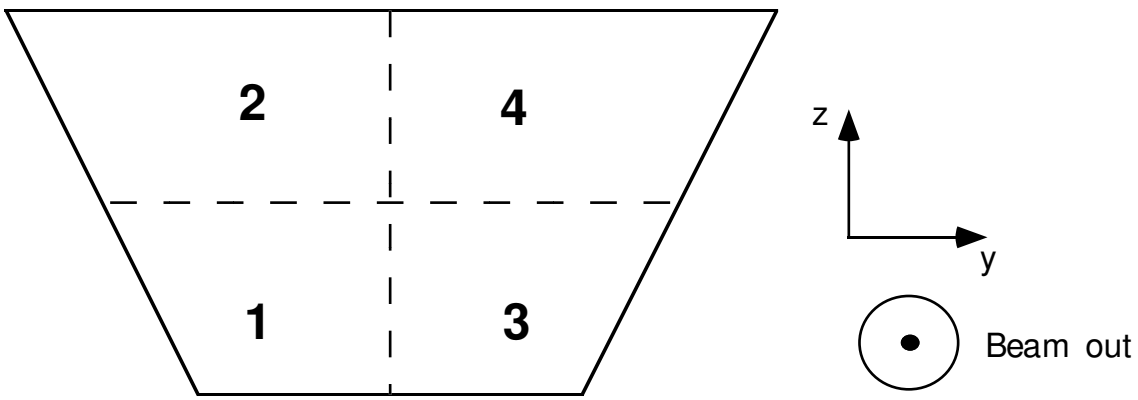

Figure 6.2: The four logical quadrants of the MWPCs.

As well as the chamber consisting of 3 planes, as mentioned in chapter 2, for the purpose of the efficiency study, each plane is split into four logical quadrants as shown in figure 6.2. Therefore 84 (7 chambers $\times$ 3 planes $\times$ 4 quadrants) efficiencies are calculated and then used in the implantation of the Monte Carlo data into real data.

6.1.1 Chamber Edge Effects

A study has been carried out [34] to see how the chamber efficiency varies at the edge of the chamber, as can be seen in figure 6.3 a), b) and c), which shows the variation in chamber efficiency close to the edge of the butterfly region of the Y, U and V planes of chamber 1 respectively, there is a gradual fall off in efficiency over the last cm which would be a source of systematic error if not accounted for. The population of reconstructed tracks close to the edge of the butterfly region of the chamber are shown in figure 6.3 d); the population decreases near the edge due to falling efficiency meaning the probability of reconstructing a track will be less. To ensure that analysis was performed in a uniform region of efficiency a 1 cm band around the edge of the chambers is removed from analysis calculations.

6.1.2 Chamber Efficiency Results

The efficiencies of the chambers used in the 1991 sulphur sulphur run have been calculated from data sampled through out the run, the average efficiencies of the 7 A chambers are shown in figure 6.4, whilst the efficiencies of the planes and quadrants of the 7 chambers are listed in full in appendix D.

6.2 Structure of raw data events

In order for the Monte Carlo data to reproduce real data, the composite event made up of the Monte Carlo data merged with the real data must be in exactly the same format as raw data. Therefore it is important to understand the structure of a raw event, i.e. TRIDENT input.

As mentioned at the end of chapter 2 raw data taken in the run are written to tape in EPIO format (machine independent). Each event is written in the form of 16 bit words, when possible several logical records (events) are blocked together to fill in a physical record. A logical record has a structure as shown in figure 6.5. The header block, with NH header words, gives information about the event, such as the length of the event, word 1; the event type, be it a trigger, beginning of burst or end

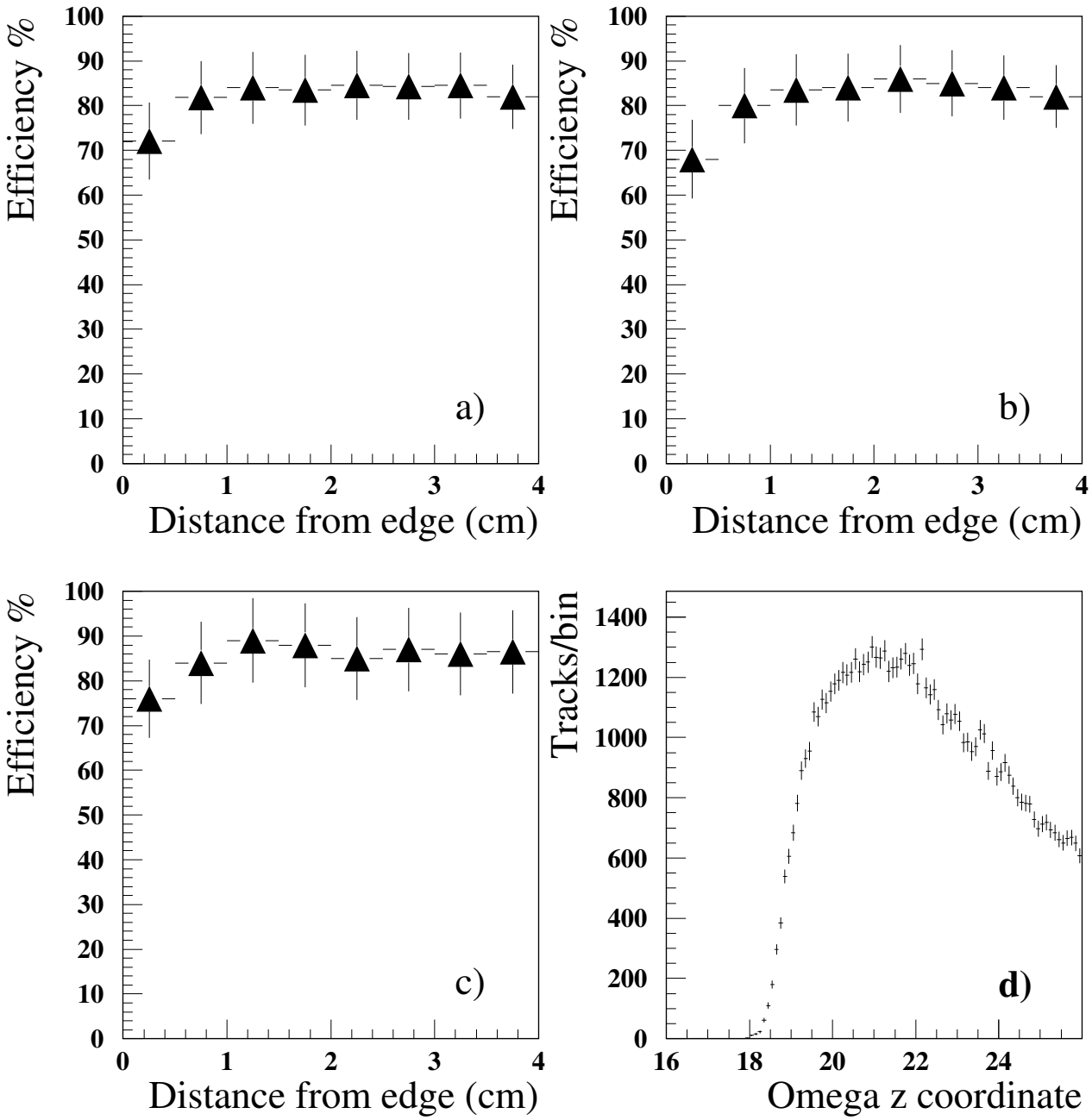

Figure 6.3: The variation in chamber efficiency close to the edge of the butterfly region of chamber 1, plane Y (a), plane U (b) and plane V (c). The population of reconstructed tracks at the edge of the butterfly region are shown in (d).

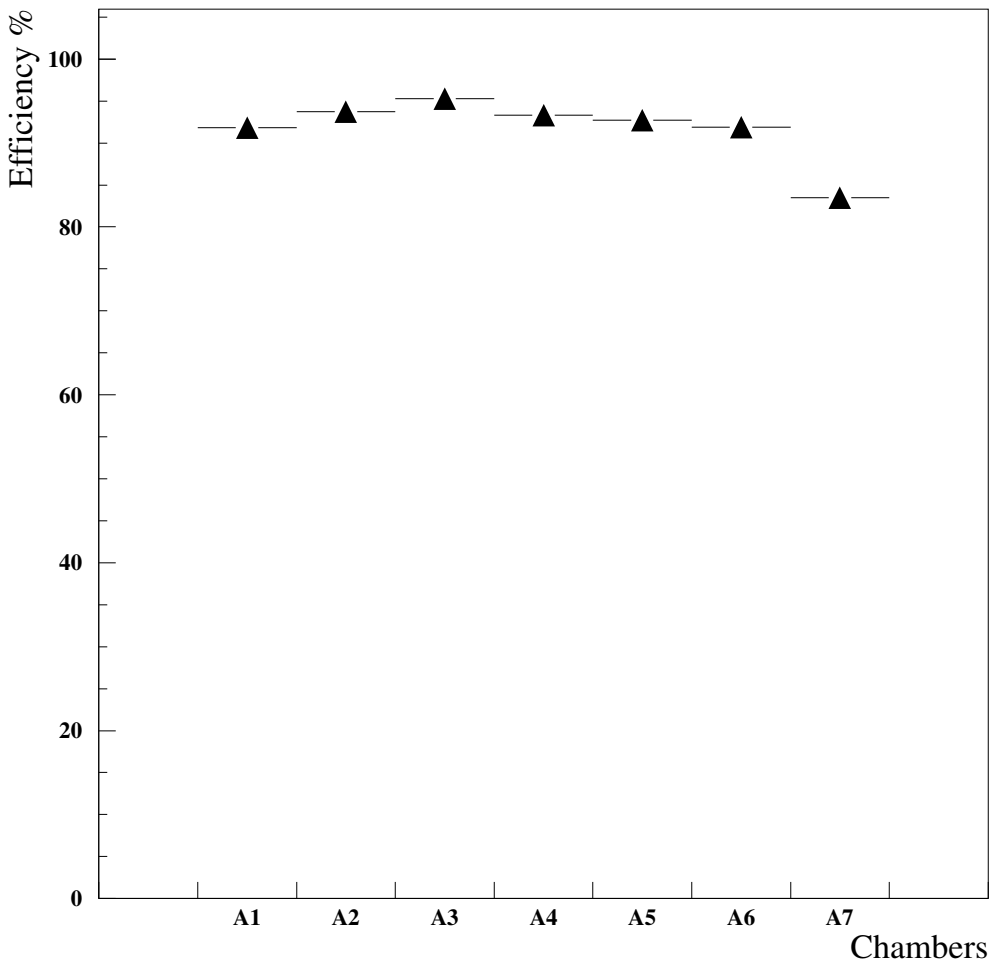

Figure 6.4: Chamber efficiencies of the 7 A chambers used by WA94 in the 1991 S-S run.

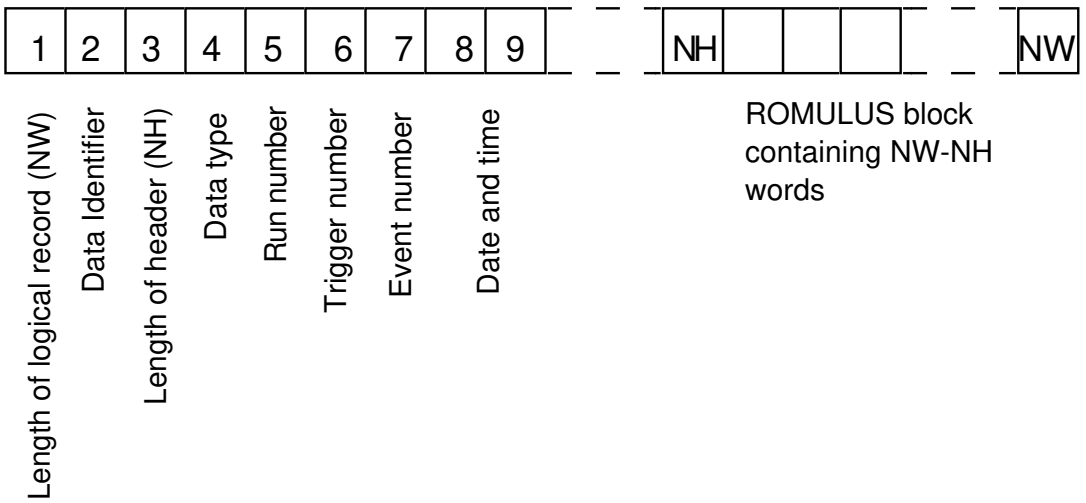

Figure 6.5: Structure of a raw data event.

of burst event, given by word 2; and the time when it was recorded [1], words 8-11. The first word, which gives the length of the event, enables TRIDENT to find the end of the record, which is the 'top' end of the ROMULUS structure, shown in figure 2.8. This ROMULUS block contains all the information on wire hits, cluster sizes etc. that TRIDENT needs to reconstruct the tracks in the chambers. TRIDENT then gives an output record consisting of several blocks, the first one is called the header block and contains information on the structure of the record and is shown in figure 6.6. The electronic data block is just the ROMULUS block that was the TRIDENT input, the results of the tracks reconstruction are given in the geometry block.

6.3 Implantation of the Monte Carlo data

The Monte Carlo tracks are traced through the Omega magnetic field, the points of intersection with the wires in the chambers are calculated. If a track is traced between two wires, both wires are fired if the distance of the track from the wires is greater than a 1/3 of the wire pitch distance of 2mm, if not then the one nearest

[1]The time is given in the VAX system time, which is of the form of the Smithsonian base date and time for the astronomical calendar, which is the number of nanoseconds which have passed since midnight, November 17,1858.

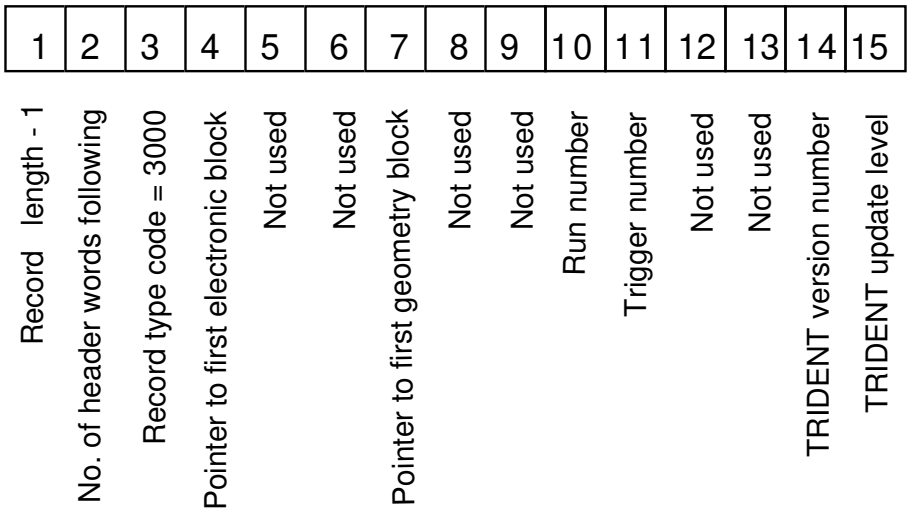

Figure 6.6: Structure of TRIDENT header block.

to the track is made to fire. To ensure that the Monte Carlo tracks behave like real tracks, before a hit is registered the efficiency of the quadrant of the plane that the track is passing through is consulted and thus the Monte Carlo particle is not recorded perfectly by all the wire planes. Real data is read in from TRIDENT output tapes and the part of the ROMULUS block containing the wire chamber information is unpacked into an array of wire hits. The array of hits from the Monte Carlo tracks and real tracks are then merged together and repacked into a new ROMULUS block, with the header block adjusted to take account of the extra words arising due to the wire hits caused by the Monte Carlo particles. The whole event is then written to tape in EPIO format.

6.4 Λ Reconstruction Efficiencies

As mentioned in chapter 3, we require the Λ candidates to lie in the range $-80 < x_\Omega < 71$ cm, and to be unambiguous, i.e. $0.45 <\mid \alpha \mid < 0.6$. We furthermore require that the Λ has rapidity, Y_{LAB}, in the range $2.5 < Y_{LAB} < 3.2$ and p_T between 1.0 and 3.0 GeV/c, as outside this region the acceptance for Λs traced through the seven A chambers (with the 1 cm cut) falls below $\sim 10\%$ of its maximum value. However the Monte Carlo particles must be generated in a slightly larger acceptance window to take account of inaccuracies in the momentum and position measurements due to the

finite resolution of the detector system. By generating in a slightly larger window, particles from outside the region are smeared into the right kinematic region as well as some inside the region being lost due to being reconstructed slightly outside the region. The Monte Carlo Λs are generated with an exponential decay, as in the acceptance case, but with the following conditions:

- the vertex lies in the region $-100 < x_\Omega < 71$ cm,
- the rapidity distribution is flat, in the range $2.3 < Y_{LAB} < 3.4$,
- $0.8 < p_T < 3.2$ GeV/c,
- they obey a distribution given by,

$$\frac{1}{\mathrm{m_T^{\frac{3}{2}}}}\frac{\mathrm{dN}}{\mathrm{dm_T}} \sim \exp^{-\beta \mathrm{m_T}},$$

  where β is determined from the real data, corrected for acceptances,
- the Λs are generated at the target with a Gaussian distribution of width 1 mm,
- the Monte Carlo decays are isotropic.

In figure 6.7 the vertex distribution of a) the generated Λs and b) the generated Λs after passing through the chain of analysis programs can be seen, with the dotted line showing the real reconstructed Λs vertex position after all the cuts are applied to it. The Λ is then decayed as for the acceptance calculation, and its decay tracks are then traced through A1-A7 with the 1cm edge cut. The Monte Carlo particles are then subjected to the same cuts as are applied to the real data, i.e.

- the vertex lies in the region $-80 < x_\Omega < 71$ cm,
- the rapidity distribution is flat, in the range $2.5 < Y_{LAB} < 3.2$,
- $1.0 < p_T < 3.0$ GeV/c,
- the Λs momentum is > 6.5 GeV/c,

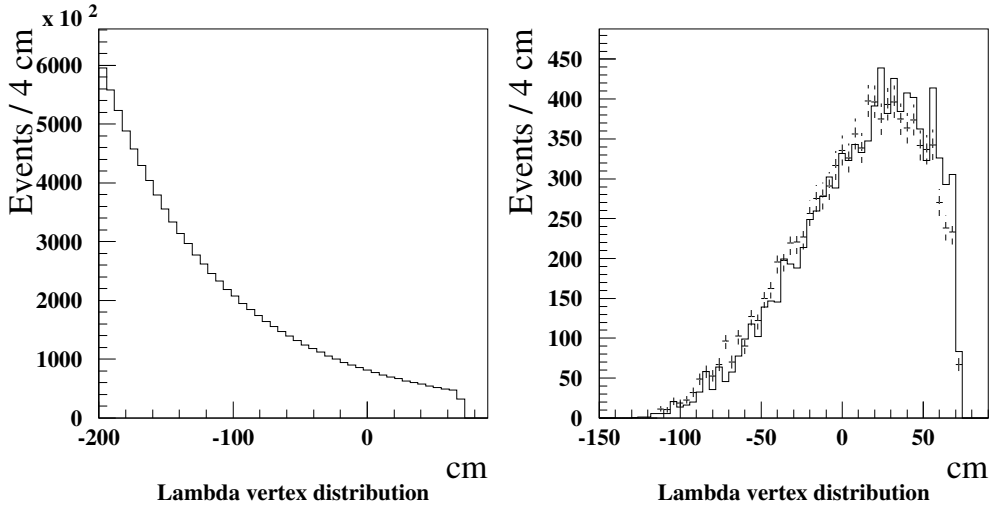

Figure 6.7: Vertex distribution of a) Monte Carlo Λs and b) Monte Carlo Λs after passing through the analysis chain, the dots represent real data.

- it is unambiguous, i.e. the condition $0.45 <| \alpha |< 0.6$ is applied to remove contamination of K^0s.

If the Monte Carlo Λ successfully passes these conditions, they are tagged and the wire hits are found and identified. These data are then used to merge the Monte Carlo data with the real data, as well as this the average number of cluster hits in the A chambers is recorded for these tagged events. If adjacent wires fire the hit is recorded as a cluster, and the first wire fired and the number of fired wires are given. The average charged track multiplicity in the wire chambers is then given by the sum of the clusters in each plane divided by 21 (3 planes $\times$ 7 chambers). The merged data are then processed using TRIDENT, STRIPV0, and the final analysis program which performs the cuts to extract 'good' Λ decays. Figure 6.8 shows the mass distribution of real Λs, together with the mass distribution of the same number of Monte Carlo Λs. The wire chamber multiplicity distribution is then found for these 'good' Λ and the efficiency is then simply given by,

$$\text{Efficiency} = \frac{\mathrm{N_{Rec}}}{\mathrm{N_{Gen}}},$$

where $\mathrm{N_{Gen}}$ is the number of tagged generated events, and N_{Rec} is the number of reconstructed events. The reconstruction efficiencies as a function of MWPC cluster multiplicity are shown in figure 6.9 for a) Λs field down (B=1.8T $\downarrow$, the normal

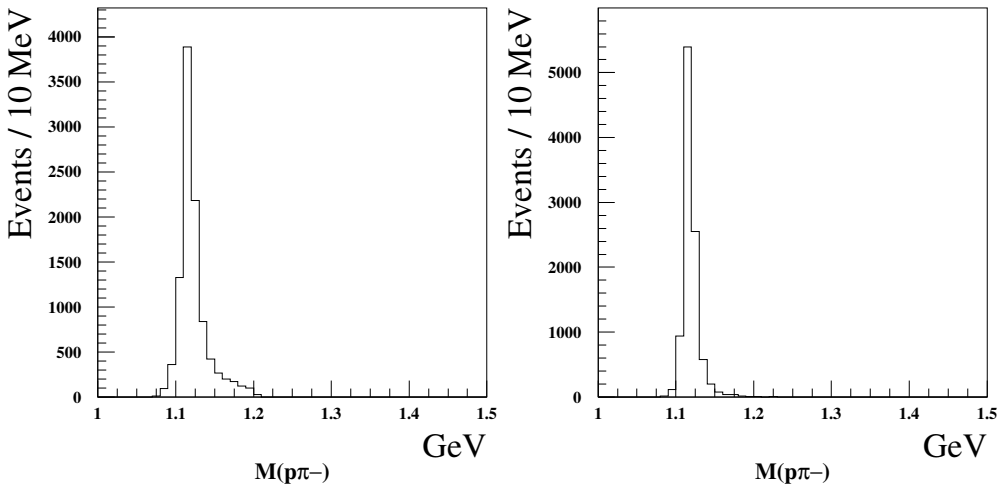

Figure 6.8: Mass distribution of a) Real Λs and b) Monte Carlo Λs.

polarity of the Omega magnetic field) b) $\overline{\Lambda}$s (B=1.8T $\downarrow$), c) Λs (B=1.8T $\uparrow$) and d) $\overline{\Lambda}$s (B=1.8T $\uparrow$). Also shown in figure 6.9a), dotted line, is the multiplicity distribution for a sample of background data, it can be seen that outside the multiplicity region of 4 to 16 the statistics are low. The data are therefore restricted to have an average number of clusters per plane of between 4 and 16.

6.5 Ξ Reconstruction Efficiencies

The Monte Carlo Ξs are generated with an exponential decay, with the following characteristics,

- the Ξ^- decays in the region $-150 < x_\Omega < 71$ cm,
- the Λ vertex lies in the region $-100 < x_\Omega < 71$ cm,
- the rapidity distribution is flat, in the range $2.3 < Y_{LAB} < 3.2$,
- $0.8 < p_T < 3.2$ GeV/c,
- they are distributed according to,

$$\frac{1}{\mathrm{m_T^{\frac{3}{2}}}}\frac{\mathrm{dN}}{\mathrm{dm_T}} \sim \exp^{-\beta \mathrm{m_T}},$$

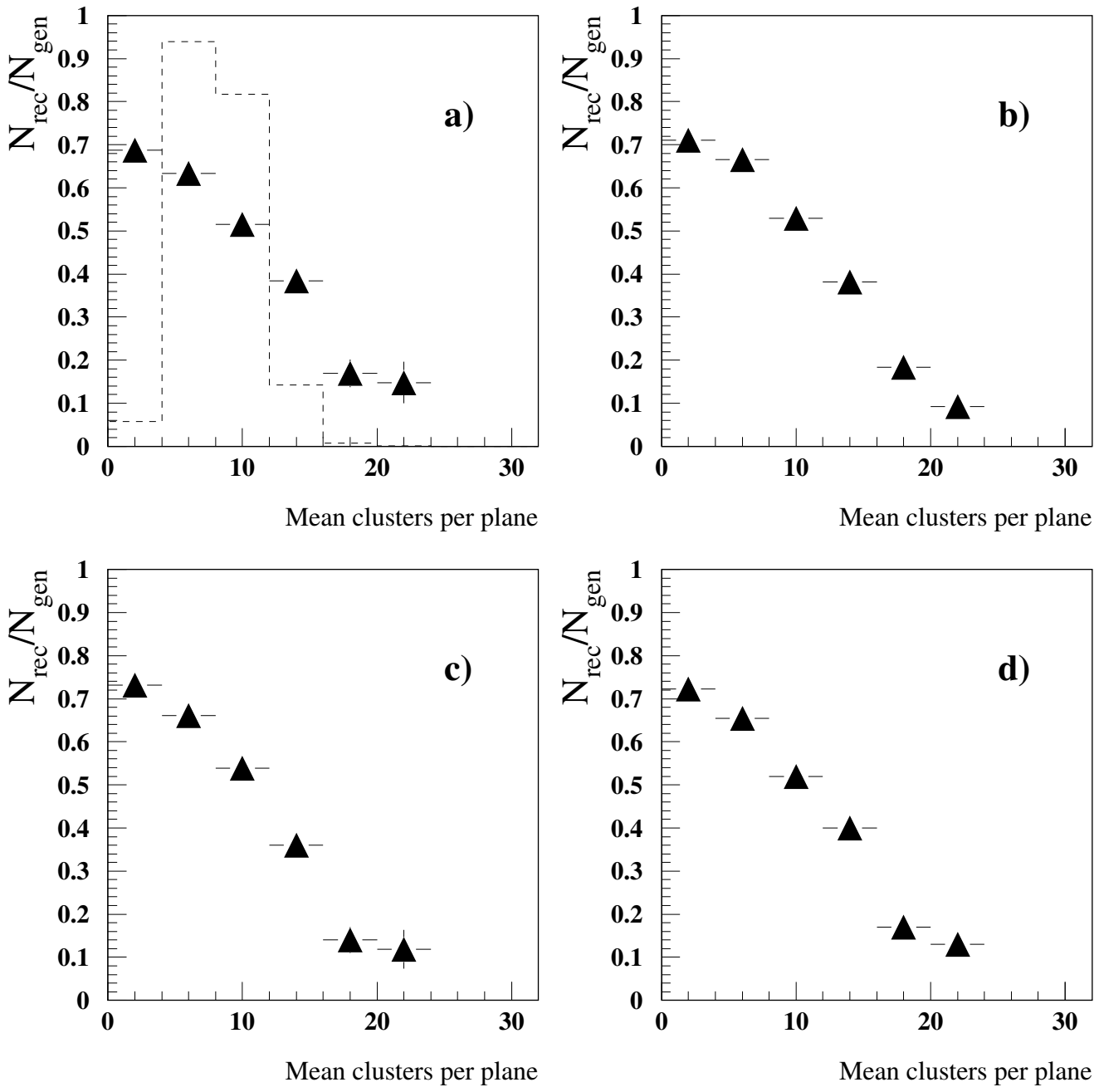

Figure 6.9: Reconstruction efficiencies as a function of MWPC cluster multiplicity for a) Λs field down (B=1.8T $\downarrow$), b) $\overline{\Lambda}$s (B=1.8T $\downarrow$), c) Λs (B=1.8T $\uparrow$) and d) $\overline{\Lambda}$s (B=1.8T $\uparrow$).

- the Ξs are generated at the target with a Gaussian distribution of width 1 mm,

As in the Λ case it can be seen, figure 6.10, that once the Monte Carlo Ξs, which are decayed exponentially, are passed through the analysis chain their vertex distribution is similar to that of the real data.

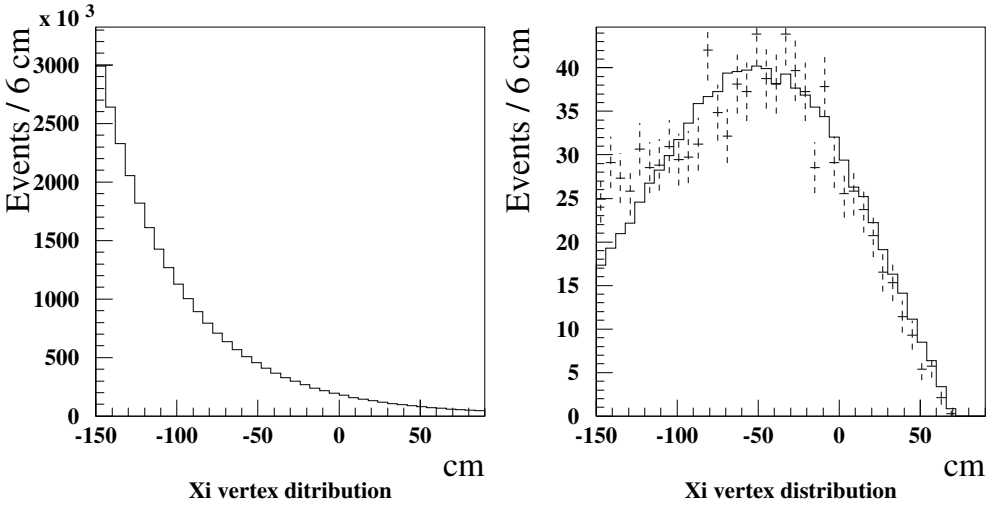

Figure 6.10: Vertex distribution of a) Monte Carlo Ξs and b) Monte Carlo Ξs after passing through the analysis chain, the dots represent real data.

The wire hits in the chambers are then recorded if the Ξ satisfies the following requirements:

- the Ξ^- decays in the region $-125 < x_\Omega < 71$ cm,
- the Λ vertex lies in the region $-80 < x_\Omega < 71$ cm,
- the rapidity distribution is flat, in the range $2.5 < Y_{LAB} < 3.0$,
- $1.0 < p_T < 3.0$ GeV/c,
- the 3 decay tracks of the Ξ trace through A1 and A4 with the 1 cm cut applied.

Real data are then merged with the Monte Carlo Ξs and then processed through TRIDENT, STRIPV0, WA94XI and a final analysis program to reconstruct the Monte Carlo cascades, applying all the cuts that are applied to the data. The

multiplicity distribution of the charged tracks in the wire chambers is then found and divided with the multiplicity distribution of the Monte Carlo Ξs obtained before merging to get the reconstruction efficiencies for Ξs. These efficiencies for Ξ^-s, $\overline{\Xi^-}$s field down, field up and Ξ^-s, $\overline{\Xi^-}$s field up are shown in figures 6.11 a),b),c) and d) respectively.

6.6 K Reconstruction Efficiencies

As mentioned in chapter 5, the cut imposed at the STRIPV0 level on the momentum of the V^0 (P > 6.5 GeV/c) is biased against charged kaons with lower rapidity and p_T. The window defined by requiring that the acceptance does not vary by more than $\sim$ 10% is $2.7 < Y_{LAB} < 3.2$ and $1.0 < p_T < 3.0$ GeV/c. The Monte Carlo charged kaons are generated with the following variables:

- the vertex lies in the region $-80 < x_\Omega < 71$ cm,
- the rapidity distribution is flat, in the range $2.5 < Y_{LAB} < 3.3$,
- $0.8 < p_T < 3.2$ GeV/c,
- they obey a distribution given by,

$$\frac{1}{\mathrm{m_T^{\frac{3}{2}}}}\frac{\mathrm{dN}}{\mathrm{dm_T}} \sim \exp^{-\beta \mathrm{m_T}},$$

- the charged kaons are generated at the target with a Gaussian distribution of width 1 mm.
- the Monte Carlo decays are isotropic.

A look at the vertex distribution, figure 6.12a), shows the effect of the long decay length of the charged kaons, mentioned in chapter 5. The results of the Monte Carlo data passing through the analysis chain is seen in figure 6.12b) with the Monte Carlo distribution, solid line, mimicking the data. The charged kaon is then decayed as in the acceptance case and the tracks traced through the Omega magnetic field; the wire chamber hits are recorded if:

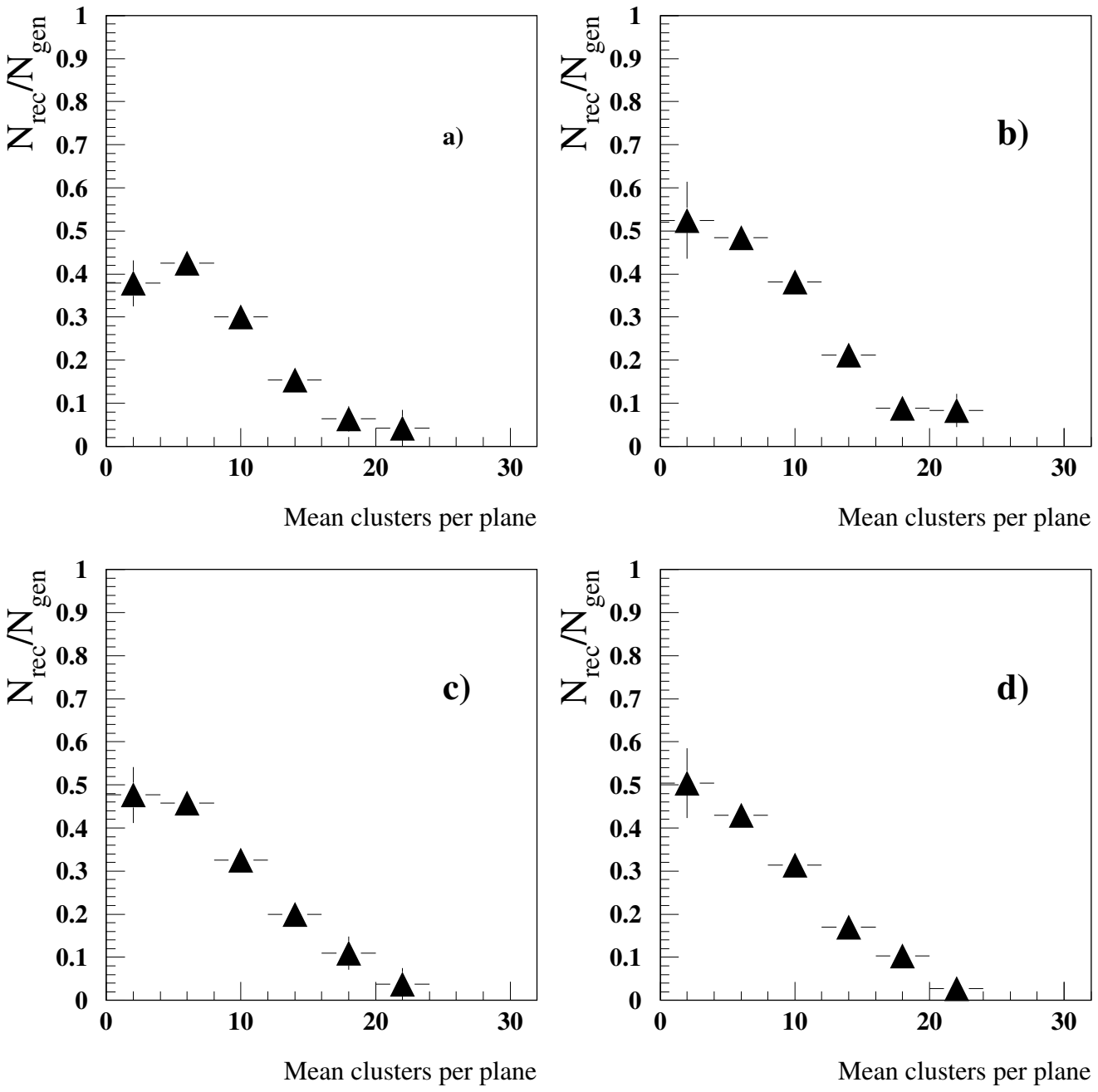

Figure 6.11: Reconstruction efficiencies as a function of MWPC cluster multiplicity for a) Ξ^-s field down, b) $\overline{\Xi^-}$s (B=1.8T $\downarrow$), c) Ξ^-s (B=1.8T $\uparrow$) and d) $\overline{\Xi^-}$s (B=1.8T $\uparrow$).

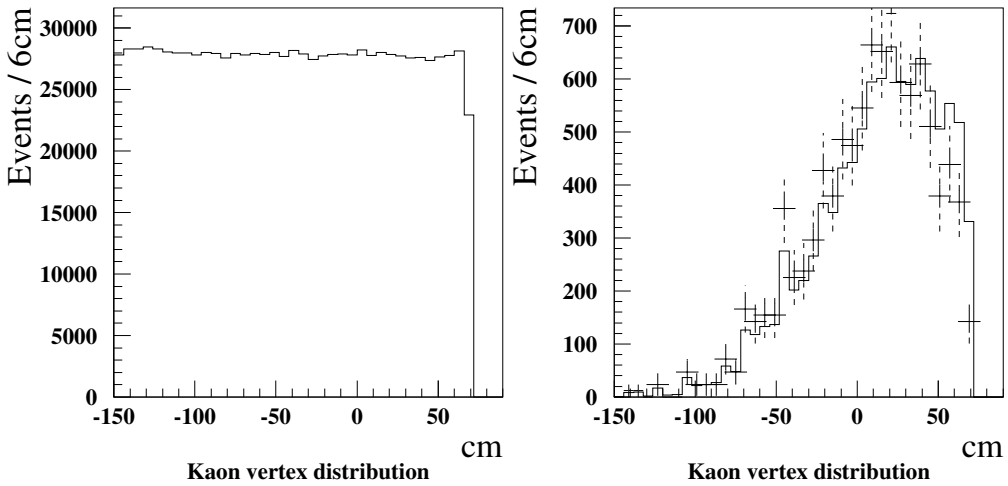

Figure 6.12: Vertex distribution of a) Monte Carlo Ks and b) Monte Carlo Ks after passing through the analysis chain, the dots represent real data.

- the vertex lies in the region $-55 < x_\Omega < 71$ cm,
- the rapidity distribution is flat, in the range $2.7 < Y_{LAB} < 3.2$,
- $1.0 < p_T < 3.0$ GeV/c,
- the V^0s momentum is > 6.5 GeV/c,
- the 3 decay tracks trace through A1 and A4 but not within 1 cm of the edge of the active region of the chambers.

The Monte Carlo particles are then merged with real data, and fed through the normal analysis chain, the reconstruction efficiencies are again found by dividing the wire chamber multiplicity of the events which pass through the analysis chain with the wire chamber multiplicity obtained from the Monte Carlo kaons before entering the analysis chain. The reconstruction efficiencies are shown in figure 6.13 a) K^+ (normal field), b) K^- (normal field) c) K^+ (inverted field) and d)K^- (inverted field).

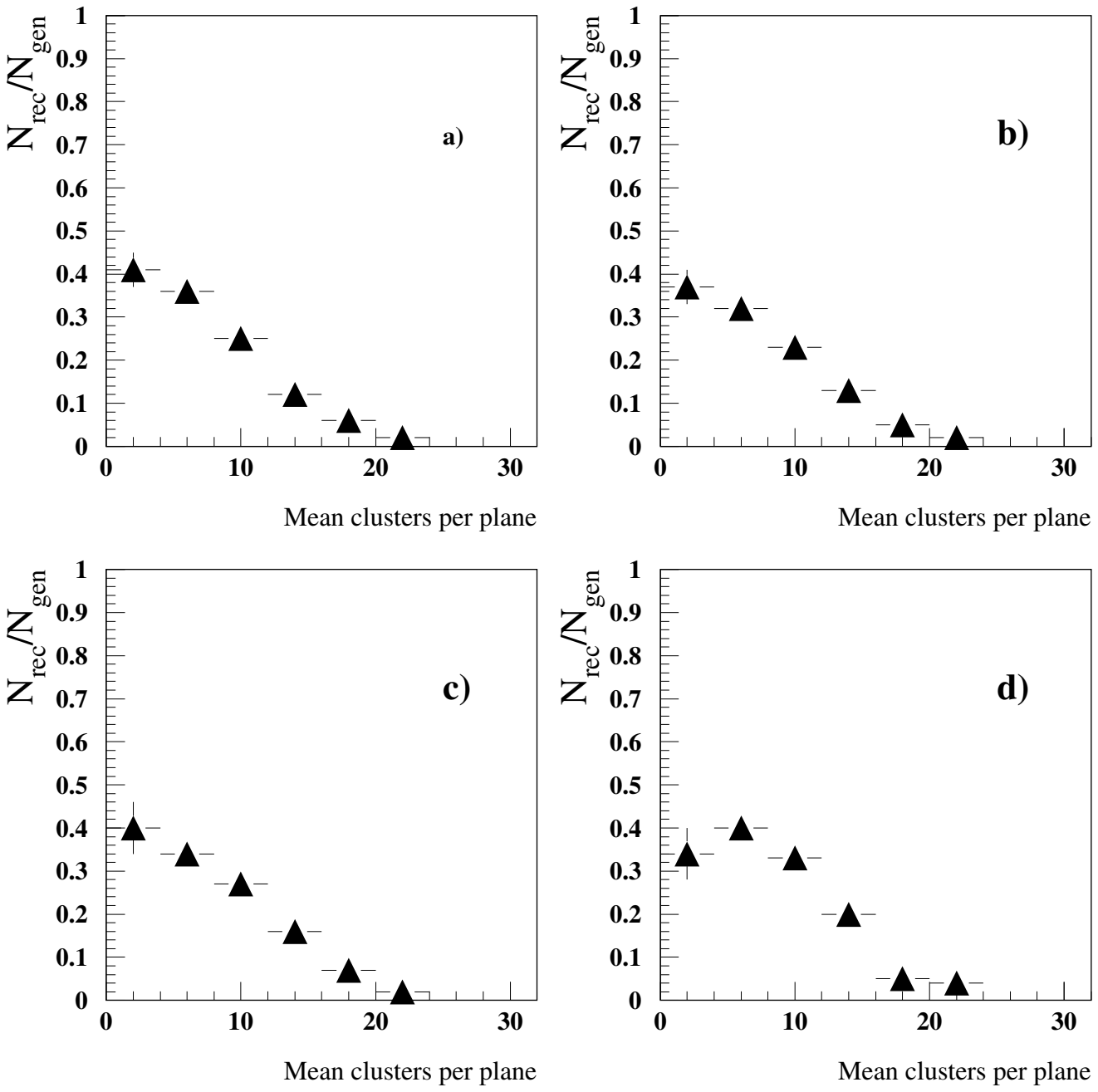

Figure 6.13: Reconstruction efficiencies as a function of MWPC cluster multiplicity for a) K^+s field down, b) K^-s (B=1.8T $\downarrow$), c) K^+s (B=1.8T $\uparrow$) and d) K^-s (B=1.8T $\uparrow$).

6.7 Further corrections to the data

At the end of chapter 3 it was mentioned that a further correction had to be applied to the Λ data; this is a correction that has to be made to take account of the fact that some of the Λs reconstructed will not come from the target but from Ξ decays. This is known as feed-down. This contamination of Λs ($\overline{\Lambda}$s) from Ξ ($\overline{\Xi}$) decays may be quite large for the following reasons. The decay region for Λ decays is some 135 cm from the target, and almost all the Ξs produced at the target will have decayed into Λs before reaching this region. Furthermore when a Ξ^- decays into a Λ and π^-, the Λ being much heavier than the π^- will carry much of the momentum of the Ξ^-, and will thus point back towards the target becoming difficult to distinguish from a Λ created at the target. This also explains why the cut on the momentum of the V^0 affects the kaon candidates and not the Ξ candidates, in the kaon case its 3 decay tracks will share the momentum approximately equally, and the reconstructed V^0 will only therefore carry about two thirds of the momentum, which will be below 6.5 GeV/c for many of the kaon candidates.

In order to calculate this contamination a sample of Monte Carlo Ξ^-s are generated and merged with real data as when calculating the reconstruction efficiencies, with a transverse mass distribution given by

$$\frac{1}{\mathrm{m_T^{\frac{3}{2}}}}\frac{\mathrm{dN}}{\mathrm{dm_T}} \sim \exp^{-\beta \mathrm{m_T}},$$

the composite events are then processed by TRIDENT, STRIPV0 and the analysis programs, the amount of contamination is then given by,

$$\text{contamination} = \frac{\mathrm{n_{\Xi_{real}}}}{\mathrm{n_{\Xi_{gen}}} \times 2} \times \frac{\mathrm{n_{\Lambda_{feed-down}}} \times 0.641}{\mathrm{n_{\Lambda_{real}}}},$$

where the factor $\frac{n_{\Xi_{real}}}{n_{\Xi_{gen}}}$ normalises the Monte Carlo data and the factor 2 takes account of the fact that the Monte Carlo particles were generated in the upper hemisphere only, and the factor 0.641 takes account of unseen decay modes. Contamination from Ξ^0s is calculated in the same way and normalised assuming that the number of Ξ^0s produced at the target is the same as for Ξ^-s. The contamination of $\overline{\Lambda}$s from $\overline{\Xi}$ decays is estimated in a similar manner.

It is found that about 7% of the Λ sample originate from Ξ^- decays and about 11% from Ξ^0 decays, whilst the $\overline{\Lambda}$ sample is contaminated by about 13% from $\overline{\Xi^-}$ decays and about 21% from $\overline{\Xi^0}$ decays.

6.8 Summary

The reconstruction efficiencies as well as the acceptances have been calculated for the different particle species recorded by WA94 in the 1991 sulphur-sulphur run. The efficiencies are found to be similar for particle and antiparticle, field up and field down, with the efficiencies varying between 65% and 40% for lambdas and between 40% to 25% for Ξs and kaons, in the multiplicity region of interest, i.e. 4 to 20.

The feed-down of lambdas from xi decays has also been calculated and there is found to be an overall contamination of $\sim 18\%$ for Λs from Ξ^- and Ξ^0 decays and $\sim 34\%$ for $\overline{\Lambda}$s from $\overline{\Xi^-}$ and $\overline{\Xi^0}$ decays.

The corrections to the data have now been calculated and in the next chapter corrected particle yields and distributions are presented for the 1991 sulphur-sulphur run.

Chapter 7

Corrected particle ratios and M_T distributions

In 1991 100 million triggers were taken by WA94 involving sulphur-sulphur interactions at 200 GeV/c per nucleon. The raw yields from these data are shown in table 7.1, where the unambiguous lambdas are given in brackets.

The corrections to this data to take account of the efficiencies and limited phase space covered by the WA94 detectors, as well the contamination of lambdas from xi decays has been calculated and in this chapter the relative yields of the different particle species observed by WA94 are presented and discussed; the transverse mass distributions of these particles are also presented.

7.1 Corrected particle yields

The relative yields for strange and multistrange baryon and antibaryon production have been studied by WA85 (sulphur-tungsten interactions) [21], NA36 (sulphur-lead interactions) [23] and now WA94 (sulphur-sulphur interactions). The corresponding ratios obtained are given in table 7.2, with their respective acceptance regions. These ratios have all been corrected for feed-down and it can be seen that the strangeness yield ratios obtained by WA94 are very similar to those obtained by WA85 in an equivalent centre of mass rapidity interval. The NA36 ratios are all lower than

Table 7.1: Raw yields of strange and multistrange particles and antiparticles obtained by WA94 in the 1991 sulphur-sulphur run.

Particle	Raw yield
Λ	56140 (28783)
$\overline{\Lambda}$	18014 (8783)
Ξ^-	547
$\overline{\Xi^-}$	278
K^-	430
K^+	202

those obtained by WA85 and WA94, but care should be taken when comparing these ratios as they used a slightly less central trigger than both WA85 and WA94 and as the individual rapidity distributions are not uniform the difference in the rapidity intervals has to be taken into account.

Theoreticians prefer to parametrise the ratios in terms of the transverse mass, m_T, instead of p_T. Therefore WA85 and WA94 have calculated the relative hyperon yields in the central rapidity region with $m_T > 1.9$ GeV. These are shown in table 7.3. Also for ease of comparison with other experiments the ratios have been calculated, like WA85, in the region $1.0 < p_T < 2.0$ GeV/c. These are also shown in table 7.3 as well as in figure 7.1 which shows the WA94 values along with WA85 and other published data for e^+e^- [35], $\overline{p}p$ [36] and pp [26]. Whilst the Ξ^-/Λ ratio is similar to those obtained for non heavy ion interactions, the $\overline{\Xi^-}/\overline{\Lambda}$ ratio (0.20 ± 0.02) is about 4 standard deviations larger than the value (0.06 ± 0.02) obtained by the AFS collaboration in pp interactions.

One should note that in a fixed kinematic window only three of the four ratios $\overline{\Lambda}/\Lambda$, $\overline{\Xi^-}/\Xi^-$, Ξ^-/Λ and $\overline{\Xi^-}/\overline{\Lambda}$ are independent, since the fourth can be estimated as for example

$$\frac{\overline{\Xi^-}}{\overline{\Lambda}} = \frac{\Xi^-}{\Lambda} \times \frac{\Lambda}{\overline{\Lambda}} \times \frac{\overline{\Xi^-}}{\Xi^-}.$$

There are usually several parameters to be fitted in a model [16] for chemical

Table 7.2: Strangeness Production Ratios for WA94 (S S), WA85 (S W) and NA36 (S Pb).

	WA94		WA85		NA36	
Ratio	Value	Acceptance Region	Value	Acceptance Region	Value	Acceptance Region
$\overline{\Lambda}/\Lambda$	0.23 ± 0.01	$2.5 < Y_{LAB} < 3.0$ $1.2 < p_T < 3.0$ GeV/c	0.20 ± 0.01	$2.3 < Y_{LAB} < 3.0$ $1.2 < p_T < 3.0$ GeV/c	0.207 ± 0.014	$1.5 < Y_{LAB} < 3.0$ $0.6 < p_T < 1.6$ GeV/c
$\overline{\Xi^-}/\Xi^-$	0.55 ± 0.07	same	0.45 ± 0.05	same	0.276 ± 0.108	$0.8 < Y_{LAB} < 1.8$ $0.8 < p_T < 1.8$ GeV/c
Ξ^-/Λ	0.09 ± 0.01	same	0.095 ± 0.006	same	0.066 ± 0.013	$1.5 < Y_{LAB} < 3.5$ $0.8 < p_T < 1.8$ GeV/c
$\overline{\Xi^-}/\overline{\Lambda}$	0.21 ± 0.02	same	0.21 ± 0.02	same	0.127 ± 0.022	$2.0 < Y_{LAB} < 3.0$ $0.6 < p_T < 1.6$ GeV/c

Table 7.3: Relative strange particle yields obtained by WA94 (S S) and WA85 (S W) in the given interval.

	WA94	WA85
	$2.5 < Y_{LAB} < 3.0$	$2.3 < Y_{LAB} < 2.8$
Ratio	$m_T > 1.9$ GeV	
$\overline{\Lambda}/\Lambda$	0.22 ± 0.01	0.20 ± 0.01
$\overline{\Xi^-}/\Xi^-$	0.54 ± 0.06	0.41 ± 0.05
Ξ^-/Λ	0.18 ± 0.01	0.19 ± 0.01
$\overline{\Xi^-}/\overline{\Lambda}$	0.44 ± 0.04	0.40 ± 0.04
Ratio	$1.0 < p_T < 2.0$ GeV	
$\overline{\Lambda}/\Lambda$	0.24 ± 0.01	–
$\overline{\Xi^-}/\Xi^-$	0.58 ± 0.07	–
Ξ^-/Λ	0.08 ± 0.01	0.09 ± 0.01
$\overline{\Xi^-}/\overline{\Lambda}$	0.20 ± 0.02	0.20 ± 0.03

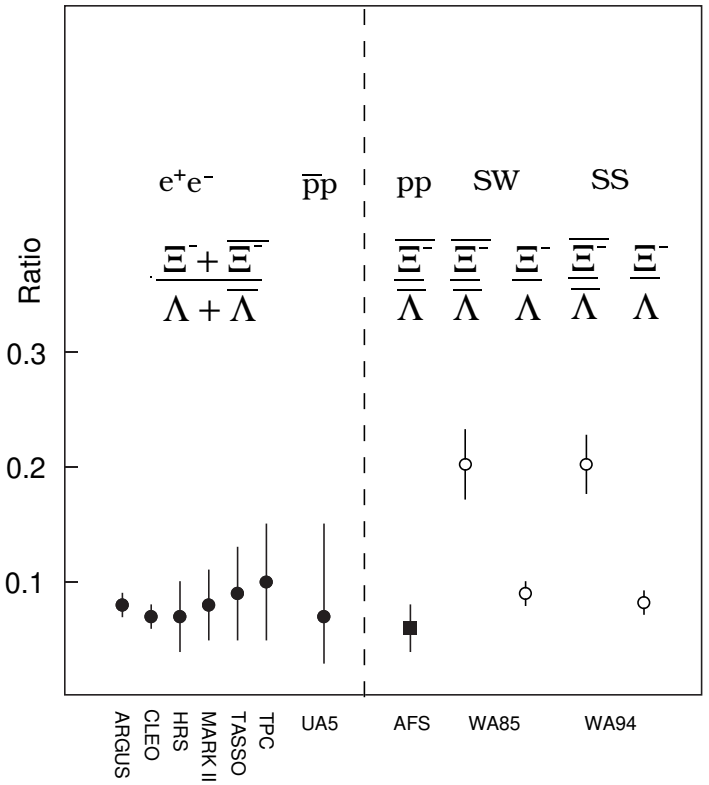

Figure 7.1: Ξ^-/Λ and $\overline{\Xi^-}/\overline{\Lambda}$ ratios for different experiments, including the WA94 points.

equilibrium (e.g. the baryochemical potential (μ_b), the strangeness chemical potential (μ_s) and the temperature (T)). Therefore, in order to constrain the models it is desirable to determine more ratios under the same centrality conditions. Kaons may be used for this purpose [19], provided we can assume the freeze-out temperatures for mesons and baryons are not much different. The raw yields of reconstructed kaons have been corrected for efficiency and acceptance and the corrected ratios are shown in table 7.4, in the acceptance window $2.7 < Y_{LAB} < 3.2$ and $1.0 < p_T < 2.0$ GeV/c. The reason for the ratio of $K^+(u\bar{s})$ to $K^-(\bar{u}s)$ being greater than one could

Table 7.4: Charged kaon production ratios obtained by WA94.

Ratio	Value
K^+/K^-	1.9 ± 0.4
K^+/Λ	2.5 ± 0.3
$K^-/\overline{\Lambda}$	1.3 ± 0.2

be due to the relative production of $\bar{s}$ quarks compared to s quarks being higher than the relative production of $\bar{u}$ quarks compared to u quarks. It should be noted that when the data is re-examined without the cut on the momentum of the V^0 the acceptance window might change and the errors on the ratios will decrease due to the higher statistics available.

7.2 M_T distributions

As mentioned in chapter 1, transverse mass distributions can show whether the particle production can be parameterized using thermal models, if so useful information can be gained about the approximate temperature of the source. For particles coming from a wide rapidity range, the transverse mass distributions are expected to be of the form,

$$\frac{1}{m_T^{\frac{3}{2}}}\frac{dN}{dm_T} \sim \exp^{-\beta m_T}$$

Table 7.5: Inverse slopes in MeV for Λs and Ξs.

Particle	WA94 (S S) $2.5 < Y_{LAB} < 3.0$ $1.0 < p_T < 3.0$ GeV/c	WA85 (S W) $2.3 < Y_{LAB} < 2.8$ $1.0 < p_T < 3.0$ GeV/c	NA35 (S S) $0.5 < Y_{LAB} < 3.0$ $0.3 < p_T < 2.0$ GeV/c
Λ	213 ± 3	232 ± 3	204 ± 17
$\overline{\Lambda}$	204 ± 5	230 ± 6	180 ± 24
Ξ^-	222 ± 10	239 ± 11	–
$\overline{\Xi^-}$	208 ± 13	234 ± 15	–

where β is the inverse temperature of the source and m_T the transverse mass. Figure 7.2 shows the m_T distributions for a) Λ and Ξ, and b) $\overline{\Lambda}$ and $\overline{\Xi^-}$ hyperons obtained by WA94 in the rapidity interval $2.5 < Y_{LAB} < 3.0$. The inverse slopes are given in table 7.5, together with those obtained by WA85, shown in chapter 1, and those obtained by the NA35 collaboration for Λs reconstructed in central sulphur-sulphur collisions [37]. The inverse slopes for Λ, $\overline{\Lambda}$, Ξ^- and $\overline{\Xi^-}$ hyperons are about 20 MeV lower than those obtained by the WA85 collaboration. The inverse slopes obtained by NA35 for Λs and $\overline{\Lambda}$s are compatible with those obtained by WA94.

The transverse mass distributions for charged kaons are shown in figure 7.3. The inverse slopes are shown in table 7.6, in the rapidity interval $2.7 < Y_{LAB} < 3.2$ and $1.0 < p_T < 2.0$ GeV/c, along with values obtained by the NA44 collaboration [38] for central sulphur-sulphur interactions and sulphur-lead interactions.

Table 7.6: Inverse slopes in MeV for charged kaons.

Particle	WA94 (S S)	NA44 (S S)	NA44 (S Pb)
K^+	172 ± 20	185 ± 5	205 ± 5
K^-	152 ± 25	180 ± 5	200 ± 5

It can be seen that the transverse mass distributions for charged kaons reconstructed by WA94 give inverse slopes lower than the corresponding values for Ξs and Λs. This could be explained by secondary collisions occurring within the fireball,

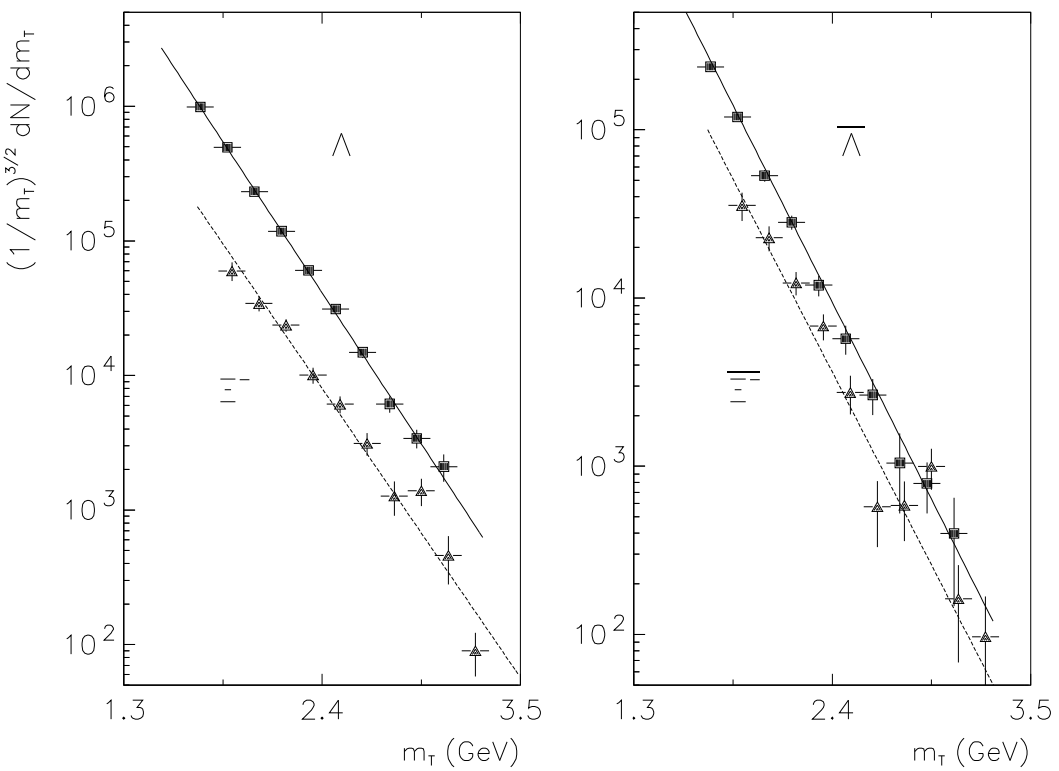

Figure 7.2: Transverse mass distributions for a) Λs and Ξ^-s, and b) $\overline{\Lambda}$s and $\overline{\Xi^-}$s, obtained by WA94.

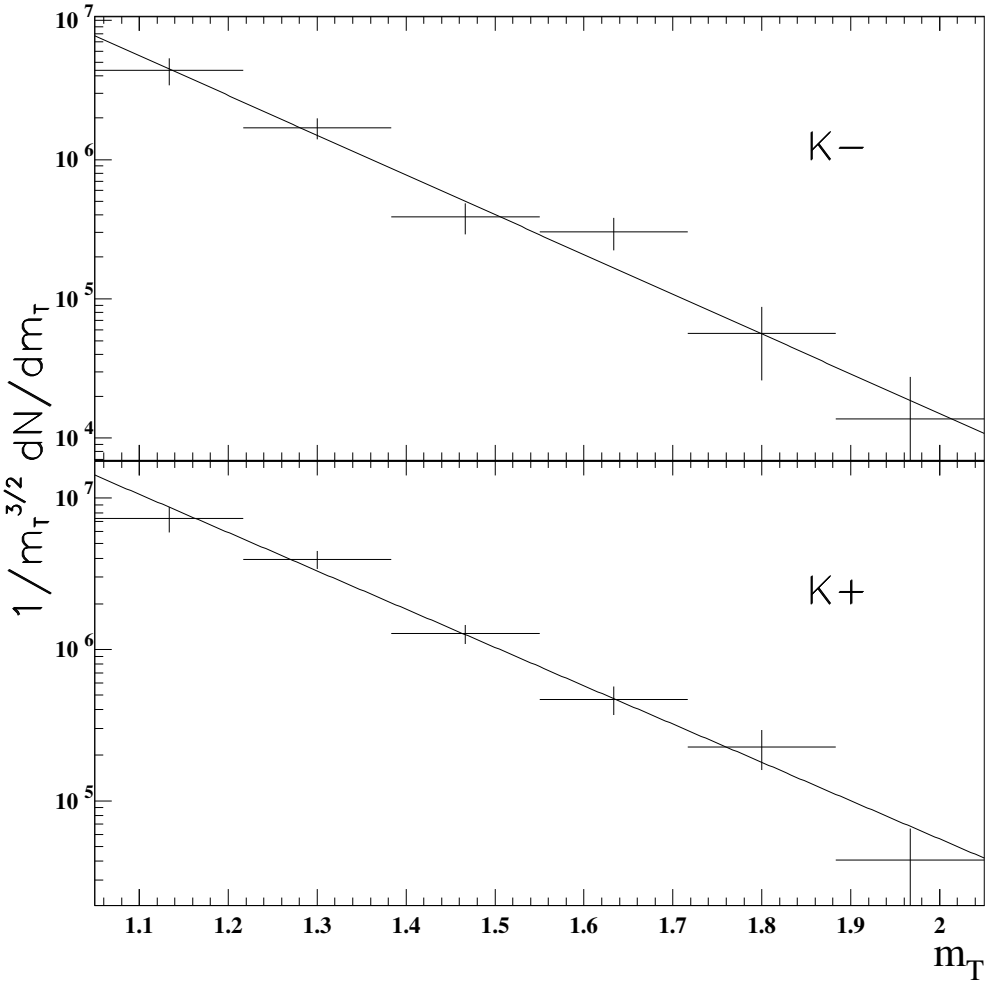

Figure 7.3: Transverse mass distributions for charged kaons, obtained by WA94.

producing kaons at a later time than the charged hyperons [39], which, due to the system cooling as it expands, will give lower temperatures for those particles which decouple later. This could also explain the steeper slope of K^- spectra compared to K^+ spectra seen in the data [38], as the scattering cross section of the K^- is larger and therefore they decouple from the system later than the K^+ and reflect a lower temperature.

7.3 Summary

Fully corrected yields for strange and multistrange particles and antiparticles have been presented, in particular the observation of a large value of the ratio $\Xi^-/\overline{\Lambda}$ compared to other published data confirms the values obtained previously by WA85. The inverse slopes of the m_T distributions for Λ, $\overline{\Lambda}$, Ξ^- and $\overline{\Xi^-}$ particles have been found to be slightly lower than those observed in central SW interactions, at around 210 MeV. Results on charged kaons have also been presented with m_T distributions giving inverse slopes of around 170 MeV.

Chapter 8

Summary and outlook

The interest in heavy ion interactions has been motivated by the prediction of QCD that hadronic matter under extreme conditions of temperature and/or pressure might undergo a phase transition to a Quark Gluon Plasma (QGP). If a QGP is produced an increase in the production of strange particles is expected.

The WA94 experiment is designed to study the production of strange and multi-strange particles and antiparticles at central rapidity in sulphur-sulphur interactions at 200 GeV/c per nucleon.

8.1 Results

WA94 has successfully reconstructed K^+, K^-, Λ, $\overline{\Lambda}$, Ξ^- and $\overline{\Xi^-}$ decays in the difficult environment of heavy ion interactions. WA94 has carried on the successful achievements of WA85, which was the first heavy ion experiment to reconstruct Ξs, and together the two experiments have over ten times the statistics on these multistrange particles than of all the other heavy ion experiments put together.

The transverse mass distributions of the WA94 data fit well with the idea that the particles originate from a thermal source. The inverse slopes of these distributions correspond to about 210 MeV for Λs and Ξs, slightly lower than those obtained by WA85, and about 170 MeV for charged kaons.

The production ratios for Ξ^-s, Λs, Ks and their corresponding antiparticles have

been obtained and the relative hyperon yields have been found to be very similar in central sulphur-sulphur and sulphur-tungsten interactions. In particular, as observed by WA85, the $\overline{\Xi^-}/\overline{\Lambda}$ ratio is about $3\frac{1}{2}$ times larger than the value measured in pp interactions, corresponding to a four standard deviation effect.

8.2 Future Plans

The experimental program which uses the CERN Ω Spectrometer, which was started by WA85 and followed by WA94 is now being continued by WA97 [40]. The WA97 experiment uses a lead beam with an energy of 160 GeV per nucleon onto a lead target. The principal aim is again to compare the production of baryons carrying one unit of strangeness (Λ) with those carrying two (Ξ^-) and three units of strangeness (Ω^-).

The larger volume of dense matter produced in lead-lead interactions should increase the likelihood for the onset of a phase transition from hadronic matter to a QGP. The larger volume of the system will also make the lifetime of the central fireball produced in the interaction longer, meaning more time will be available for strangeness equilibrium to be achieved. However with the heavier projectiles comes the problem of much larger multiplicities. An average number of some 3000 charged particles per event has been estimated for lead-lead collisions [41], compared to about 300 in central sulphur-sulphur collisions. The strategy applied to overcome this is (i) to use a restricted kinematic window, which can be moved over the required phase space window, while retaining the advantages of low multiplicity in the detector elements and (ii) to have a setup capable of high event rates to get good statistics in our kinematic window.

A first run by WA97 took place during November and December 1994, and 70 million events were recorded. The apparatus used is shown in figure 8.1. The scintillator petals detect tracks at backwards rapidities and are used to trigger on events having a large overall charge multiplicity. The multiplicity in the central region is sampled using silicon microstrips (multiplicity detectors). The silicon telescope is 55

Figure 8.1: The WA97 experimental layout used in the 1994 run and inset a Λ mass distribution.

cm long and consists of pixels, pads and microstrips to measure tracks of particles coming from the target in a small solid angle covering the central rapidity region. The pad chambers located about 4 metres downstream from the target are used to improve the momentum resolution and the tracking capability of the silicon telescope. Tracks have already been reconstructed in this difficult environment, and Λs have been successfully identified [42], as shown also in figure 8.1.

The heavy ion community has already joined forces in the ALICE (A Large Ion Collider Experiment) Collaboration in preparation for lead lead collisions at the Large Hadron Collider (LHC). These interactions will be studied at much higher energies, so that average energy densities well above those required for QGP formation will be achieved over large volumes and detailed studies of the QGP will be hopefully possible. These studies will provide important tests of long range QCD, and should also give information about some crucial predictions of cosmology and astrophysics.

8.3 Conclusions

The WA94 collaboration have been very successful in reconstructing strange particles and antiparticles in sulphur sulphur collisions at 200 GeV/c per nucleon. The relative production yields of the different particles species observed by WA94 show an enhanced production of strange matter occurring in heavy ion collisions compared to proton-nucleus interactions.

The transverse mass distributions showed that the data fitted well with a thermal source having a temperature of around 200 MeV, which is about the predicted critical temperature for the onset of QGP formation.

In 1993 data was recorded using a proton beam onto a sulphur target by the WA94 collaboration, this will provide a good comparison with results presented in this Thesis. At the present time data is being analysed from the first WA97 run using lead onto lead, while looking further ahead preparation is underway to take advantage of the large energies available when the LHC comes into operation. The

future is indeed looking bright for those whose goal is to recreate what could have been the state of the early universe, the QGP.

Appendix A

The Butterfly Geometry

The position of impact of tracks on the detector planes is considered. The method described here considers a particle of momentum $p = (p_L, p_T)$ in the laboratory and $p^* = (p_L^*, p_T^*)$ in the centre of mass frame, where $p_T = p_T^*$. It assumes the following:

- $p_L \gg p_T$, (for trigger particles $< p_T > \simeq 1GeV/c, < p_L > \simeq 10GeV/c$),
- $\beta \simeq 1, \gamma \sim 10$,
- rest mass m may be neglected ($p \simeq 10GeV/c$).

The laboratory scattering angle of a particle is given by:

$$\theta \simeq p_T/p_L$$

$$\Rightarrow \theta \simeq \frac{p_T^*}{\gamma(p_L^* + \beta E^*)}$$

$$\Rightarrow \theta \simeq \frac{1}{\gamma(1 + p_L^*/p_T^*)} \tag{A.1}$$

In the centre of mass frame the rapidity, Y^* is given by :

$$Y^* = \frac{1}{2} ln \frac{E^* + p_L^*}{E^* - p_L^*}$$

$$\Rightarrow sinh(Y^*) = \frac{p_L^*}{\sqrt{E^{*2} - p_L^{*2}}}$$

$$sinh(Y^*) \simeq \frac{p_L^*}{p_T^*} \tag{A.2}$$

Substituting (A.1) into (A.2) gives,

$$\theta \simeq \frac{1}{\gamma\{1 + sinh(Y^*)\}}. \tag{A.3}$$

Hence particles of a given Y^* correspond to a circle of hits on the detector planes. The effect of the Omega magnetic field is then to deflect charged particles. Since the magnetic field is in the vertical plane the amount of deflection is determined by the momentum component in the horizontal plane, i.e. essentially by p_L.

This is the basis of the design of the butterfly system. Figure 2.3 shows the loci of hits of particles with a given p_T, the envelopes of these loci form the characteristic butterfly shape. Particles of a lower p_T cannot enter the shaded butterfly regions shown in figure 2.3.

Appendix B

Armenteros Plots

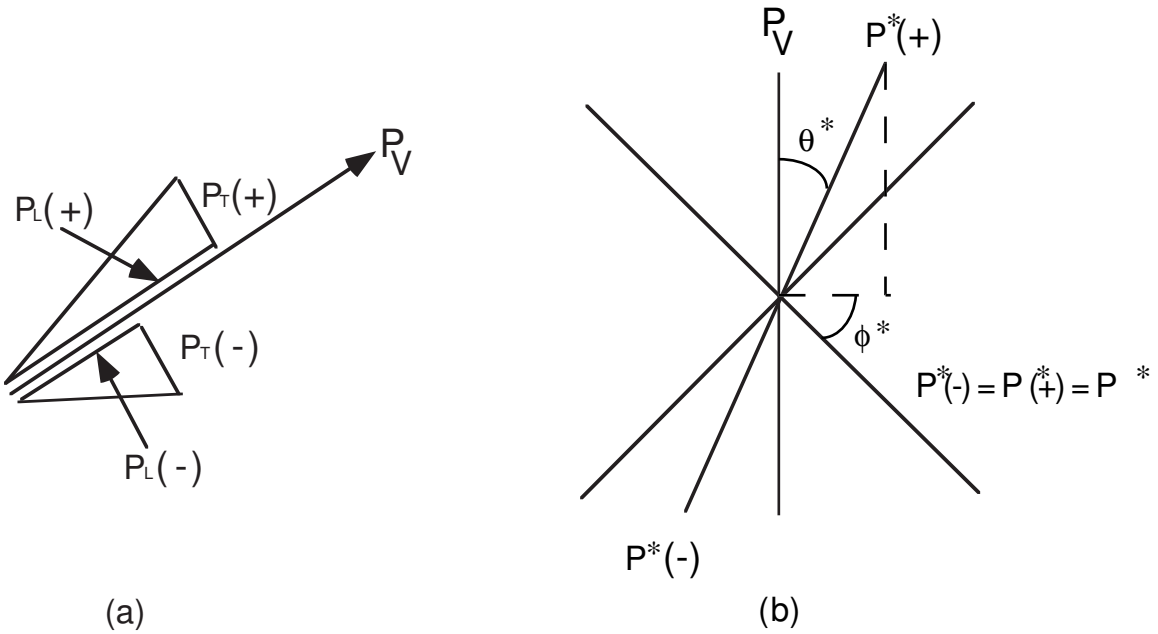

Figure B.1: Schematic representation of a V^0 decay in a) the lab frame and b) the centre of mass frame of the V^0 decay.

Figure B.1a shows the decay of a V^0 into a positive and negative particle, with a combined momentum p_L in the direction of motion of the V^0 and transverse momentum of p_T. In the centre of mass frame, figure B.1b, the momentum components are thus,

$$p_L^*(+) = p^* \cos\theta,$$

$$p_T^*(+) = p^* \sin\theta,$$

$$E^*(+) = \sqrt{p^{*2} + m^2(+)}.$$

To transform to the lab frame one uses Lorentz transformations, which in matrix form are given by [1]

$$\begin{pmatrix} E \\ p_L \end{pmatrix} = \begin{pmatrix} \gamma & \gamma\beta \\ \gamma\beta & \gamma \end{pmatrix} \begin{pmatrix} E^* \\ p_L^* \end{pmatrix}, \qquad p_T^* = p_T$$

where $\gamma = 1/\sqrt{1-\beta^2}$ and β is the velocity of the lab in the particles rest frame. This gives

$$E^{Lab}(+) = \gamma E^*(+) + \gamma\beta p_L^*(+)$$

$$p_L^{Lab}(+) = \gamma p_L^*(+) + \gamma\beta E^*(+) = \gamma p^* \cos\theta^* + \gamma\beta E^*(+)$$

$$p_T^{Lab}(+) = p_T^*(+) = p^* \sin\theta^*$$

i.e.

$$p_L^{Lab}(+) = \gamma p^* \cos\theta^* + \gamma\beta E^*(+)$$

$$p_L^{Lab}(-) = \gamma p^* \cos\theta^* + \gamma\beta E^*(-)$$

therefore

$$p_L^{Lab}(+) - p_L^{Lab}(-) = 2\gamma p^* \cos\theta^* + \beta\gamma(E^*(+) - E^*(-))$$

$$p_L^{Lab}(+) + p_L^{Lab}(-) = p_L^{Lab} = \beta\gamma m_V^0.$$

The Armenteros α is defined by [32]

$$\alpha = \frac{p_L^{Lab}(+) - p_L^{Lab}(-)}{p_L^{Lab}(+) + p_L^{Lab}(-)} = \frac{2p^* \cos\theta^*}{\beta m_V^0} + \frac{E^*(+) - E^*(-)}{m_V^0} = \xi \cos\theta^* + \varphi$$

therefore

$$\cos\theta^* = \frac{\alpha - \varphi}{\xi} \qquad \sin\theta^* = \frac{p_T^*}{p^*}$$

$$\cos^2\theta^* + \sin^2\theta^* = 1 = (\frac{\alpha - \varphi}{\xi})^2 + (\frac{p_T^*}{p^*})^2.$$

This is an equation of an ellipse with centre (φ,0) and semi axis in α of length ξ, and in p_T length p^*. Table B.1 shows the value of these variables for the decays of Λs, $\overline{\Lambda}$s and K^0s, whilst the theoretical plots for Λs, $\overline{\Lambda}$s and K^0s are shown in figure B.2.

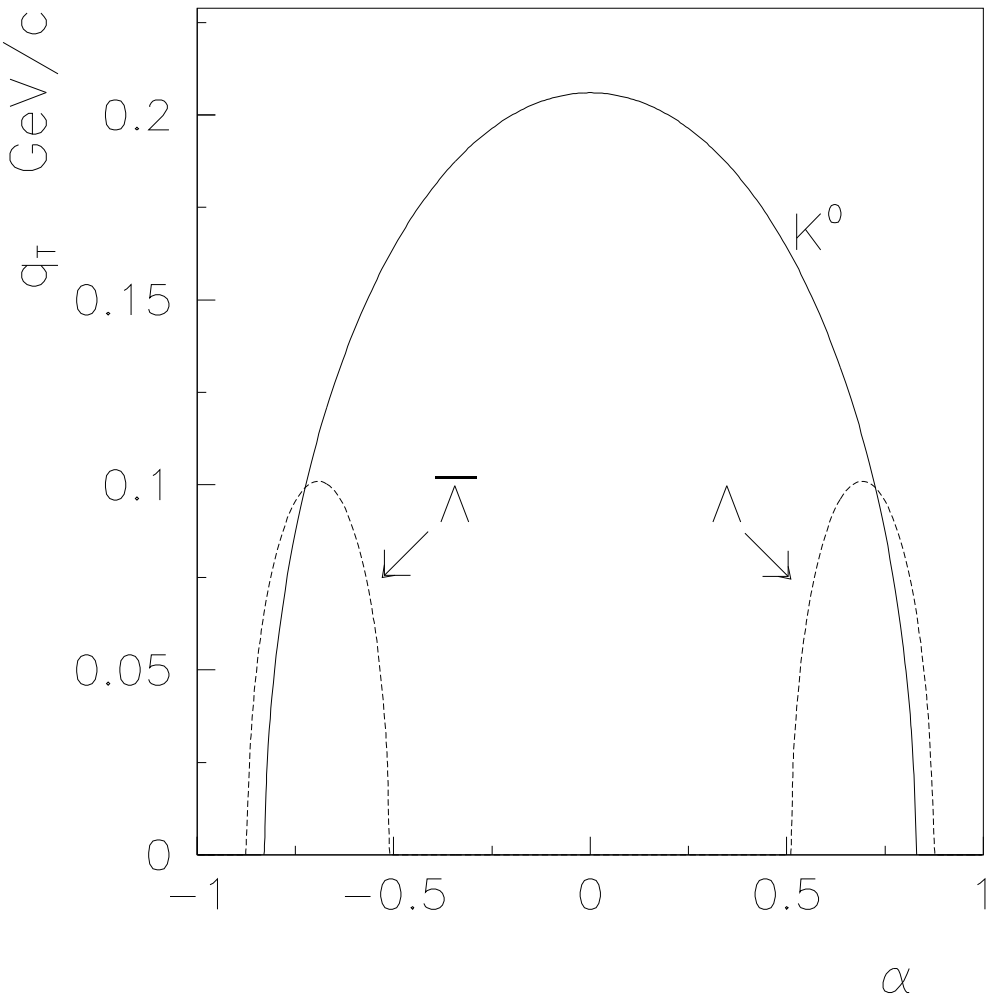

Figure B.2: Podolanski-Armenteros regions for different V^0 candidates.

Decay	ξ	p^* (GeV/c)	$\alpha_{\min}$	$\alpha_{\max}$	φ
$K^0_S \to \pi^+\pi^-$	0.8282	0.206	-0.828	+0.8282	0.
$\Lambda \to p\pi^-$	0.179	0.101	+0.515	0.873	0.694
$\overline{\Lambda} \to \overline{p}\pi^+$	0.179	0.101	-0.873	-0.515	-0.694

Table B.1: Armenteros quantities.

Appendix C

Acceptance Tables

The geometrical acceptances of unambiguous Λs ($0.45 < |\alpha| < 0.60$), Ξ^-s and K^+s for the experimental layout and trigger used in the WA94 1991 sulphur-sulphur run are given in the following tables, as a function of rapidity, Y_{LAB}, and p_T. The acceptances of the corresponding antiparticles are the same due to the symmetry of the magnetic field and apparatus. Unseen decay modes and decays outside the fiducial region are included in the acceptance tables.

Table C.1: Acceptances for Λs produced in S S interactions (in percent).

Y_{LAB}	2.525	2.575	2.625	2.675	2.725	2.775	2.825	2.875	2.925	2.975
p_T = 0.85 GeV/c	0.050	0.058	0.064	0.069	0.069	0.064	0.051	0.020	0.000	0.000
p_T = 0.95 GeV/c	0.073	0.089	0.103	0.114	0.117	0.118	0.109	0.091	0.056	0.003
p_T = 1.05 GeV/c	0.096	0.122	0.144	0.166	0.179	0.186	0.182	0.165	0.139	0.091
p_T = 1.15 GeV/c	0.122	0.158	0.192	0.220	0.242	0.259	0.259	0.252	0.228	0.184
p_T = 1.25 GeV/c	0.144	0.194	0.241	0.282	0.314	0.336	0.350	0.345	0.325	0.288
p_T = 1.35 GeV/c	0.145	0.227	0.288	0.342	0.381	0.413	0.433	0.437	0.417	0.380
p_T = 1.45 GeV/c	0.141	0.251	0.331	0.392	0.450	0.486	0.507	0.521	0.499	0.471
p_T = 1.55 GeV/c	0.141	0.241	0.363	0.449	0.508	0.555	0.580	0.585	0.579	0.548
p_T = 1.65 GeV/c	0.138	0.226	0.389	0.486	0.563	0.608	0.640	0.661	0.643	0.627
p_T = 1.75 GeV/c	0.135	0.217	0.390	0.519	0.604	0.662	0.694	0.715	0.705	0.686
p_T = 1.85 GeV/c	0.132	0.212	0.357	0.548	0.650	0.706	0.745	0.753	0.758	0.728
p_T = 1.95 GeV/c	0.128	0.208	0.336	0.572	0.678	0.744	0.780	0.804	0.798	0.777
p_T = 2.05 GeV/c	0.125	0.201	0.330	0.575	0.718	0.783	0.816	0.837	0.839	0.814
p_T = 2.15 GeV/c	0.122	0.202	0.320	0.571	0.734	0.820	0.849	0.869	0.870	0.853
p_T = 2.25 GeV/c	0.123	0.202	0.317	0.547	0.755	0.842	0.878	0.891	0.899	0.882
p_T = 2.35 GeV/c	0.122	0.201	0.316	0.511	0.775	0.874	0.908	0.918	0.914	0.900
p_T = 2.45 GeV/c	0.121	0.202	0.316	0.505	0.794	0.891	0.926	0.934	0.946	0.922
p_T = 2.55 GeV/c	0.125	0.199	0.313	0.497	0.806	0.918	0.945	0.950	0.962	0.949
p_T = 2.65 GeV/c	0.123	0.201	0.313	0.488	0.819	0.938	0.962	0.975	0.976	0.961
p_T = 2.75 GeV/c	0.120	0.201	0.313	0.485	0.817	0.950	0.985	0.988	0.990	0.971
p_T = 2.85 GeV/c	0.120	0.203	0.316	0.493	0.829	0.970	0.993	1.008	0.995	0.990
p_T = 2.95 GeV/c	0.124	0.202	0.317	0.491	0.829	0.979	1.002	1.011	1.009	0.985

Table C.2: Acceptances for Ξ^-s produced in S S interactions (in percent).

Y_{LAB}	2.525	2.575	2.625	2.675	2.725	2.775	2.825	2.875	2.925	2.975
p_T = 1.25 GeV/c	0.043	0.049	0.054	0.057	0.058	0.056	0.054	0.047	0.036	0.020
p_T = 1.35 GeV/c	0.075	0.083	0.090	0.096	0.099	0.099	0.095	0.088	0.072	0.054
p_T = 1.45 GeV/c	0.113	0.129	0.141	0.151	0.154	0.154	0.150	0.139	0.122	0.100
p_T = 1.55 GeV/c	0.158	0.182	0.202	0.212	0.217	0.220	0.210	0.199	0.183	0.158
p_T = 1.65 GeV/c	0.205	0.240	0.265	0.283	0.288	0.287	0.282	0.267	0.249	0.217
p_T = 1.75 GeV/c	0.247	0.299	0.333	0.358	0.363	0.363	0.352	0.336	0.314	0.282
p_T = 1.85 GeV/c	0.291	0.355	0.400	0.429	0.439	0.441	0.424	0.408	0.382	0.349
p_T = 1.95 GeV/c	0.328	0.407	0.466	0.499	0.515	0.512	0.500	0.478	0.450	0.409
p_T = 2.05 GeV/c	0.359	0.456	0.531	0.571	0.590	0.587	0.572	0.548	0.509	0.465
p_T = 2.15 GeV/c	0.378	0.504	0.594	0.641	0.662	0.658	0.636	0.602	0.571	0.528
p_T = 2.25 GeV/c	0.387	0.544	0.645	0.704	0.727	0.727	0.701	0.671	0.629	0.578
p_T = 2.35 GeV/c	0.396	0.581	0.694	0.763	0.796	0.788	0.761	0.723	0.672	0.621
p_T = 2.45 GeV/c	0.404	0.609	0.743	0.816	0.854	0.845	0.813	0.774	0.723	0.667
p_T = 2.55 GeV/c	0.413	0.632	0.791	0.868	0.902	0.898	0.864	0.817	0.766	0.701
p_T = 2.65 GeV/c	0.422	0.644	0.823	0.914	0.950	0.941	0.905	0.858	0.797	0.729
p_T = 2.75 GeV/c	0.431	0.649	0.855	0.948	0.990	0.982	0.941	0.890	0.827	0.756
p_T = 2.85 GeV/c	0.437	0.643	0.885	0.987	1.027	1.019	0.977	0.919	0.852	0.781
p_T = 2.95 GeV/c	0.442	0.636	0.901	1.017	1.058	1.049	1.011	0.939	0.881	0.801

Table C.3: Acceptances for K^+s produced in S S interactions (in percent).

Y_{LAB}	2.725	2.775	2.825	2.8750	2.925	2.975	3.025	3.075	3.125	3.175
p_T = 1.05 GeV/c	.0005	.0012	.0020	.0032	.0043	.0048	.0050	.0049	.0044	.0035
p_T = 1.15 GeV/c	.0021	.0037	.0048	.0057	.0069	.0072	.0070	.0062	.0060	.0048
p_T = 1.25 GeV/c	.0046	.0060	.0075	.0083	.0087	.0082	.0081	.0075	.0064	.0050
p_T = 1.35 GeV/c	.0075	.0092	.0097	.0101	.0099	.0095	.0082	.0078	.0064	.0055
p_T = 1.45 GeV/c	.0095	.0104	.0107	.0109	.0104	.0097	.0082	.0074	.0068	.0059
p_T = 1.55 GeV/c	.0118	.0119	.0116	.0110	.0099	.0092	.0077	.0069	.0065	.0059
p_T = 1.65 GeV/c	.0134	.0133	.0124	.0115	.0096	.0090	.0081	.0071	.0064	.0058
p_T = 1.75 GeV/c	.0135	.0128	.0117	.0108	.0095	.0087	.0082	.0070	.0061	.0054
p_T = 1.85 GeV/c	.0133	.0123	.0113	.0103	.0094	.0084	.0079	.0068	.0063	.0046
p_T = 1.95 GeV/c	.0124	.0119	.0111	.0101	.0092	.0083	.0074	.0066	.0056	.0045
p_T = 2.05 GeV/c	.0110	.0127	.0102	.0098	.0089	.0084	.0069	.0060	.0053	.0045
p_T = 2.15 GeV/c	.0112	.0112	.0103	.0093	.0086	.0078	.0067	.0060	.0047	.0046
p_T = 2.25 GeV/c	.0111	.0099	.0097	.0085	.0082	.0068	.0065	.0055	.0052	.0047
p_T = 2.35 GeV/c	.0107	.0096	.0094	.0081	.0075	.0071	.0063	.0047	.0046	.0035
p_T = 2.45 GeV/c	.0103	.0095	.0093	.0077	.0068	.0061	.0060	.0045	.0039	.0035
p_T = 2.55 GeV/c	.0094	.0087	.0074	.0072	.0063	.0057	.0048	.0044	.0041	.0031
p_T = 2.65 GeV/c	.0091	.0083	.0068	.0070	.0062	.0054	.0046	.0044	.0039	.0029
p_T = 2.75 GeV/c	.0093	.0081	.0068	.0067	.0059	.0050	.0044	.0043	.0037	.0028
p_T = 2.85 GeV/c	.0084	.0078	.0066	.0065	.0061	.0051	.0043	.0036	.0027	.0025
p_T = 2.95 GeV/c	.0072	.0072	.0064	.0061	.0047	.0045	.0040	.0034	.0033	.0020

Appendix D

MWPC efficiencies for the 1991 ions run

Results of the calculations of the chamber efficiencies for the A chambers from the WA94 1991 sulphur-sulphur run are presented.

Table D.1: Mean efficiencies for chamber A1.

Y Plane	Quad 1	0.891 ± 0.012
	Quad 2	0.892 ± 0.014
	Quad 3	0.936 ± 0.011
	Quad 4	0.938 ± 0.013
U Plane	Quad 1	0.901 ± 0.012
	Quad 2	0.875 ± 0.012
	Quad 3	0.941 ± 0.011
	Quad 4	0.943 ± 0.013
V Plane	Quad 1	0.879 ± 0.012
	Quad 2	0.882 ± 0.013
	Quad 3	0.932 ± 0.012
	Quad 4	0.920 ± 0.014

Table D.2: Mean efficiencies for chamber A2.

Y Plane	Quad 1	0.907 ± 0.012
	Quad 2	0.906 ± 0.013
	Quad 3	0.952 ± 0.011
	Quad 4	0.958 ± 0.013
U Plane	Quad 1	0.917 ± 0.013
	Quad 2	0.902 ± 0.014
	Quad 3	0.944 ± 0.013
	Quad 4	0.955 ± 0.012
V Plane	Quad 1	0.901 ± 0.012
	Quad 2	0.920 ± 0.014
	Quad 3	0.952 ± 0.011
	Quad 4	0.958 ± 0.012

Table D.3: Mean efficiencies for chamber A3.

Y Plane	Quad 1	0.940 ± 0.013
	Quad 2	0.933 ± 0.014
	Quad 3	0.966 ± 0.011
	Quad 4	0.966 ± 0.013
U Plane	Quad 1	0.936 ± 0.013
	Quad 2	0.942 ± 0.014
	Quad 3	0.968 ± 0.012
	Quad 4	0.969 ± 0.013
V Plane	Quad 1	0.928 ± 0.013
	Quad 2	0.934 ± 0.014
	Quad 3	0.957 ± 0.011
	Quad 4	0.953 ± 0.013

Table D.4: Mean efficiencies for chamber A4.

Y Plane	Quad 1	0.945 ± 0.013
	Quad 2	0.942 ± 0.014
	Quad 3	0.970 ± 0.011
	Quad 4	0.976 ± 0.013
U Plane	Quad 1	0.909 ± 0.013
	Quad 2	0.922 ± 0.014
	Quad 3	0.935 ± 0.012
	Quad 4	0.923 ± 0.013
V Plane	Quad 1	0.906 ± 0.013
	Quad 2	0.883 ± 0.014
	Quad 3	0.922 ± 0.011
	Quad 4	0.917 ± 0.013

Table D.5: Mean efficiencies for chamber A5.

Y Plane	Quad 1	0.924 ± 0.013
	Quad 2	0.937 ± 0.014
	Quad 3	0.955 ± 0.011
	Quad 4	0.956 ± 0.013
U Plane	Quad 1	0.886 ± 0.012
	Quad 2	0.881 ± 0.014
	Quad 3	0.907 ± 0.012
	Quad 4	0.908 ± 0.013
V Plane	Quad 1	0.915 ± 0.013
	Quad 2	0.936 ± 0.014
	Quad 3	0.942 ± 0.011
	Quad 4	0.940 ± 0.013

Table D.6: Mean efficiencies for chamber A6.

Y Plane	Quad 1	0.928 ± 0.013
	Quad 2	0.948 ± 0.014
	Quad 3	0.940 ± 0.011
	Quad 4	0.959 ± 0.013
U Plane	Quad 1	0.922 ± 0.013
	Quad 2	0.922 ± 0.014
	Quad 3	0.939 ± 0.011
	Quad 4	0.944 ± 0.013
V Plane	Quad 1	0.897 ± 0.013
	Quad 2	0.888 ± 0.014
	Quad 3	0.864 ± 0.011
	Quad 4	0.880 ± 0.013

Table D.7: Mean efficiencies for chamber A7.

Y Plane	Quad 1	0.896 ± 0.013
	Quad 2	0.891 ± 0.014
	Quad 3	0.897 ± 0.011
	Quad 4	0.858 ± 0.012
U Plane	Quad 1	0.862 ± 0.013
	Quad 2	0.895 ± 0.014
	Quad 3	0.872 ± 0.011
	Quad 4	0.705 ± 0.011
V Plane	Quad 1	0.837 ± 0.012
	Quad 2	0.631 ± 0.013
	Quad 3	0.791 ± 0.011
	Quad 4	0.826 ± 0.012

Bibliography

[1] D.H.Perkins, Introduction to High Energy Physics, Addison-Wesley Publishing Company, Third Edition 1987.

[2] F. Abe et al, The CDF Collaboration, Phys. Rev. **D50** (1994) 2966.

[3] F.Halzen and A.D.Martin, Quarks and Leptons: An Introductory Course in Modern Particle Physics, John Wiley and Sons, 1984.

[4] J. Rafelski, 21st Rencontres de Moriond, Les Arcs, 1983.

[5] L. Van Hove, Quark Gluon Plasma and Multiparticle Production, CERN-TH.5236/88.

[6] B. Muller, The Physics of the Quark-Gluon-Plasma , Springer-Verlag, 1985.

[7] M. Jacob, In Search of Quark Matter, CERN - TH. 7343/94.

[8] L. Dragon et al, The WA80 Collaboration, Nuclear Physics **A525** (1991), 305c.

[9] R. Santo et al, The WA80 Collaboration, Nuclear Physics **A566** (1994), 61c.

[10] P. V. Ruuskanen, Nuclear Physics **A525** (1991), 255c.

[11] T. Matsui and H. Satz, Phys. Lett **B178** (1986) 416.

[12] S. Gavin and M. Gyulassy, Phys. Lett **B214** (1988) 214.

[13] S. Gupta and H. Satz, Phys. Lett **B283** (1992) 439.

[14] M.C. Abreau et al., Nuclear Physics **A566** (1994), 77c.

[15] M.C. Abreau et al., Nuclear Physics **A566** (1994), 367c.

[16] P. Koch, B. Muller and J. Rafelski, Phys. Rev. **C142** (1986) 167, and references therein.

[17] H. C. Eggers and J. Rafelski XXIVth Rencontres de Moriond, March 1989.

[18] H. C. Eggers and J. Rafelski, Int. J. of Mod. Phys. A, Vol. 6, No. 7 (1991) 1067.

[19] U. Heinz, Nuclear Physics **A566** (1994), 205c.

[20] WA85 Proposal, CERN/SPSC/84-76 P206 (1984) CERN/SPSC/87-18 P206 Add. (1987),CERN/SPSC/88-20 P206 Add. (1988).

[21] The WA85 Coll., D. Evans et al., Nuclear Physics **A566** (1994), 225c.

[22] The WA85 Coll., S. Abatzis et al., Nuclear Physics **A525** (1991), 445c.

[23] The NA36 Coll., E. Andersen et al., Nuclear Physics **A566** (1994), 217c.

[24] The WA85 Coll., S. Abatzis et al., Phys. Lett. **B316** (1993) 615.

[25] The WA85 Coll., F. Antinori et al., Proc. of the NATO Advanced Research Workshop on Hot Hadronic Matter, Divonne-les-Bains, June 1994, to be published.

The WA85 Coll., S. Abatzis et al., to be published in Phys. lett. B.

[26] The AFS Coll., T. Åkesson et al., Nucl. Phys. **B246** (1984) 1-11.

[27] WA94 Proposal, CERN/SPSLC/91-5 (1991).

[28] The WA94 Coll., A.C. Bayes et al., Nuclear Physics **A566** (1994), 499c.

[29] W. Beusch, Omega Prime, CERN/SPSC/84-62/P204 (1984).

[30] J. Rafelski and M. Danos, Phys. Lett. **B192** (1987) 432.

[31] J-C Lassalle et. al. DD/EE/79-2 (TRIDENT Manual).

[32] J. Podolanski and R. Armenteros, Phil. Mag 45 (1954) 13.

[33] Particle Data Group, Phys. Rev. D. (1994) D50, 1172-1825.

[34] Thesis of R. P. Barnes, Production of Strange and Multistrange Baryons in Ultrarelativistic Heavy Ion Collisions, The University of Birmingham (1994).

[35] The ARGUS Coll., A. Albrecht et al., Phys. Lett. **B183** (1987) 419.
The CLEO Coll., M. S. Alam et al., Phys. Rev. Lett. 53 (1984) 24.
The HRS Coll., S. Abachi et al., Phys. Rev. Lett. 58 (1987) 2627.
The MARK II Coll., S. R. Klein et al., Phys. Rev. Lett. 58 (1987) 644.
The TASSO Coll., M. Althoff et al., Phys. Lett. **B130** (1983) 340.
The TPC Coll., H. Yamamoto et al., proceedings of the XXth Recontres de Moriond (1986).

[36] The UA5 Coll. R. E. Ansorge et al., CERN-EP/89-41.

[37] T. Alber et al., IKF-HENPG/1-94 (Univ. Frankfurt).

[38] The NA44 Coll., J. Dodd et al., Proceedings of the Eleventh International Conference on Ultra-Relativistic Nucleus-Nucleus Collisions, Monterey, California (1995), to be published.

[39] B. V. Jacak, Particle Production in Highly Excited Matter., Edited by H. H. Gutbrod and J. Rafelski, Plenum Press, New York (1993).

[40] WA97 Proposal, CERN/SPSLC/91-29 (1991).

[41] N. S. Amelin, K. K. Gudima, S. Y. Sivoklokov and V. D. Toneev, Sov. J. Nucl. Phys. 52 (1990) 172.

[42] The WA97 Coll., F. A. Antinori et al., Proceedings of the Eleventh International Conference on Ultra-Relativistic Nucleus-Nucleus Collisions, Monterey, California (1995), to be published.